EXPERIMENTAL STUDY OF BUILT-UP-EDGE FORMATION IN MICRO MILLING

A Thesis

by

VIVEKANANDA REDDY KOVVURI

Submitted to the Office of Graduate and Professional Studies of
Texas A&M University
in partial fulfillment of the requirements for the degree of

MASTER OF SCIENCE

Chair of Committee,	Satish Bukkapatnam
Co-Chair of Committee,	Wayne N.P. Hung
Committee Member,	Amarnath Banerjee
Head of Department,	César O. Malavé

August 2015

Major Subject: Industrial Engineering

ABSTRACT

Micromachining relies on precise tool geometry for effective material removal and acceptable surface finish. The detrimental built-up-edges (BUEs) not only degrade the surface finish of machined features, but also pose a concern for critical applications when BUE can be eventually detached from machined surface.

This work presents experimental study on conditions for BUE formation and its effects in micro milling of biocompatible 316L stainless steel. Surface finish and BUE density on a micro milled surface are used to quantify the presence of BUE. A new micro tool is used for each milling condition. A BUE, embedded onto a milled surface, is identified by scanning electron microscopy and energy dispersive X-ray analysis. Optical microscopy is used to quantify BUE density at different locations and milling parameters.

Surface finish data from meso-scale milling agree with predicted surface finish, but the model fails to predict the surface finish in micro-scale milling. Micro milling resulted in rough surface finish at low cutting speeds and chip loads due to formation and detachment of BUE from tool surface to machined surface. Hence a new surface finish model including the effect of BUE and tool wear was developed.

DEDICATION

To my Mom, Dad and Brother for their love and support

ACKNOWLEDGEMENTS

I would like to thank my committee chair and co-chair, Dr. Bukkapatnam and Dr. Hung who have been constantly advising me throughout my research. They have always guided me when required and played a critical role in my progress. I would also like to extend my heartfelt thanks to committee member Dr. Banerjee for his constant support. Thanks also extend to Dr. Srinivasa for his advice and suggestions.

I would like to extend a warm thanks to Zimo Wang for his guidance and assistance in machining experiments. Thanks also go to the rest of the Smart Manufacturing Research Group for their valuable support during this time.

I would like to thank Mr. Adam Farmer for his support and advice on machining experiments. Thanks to HAAS Automation, Performance Micro Tools and UNIST for providing us with valuable tools required for this research. Thanks also extend to National Science foundation (NSF grant: CMMI 1432914, CMMI 1437319) for their support towards this project.

Finally, thanks to my mother and father, family and friends for their encouragement, patience and support.

NOMENCLATURE

α	Concavity angle (^{o})
β	Axial relief angle (^{o})
μ	Coefficient of friction
D	Tool diameter (mm)
d	Depth of cut (μm)
f	Chip load (μm/tooth)
δ	Friction angle (^{o})
ϕ	End rake angle (^{o})
θ	Shear plane angle (^{o})
f_z	Spindle frequency (Hz)
F_c	Cutting force (Newton)
F_s	Shearing force (Newton)
h	uncut chip thickness (μm)
h_m	Minimum chip thickness (μm)
N	Tool rotational speed (revolutions per minute)
R_a	Average line roughness (μm)
R_{max}	Maximum height of surface (μm)
r_e	Tool edge radius (μm)
r_r	Ratio of uncut chip thickness to tool edge radius
S_a	Average surface roughness (μm)

t	Maximum height of surface (μm)
v	Cutting speed (m/min)
μEDM	Micro-electro discharge machining
BUE	Built-up-edge
CNC	Computerized numerical control
CrN	Chromium Nitride
CrTiAlN	Chromium Titanium Aluminum Nitride
EDS	Energy dispersive X-Ray spectroscopy
FEA	Finite element analysis
FFT	Fast Fourier transformation
HRC	Rockwell C hardness
MRR	Material removal rate
SEM	Scanning electron microscopy
TiAlN	Titanium Aluminum Nitride
TiCN	Titanium carbonitride
TiN	Titanium Nitride

TABLE OF CONTENTS

Page

ABSTRACT ii

DEDICATION iii

ACKNOWLEDGEMENTS iv

NOMENCLATURE v

TABLE OF CONTENTS vii

LIST OF FIGURES ix

LIST OF TABLES xiv

1. INTRODUCTION 1

    1.1 Issues with non-traditional micro manufacturing techniques 3

2. OBJECTIVE AND SCOPE 5

3. LITERATURE REVIEW 6

    3.1 Machining variables in micro machining 6
    3.2 Surface finish modeling 9
    3.3 Built-up-edge mechanism and effects 18
    3.4 Study of tool vibration on surface topography 22

4. EXPERIMENTS 24

    4.1 List of equipment 24
    4.2 Equipment calibrations 24
    4.3 Experiments 26

5. RESULTS AND DISCUSSION 42

    5.1 Tool runout results 42
    5.2 Tool offset 48
    5.3 Detection of built-up-edge 49
    5.4 Surface roughness and built-up-edge 52
    5.5 Theoretical model 55

Page

5.6 Results of meso milling experiments 56
5.7 Results of micro milling experiments 62

6. CONCLUSIONS 85

7. RECOMMENDATIONS AND FUTURE WORK 86

REFERENCES 87

APPENDIX A SPECIFICATIONS OF EQUIPMENT 91

APPENDIX B MODELLING OF LINE SURFACE ROUGHNESS IN FLAT END MILLING 98

APPENDIX C CNC CODE 102

C.1 Spindle warmup program 102
C.2 Meso and Micro slot milling program 102

APPENDIX D EXPERIMENTAL DATA 103

APPENDIX E R STATISTICAL DATA 108

LIST OF FIGURES

Page

Figure 1. Accuracy and precision achievable in machining (McKeown, 1986). 1

Figure 2. Small statue created by ball end micro milling using a 5-axis machine (Sasaki et al. 2004). 2

Figure 3. Profile of micro channel with aspect ratio1.1:1, AlTiN coated WC ball end mill, Φ0.198mm, 0.1µm/tooth chip load, 24m/min speed, 30µm depth, 316L stainless steel, MQL (Dmytro, 2013). 3

Figure 4. a) Macro machining where $h>r_e$ b) Micro machining where $h<r_e$, r_e=radius of cutting edge, h=uncut chip thickness, α=effective rake angle (Aramcharoen and Mativenga, 2009). 8

Figure 5. A static model of chip formation in micro scale milling, r_e=radius of cutting edge, h=uncut chip thickness, h_m=minimum chip thickness (Aramcharoen and Mativenga, 2009). 8

Figure 6. Surface profile of channel formed after ball end milling (Dmytro, 2013).....10

Figure 7. Surface profile generated by a two flute end mill cutter (Wang and Chang, 2004). 11

Figure 8. (a) End milling process and geometry (b) Surface profile for straight cut after end mill cutting (Sutherland and Babin, 1988). 12

Figure 9. Comparison of line roughness measurements and predictions for ferrite (Vogler et al., 2004). 13

Figure 10. Relation between chip load and line roughness (Dmytro, 2013). 14

Figure 11. Surface roughness variation with ratio of underformed/uncut chip thickness to cutting edge radius (r_r) (Aramcharoen and Mativenga, 2009).....15

Figure 12. Dependence of roughness (R_z) with respect to cutting speed (Weule et al., 2001). 15

Figure 13. Percent increase in tool edge radius for coated and uncoated WC tools (Aramcharoen et al., 2008) 17

Figure 14. Comparison of surface finish for uncoated and coated tools, L_c = length of cut (Aramcharoen et al., 2008). 18

Page

Figure 15. SEM images showing growth of BUE at time t=0s, t=15s and t=30s at a test temperature of 450^{o}C, Magnification 420x (Iwata and Ueda, 1980). 21

Figure 16. Cutting speed vs force per unit width (Childs, 2011). 22

Figure 17. Effect of tool vibration on surface topography (a) vibration amplitude: 0µm (b) vibration amplitude: 1µm (c) vibration amplitude: 5 µm (d) vibration amplitude: 15 µm (Peng et al., 2012) 23

Figure 18. Comparison of machined channel with and without runout (Sujeev, 2009). .25

Figure 19. Experimental setup for runout measurements and milling experiments..... 25

Figure 20. Side view of uncoated micro flat end mill showing concavity angle. 28

Figure 21. Sketch of sectional view of slot after micro milling with flat end mill. r_e=radius of cutting edge..... 28

Figure 22. Schematic diagram (side view) of workpiece preparation..... 32

Figure 23. Precision gage block (thickness=3.81mm) with copper strip hanging with support of double side sticky tape. 33

Figure 24. Schematic diagram representing precision gage block and Cu strip thickness measurements with Keyence laser displacement sensor..... 33

Figure 25. Set up for measuring tool offset..... 34

Figure 26. Time series plot at different tool rotation speeds (a) 10,000 RPM. (b) 20,000 RPM. (c) 30,000 RPM. (d) 40,000 RPM. (e) 50,000 RPM. 42

Figure 27. Frequency domain plot at different tool rotational speeds (a) 10,000 RPM. (b) 20,000 RPM. (c) 30,000 RPM. (d) 40,000 RPM. (e) 50,000 RPM. 46

Figure 28. Repeatability and consistency of tool offset values..... 49

Figure 29. Tool rake surface of uncoated WC after machining 4 slots, length 32 mm, Uncoated Φ0.406 mm WC flat end mill, 15-80 m/min speed, 15 µm/tooth chip load, 100 µm depth, dry and MQL, A36 carbon steel workpiece..... 50

Figure 30. Scanning electron microscopy image of chips collected after machining pure titanium, Uncoated WC tool, Φ0.406 mm, 2 flute, 10 m/min speed, 0.2 µm/tooth chip load, 10 µm depth, dry. 51

Page

Figure 31. Machined surface of 316L stainless steel with uncoated WC tool, Φ0.406 mm, 2 flute, 10 m/min speed, 0.05 µm/tooth chip load, 30 µm depth, MQL. .52

Figure 32. Linear density of BUE at center of slot, A36 carbon steel, high speed steel tool, Φ3.175 mm, 12 mm length, 3 µm/tooth chip load, 50 µm depth, dry.....53

Figure 33. Area density of BUE at center of slot, A36 carbon steel, high speed steel tool, Φ3.175 mm, measurement area-15625 μm^2, 3 µm/tooth chip load, 50 µm depth, dry.....54

Figure 34. Average line roughness at center of slot, A36 carbon steel, high speed steel tool, Φ3.175 mm, 3 µm/tooth chip load, 50 µm depth, dry.....54

Figure 35. Predicted and actual line roughness R_a values of slots measured at center. Al 6061-T6, high speed steel tool, Φ3.175 mm, 2 flute, 100 µm depth, dry, 3.5^o concavity angle. 56

Figure 36. Average surface roughness, S_a, A36 carbon steel, uncoated and coated WC tool, Φ3.175mm, 4 flutes, 15 µm/tooth chip load.....58

Figure 37. (a) Uncoated WC tool before machining (b**)** Tool chipping and wear observed on uncoated WC tool. Machining 4 consecutive slots, 32 mm length, 15 m/min and 80 m/min speed, 15 µm/tooth chip load, dry and MQL, 50 µm and 100 µm depth, A36 carbon steel. 59

Figure 38. (a) TiAlN coated WC tool before machining (b) Tool chipping and wear observed on TiAlN coated WC tool. Machining 4 consecutive slots, 32 mm length, 15 m/min and 80 m/min speed, 15 µm/tooth chip load, dry and MQL, 50 µm and 100 µm depth, A36 carbon steel. 60

Figure 39. Built-up-edge formation observed on rake surfaces of uncoated WC tool. Machining 4 consecutive slots, 32 mm length, 15 m/min and 80 m/min speed, 15 µm/tooth chip load, dry and MQL, 50 µm and 100 µm depth, A36 carbon steel. 61

Figure 40. Machined surface of A36 carbon steel. Uncoated WC tool, Φ3.175 mm, 4 flutes, 15 m/min speed, 15 µm/tooth chip load, 100 µm depth, MQL, S_a=0.997µm. 61

Figure 41. Machined surface of A36 carbon steel. Uncoated WC tool, Φ3.175 mm, 4 flute, 80 m/min speed, 15 µm/tooth chip load, 50 µm depth, MQL, S_a=0.584µm. 62

Page

Figure 42. Scanning electron microscopy image of machined 316L stainless steel. Uncoated WC micro mill, Φ0.406 mm, 10 m/min speed, 0.05 µm/tooth chip load, 30 µm depth, MQL. 63

Figure 43. Energy dispersive X-ray spectroscopy (EDS) of BUE. 63

Figure 44. BUE density showing variation for different grayscale. 27 m/min speed, 1 µm/tooth chip load, uncoated WC tool, Φ0.406 mm WC tool, 30 µm depth, MQL. 64

Figure 45. Grayscale image with BUE count on Image Pro software. 316L stainless steel, 44 m/min speed, 0.5 µm/tooth chip load, uncoated WC tool, Φ0.406 mm, 30 µm depth, MQL. 65

Figure 46. BUE density variation in up and down milling within a sample. 316L stainless steel, 27 m/min speed, 1 µm/tooth chip load, uncoated WC tool, Φ0.406 mm, 30 µm depth, MQL. 66

Figure 47. Grayscale image with BUE count on Image Pro software. 316L stainless steel, 10 m/min speed, 0.05 µm/tooth chip load, uncoated WC tool, Φ0.406 mm, 30 µm depth, MQL, up-milling. 67

Figure 48. Grayscale image with BUE count on Image Pro software. 316L stainless steel, 10 m/min speed, 0.05 µm/tooth chip load, uncoated WC tool, Φ0.406 mm, 30 µm depth, MQL, down-milling. 67

Figure 49. BUE Density (average of 20 samples per slot) on micro milled slots. 316L stainless steel, 10-60 m/min speed, 0.05-1 µm/tooth chip load, 30 µm depth, Φ0.406 mm uncoated WC flat end mill, 2 flutes, MQL. 68

Figure 50. (a) Flat end mill showing view area of micro end mill tool. (b) Scanning electron microscopy image of cutting edge of uncoated WC tool, Φ0.406 mm, 10 m/min speed, 0.05 µm/tooth chip load, 30 µm depth, 24 mm milling length, MQL. 69

Figure 51. (a) Flat end mill with arrows pointing towards view area of micro end mill tool. (b) Scanning electron microscopy image of cutting edge. Uncoated WC tool with BUE, Φ0.406 mm, 10 m/min speed, 0.05 µm/tooth chip load, 30 µm depth, 24 mm milling length, MQL. 70

Figure 52. Energy dispersive X-ray spectroscopy results of BUE on tool. 71

Page

Figure 53. (a) Flat end mill showing view area of micro end mill tool. (b) Scanning electron microscopy image of rake surface and cutting edge. Uncoated WC tool with BUE, Φ0.406 mm, 60 m/min speed, 1 µm/tooth chip load, 30 µm depth, 24 mm milling length, MQL. 72

Figure 54. (a) Flat end mill showing view area of micro end mill tool. (b) Scanning electron microscopy image of rake surface and cutting edge. AlTiN WC tool with BUE, Φ0.800 mm, 10 m/min speed, 2-8 µm/tooth chip load, 30 µm depth, 48 mm milling length, MQL. 73

Figure 55. Surface roughness S_a (average of 15 values) measured at center of slot. Micro milling, 316L stainless steel, 10-60 m/min speed, 0.05-1 µm/tooth chip load, 30 µm depth, Φ0.406 mm uncoated WC flat end mill, 2 flutes, MQL. 74

Figure 56. Predicted and actual line roughness, R_a values of slots measured at center. 316L stainless steel, Φ0.406 mm uncoated WC tool, 2 flute, 10-60 m/min speed, 0.05-1 µm/tooth chip load, 30 µm depth, MQL, 7^o concavity angle. 75

Figure 57. Predicted and actual line roughness, R_a values of slots measured at center. .. 76

Figure 58. (a) Top view of new micro tool (b) Top view of micro tool after 24 mm milling distance, 316L stainless steel, 27 m/min speed, 1 µm/tooth chip load, Φ0.406 mm uncoated WC tool, 30 µm depth, MQL. 77

Figure 59 (a) Top view of machined tool superimposed on top view of new micro tool (b) One of the cutting edges magnified to calculate tool wear and chipping after milling 24 mm, 316L stainless steel, 27 m/min speed, 1 µm/tooth chip load, Φ0.406 mm uncoated WC tool, 30 µm depth, MQL. 77

Figure 60. Average tool volumetric loss per machining length after micro machining slots with 10-60 m/min cutting speed, 0.05-1 µm/tooth chip load, 30 µm depth, Φ0.406 mm uncoated WC flat end mill, 2 flutes, 316L stainless steel workpiece. 79

Figure 61. Average tool volumetric loss per machining time after micro machining slots with 10-60 m/min cutting speed, 0.05-1 µm/tooth chip load, 30 µm depth, Φ0.406 mm uncoated WC flat end mill, 2 flutes, 316L stainless steel workpiece. 80

Figure 62. Predicted and actual line roughness, R_a values of slots measured at center. 316L stainless steel, Φ0.406 mm uncoated WC tool, 2 flute, 10-60 m/min speed, 0.05-1 µm/tooth chip load, 30 µm depth, MQL, 7^o concavity angle. 84

LIST OF TABLES

Page

Table 1. Cutting edge radius before and after coating tools (Aramcharoen et al., 2008). 17

Table 2. Comparison of uncoated and TiAlN coated meso end mill cutters (MSC Industrial Supply, 2014). 26

Table 3. Properties of uncoated WC micro tools (Performance Micro Tools, 2014). 27

Table 4. Physical properties of workpiece materials (Azom, 2014) (Steel Grades, 2014). 29

Table 5. Chemical composition of workpiece materials (Azom, 2014) (Steel Grades, 2014). 30

Table 6. Meso milling experimental conditions. 37

Table 7. Micro milling experimental conditions. 38

Table 8. Spindle speed frequencies calculated at various tool rotational speeds. 42

Table 9. Tool runout values measured at different speeds. 45

Table 10. Correlation between Linear density of BUE, Area density of BUE and Line roughness, R_a, A36 carbon steel, 5 m/min speed, high speed steel tool, Φ3.175 mm, 12 mm length, 3 µm/tooth chip load, 50 µm depth, dry. 53

Table 11. Preliminary linear model fit using R statistical software. 58

Table 12. Final linear model fit using R statistical software 59

Table 13. Comparison between material composition of 316L stainless steel and BUE (Azom, 2014) (Steel Grades, 2014). 64

Table 14. EDS of BUE on cutting edge, Uncoated WC tool with BUE, Φ0.406 mm, 10 m/min speed, 0.05 µm/tooth chip load, 30 µm depth, 24 mm milling length, MQL. 71

Table 15. Tool wear and chipping for micro milling experimental conditions, 316L stainless steel workpiece, Φ0.406 mm uncoated WC tool, MQL 78

Table 16. Final model using R statistical software for difference between predicted roughness and actual roughness 81

Page

Table 17. Final model using R statistical software for difference between predicted roughness and actual roughness.....82

1. INTRODUCTION

Micro machining refers to the processes in which features less than 0.1 mm can be fabricated. Motivation for producing features of micro size over time has always been increasingly popular. Development of electrical and computer technology using silicon has made it possible to achieve micro machining with high precision and accuracy. However for non-silicon materials such as titanium and stainless steel alloys, prediction of cutting mechanism and output features such as surface roughness, cutting force, burr formation and tool wear has been anything but simple. The complexity involved behind machining of micro features is complex and more machining parameters need to be controlled to achieve required objectives when compared to macro machining. The machining principles that generally apply for macro machining are not completely relevant in micromachining.

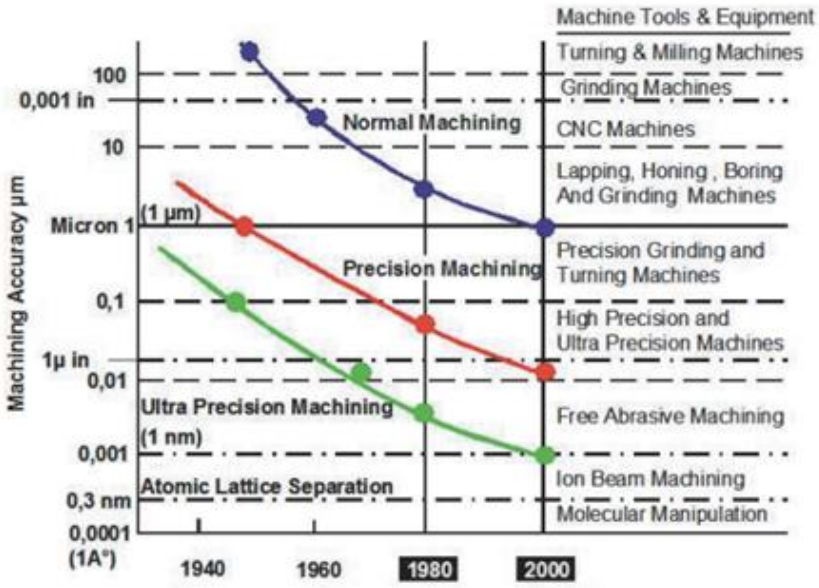

Figure 1. Accuracy and precision achievable in machining (McKeown, 1986).

Figure 1 represents manufacturing precision and accuracy curves which were first proposed by Taniguchi (1980) and later modified McKeown (1986). With advancement in the realm of science and technology, CNC machines with positional accuracies in the range of a few nanometers have been developed in the early 1990's (Byrne et al., 2003). Complex micro part features are fabricated as their demand is on the rise owing to increased usage in fuel injection nozzles in aerospace and automobile industries, integrated circuit packages in semi-conductor industry, stent and drug delivery systems in bio-medical industry (Bourne, 2007; Liu et al., 2004).

Usage of stainless steel in these applications is gaining prominence due to its properties such as high ductility, toughness, corrosion and oxidation resistance. The goal of micro machining is to fabricate these small features with high accuracy and precision.

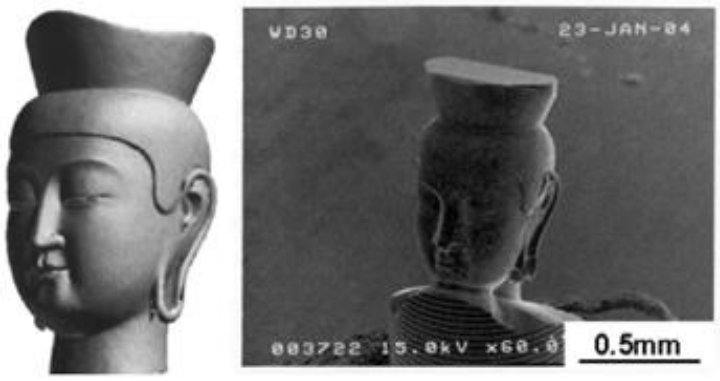

Figure 2. Small statue created by ball end micro milling using a 5-axis machine (Sasaki et al. 2004).

An example of complex part that could be fabricated is shown in Figure 2. Sasaki et al. (2004) machined gold for 36 hours using a single crystal diamond ball end mill on a

5-axis machine to fabricate this statue. Also features with high aspect ratios can be fabricated in micro milling with ease over other non-traditional fabrication methods as shown in Figure 3 (Dmytro, 2013). Various non-traditional micro fabrication processes are known to exist to machine these features. In this study, micro milling has been chosen due to its flexibility in machining complex part features.

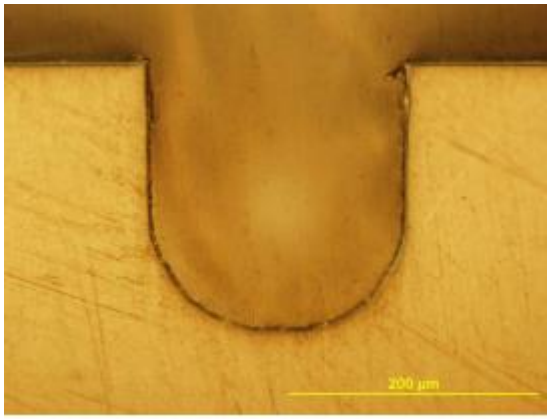

Figure 3. Profile of micro channel with aspect ratio1.1:1, AlTiN coated WC ball end mill, Φ0.198mm, 0.1µm/tooth chip load, 24m/min speed, 30µm depth, 316L stainless steel, MQL (Dmytro, 2013).

1.1 ISSUES WITH NON-TRADITIONAL MICRO MANUFACTURING TECHNIQUES

Both traditional and non-traditional techniques can produce micro features. Although many non-traditional processes have been developed to achieve the same level of accuracy and precision as in traditional machining process, they have their own limitations. Laser beam machining and electron beam machining can machine almost any available material as the heat generated during the process can exceed the melting point

of all known materials. However the heat affected zone is difficult to control (Masuzawa, 2000).

Photo etching can specify a pattern with good precision with etching proceeding iso-tropically, which restricts the application of this method to only semiconductor products. (Masuzawa, 2000). Rapid prototyping techniques like stereo-lithography can also be used in micro fabrication with major drawback being the limited availability of materials.

Micro-electro discharge machining (μEDM) is a machining process which removes material by melting and vaporization. High machining accuracy is easily achieved by μEDM whereas high machining speed is yet to be reached. Although the use of deionized water improves machining speed to an extent, it does so at the expense of machining accuracy (Masaki et al., 1990).

Traditional methods for micro fabrication include micro milling which is an extension of macro milling on a smaller scale. In this study, micro milling has been chosen due to its flexibility in machining complex part features. Also features with high aspect ratios can be fabricated using micro milling with ease over other non-traditional fabrication methods. One of the major limitations of micro milling is the formation of built-up-edge (BUE). The presence of BUE on the machined surface results in higher average surface roughness values. Detection of BUE is critical so as to avoid its formation for producing high quality micro part features. Since BUE related information is limited in micro milling, this work is an experimental study on optimizing machining parameters for BUE formation.

2. OBJECTIVE AND SCOPE

The primary objective of this study is

1. Study BUE formation in micro milling
2. Predict surface roughness and effect of BUE
3. Optimize process parameters to obtain best surface with minimum BUE

The scope of this study limits to:

1. Micro milling of 316L stainless steel using uncoated and coated tungsten carbide flat end mill cutters with diameters less than <0.500 mm.
2. Meso milling of Aluminum 6061-T6 with high speed steel cutter.
3. Meso milling of A36 carbon steel with coated and uncoated tungsten carbide flat end mill cutters of diameters 3 mm.
4. Applying minimum quantity lubrication through micro mist.

3. LITERATURE REVIEW

3.1 MACHINING VARIABLES IN MICRO MACHINING

Micro and macro machining are different in various aspects especially cutting mechanism, chip formation, surface generation etc. The motivation and knowledge of macro machining could be slightly extended to micro machining but cannot be completely applied. Since the availability of relevant literature in micro machining is limited, review of related macro machining literature is cited for reference.

3.1.1 Uncut chip thickness and edge radius

A lot of research has been done in the field of uncut chip thickness and its significance in micro machining. Its importance has been discussed by Ikawa et al. (1992) at length although studies have been conducted before that in 1988. Furukawa and Moronuki (1988) observed increase in specific cutting force for aluminum alloy with different grain sizes below cutting depths of 3 μm and reached normal standard cutting force values at higher depths. This might be due to sliding of aluminum alloy under flank face due to elastic recovery at small depths. They concluded that a minimum depth of cut is required.

Ikawa et al. (1988) machined copper using a specially prepared diamond cutting edge and produced chips in the range of 1 nm. The cutting edge sharpness was less than 1nm. They developed atomistic models to validate their claim that chips are formed only if thickness of cut is above a critical value. They further extended their study on minimum thickness of cut by applying molecular dynamics simulation on accuracy in micro cutting

which they found out to be about 1nm or less and called it minimum thickness of cut below which a chip is not formed (Shimada et al., 1993).

Yuan et al. (1996) studied the relation between tool edge radius and minimum chip thickness in ultra-machining of aluminum alloys with diamond coated cutting tools and derived mathematical equations based on cutting forces to estimate minimum thickness of cut. They found that minimum chip thickness was a function of coefficient of friction (μ) between workpiece and tool material and estimated minimum chip thickness for different combinations of workpiece and tool materials. They found it to be between 20-40% of tool edge radius in cutting most of the materials.

Lai et al. (2008) used finite element models to simulate machining of Oxygen-free high thermal conductivity (OFHC) copper with minimum chip thickness between 10-30% of tool edge radius and observed chip formation for 30% of tool edge radius when the cutting edge radius is around 2μm. After a series of experiments, they recommended minimum thickness of cut for machining OFHC copper to be 25% of cutter edge radius.

Aramcharoen and Mativenga (2009) proposed a conclusive model on minimum cut thickness with respect to tool edge radius as evident from Figures 4 and 5. They suggested that minimum thickness of cut depends on sharpness of cutting edge and tool workpiece material affinity. They suggested that chip formation in micro machining does not follow the same principles of macro machining, and its formation is uncommon in micro machining unless uncut chip thickness is greater than tool edge radius.

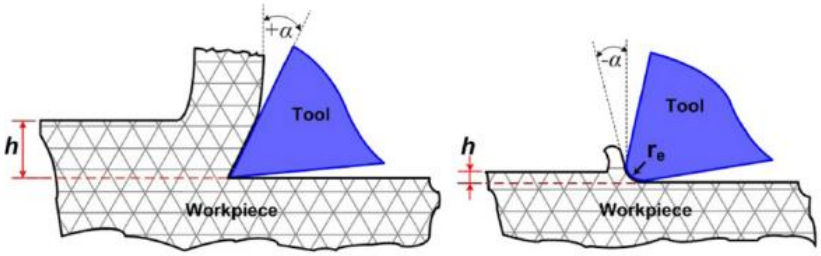

a) b)

Figure 4. a) Macro machining where $h>r_e$ b) Micro machining where $h<r_e$, r_e=radius of cutting edge, h=uncut chip thickness, α=effective rake angle (Aramcharoen and Mativenga, 2009).

They proposed three cutting mechanisms in micro machining depending on uncut chip thickness (depth of cut) h, minimum chip thickness h_m and tool radius of cutting edge r_e.

1) $h<h_m<r_e$

In Figure 5(a), the uncut chip thickness is less than tool edge radius. When this happens, elastic deformation of workpiece takes place resulting in no chip formation. A tool has negative rake angle which encourages the rake surface of tool to push forward the workpiece material resulting in ploughing and no chip formation **(**Aramcharoen and Mativenga, 2009)**.**

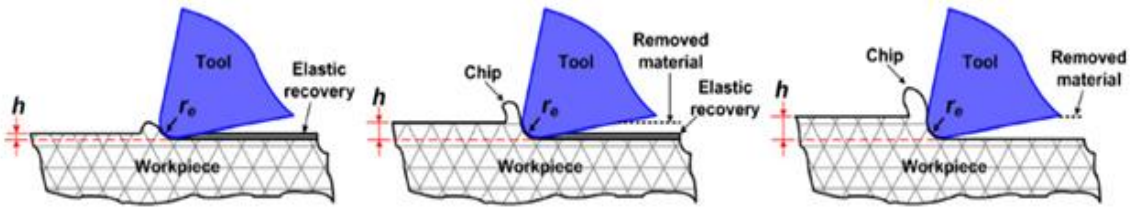

a) $h<h_m<r_e$ b) $h=h_m=r_e$ c) $h>h_m>r_e$

Figure 5. A static model of chip formation in micro scale milling, r_e=radius of cutting edge, h=uncut chip thickness, h_m=minimum chip thickness (Aramcharoen and Mativenga, 2009).

2) $h=h_m=r_e$

As this uncut chip thickness value increases and equals tool edge radius as shown in Figure 5(b), plastic deformation dominates over elastic deformation. Transition from ploughing or elastic deformation to cutting or plastic deformation is observed accompanied by chip formation.

3) $h>h_m>r_e$

As the uncut chip thickness is greater than tool edge radius, plastic deformation of workpiece material or chip formation is observed. (Figure 5(c)).

3.2 SURFACE FINISH MODELING

In most of the research concerning optimizing surface finish, a surface model is either derived mathematically or simulated to predict average roughness values. These values are then compared with actual values obtained, and deviation from predicted average roughness is calculated and explained. To achieve the best possible finish, different combination of machining parameters are tried to find the best combination that results in small values of average surface roughness (S_a).

Dmytro (2013) predicted line roughness at the center of slot for micro ball end milling under the assumptions that depth of cut was large enough to avoid ploughing and cutting tool edge was sharp. Finished surface model was developed to predict line roughness shown in Figure 6 and equation (1). This model predicts line roughness reasonably well, when the chip load is above 50 µm/tooth.

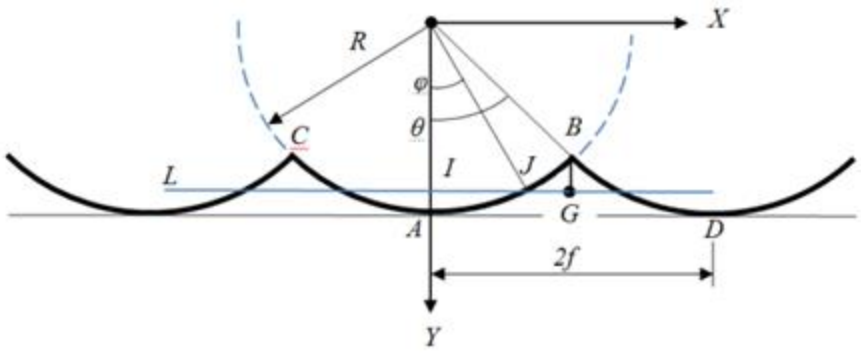

Figure 6. Surface profile of channel formed after ball end milling (Dmytro, 2013).

$$R_a = 0.2568\frac{f^2}{D} \tag{1}$$

where R_a = Line roughness (mm)

f = Chip load (mm/tooth)

D = Diameter of tool (mm)

Wang and Chang (2004) simulated surface generated by 2 flute flat end mills (Figure 7). They conducted experiments with 5 factors, each at 5 levels, including cutting speed, chip load, depth of cut, concavity angle and axial relief angle to verify their mathematical equation (2).

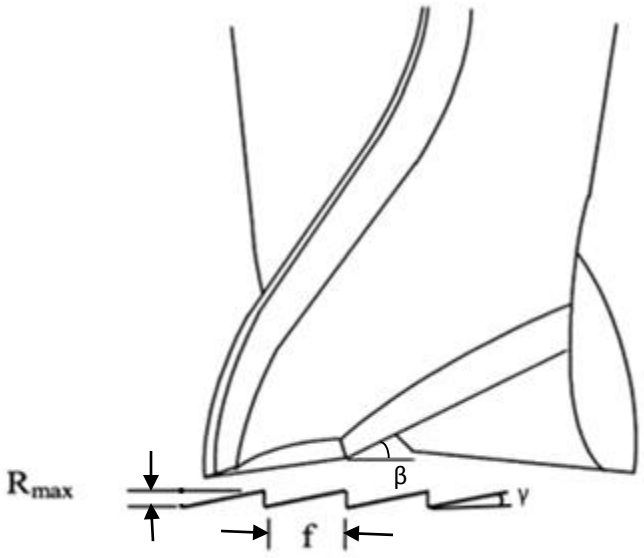

Figure 7. Surface profile generated by a two flute end mill cutter (Wang and Chang, 2004).

$$R_a = \frac{f}{4\ cot\gamma} \tag{2}$$

where R_a = Line roughness (mm)

R_{max} = Maximum height of surface (mm)

f = Chip load (mm/tooth)

γ = Concavity angle (^{o})

β = Axial relief angle (^{o})

Using response surface methodology (RSM) and experimental analysis, Wang and Chang (2004) found that for dry cutting, significant parameters affecting average roughness were cutting speed, chip load, concavity and axial relief angles. For wet cutting, chip load and concavity angles were the critical parameters. They found that, when the concavity angle is greater than 2.5^0, an increase in chip load, concavity angle and axial

relief angles would increase the surface roughness. However, equation (2) doesn't show the effect of axial relief angle on surface roughness.

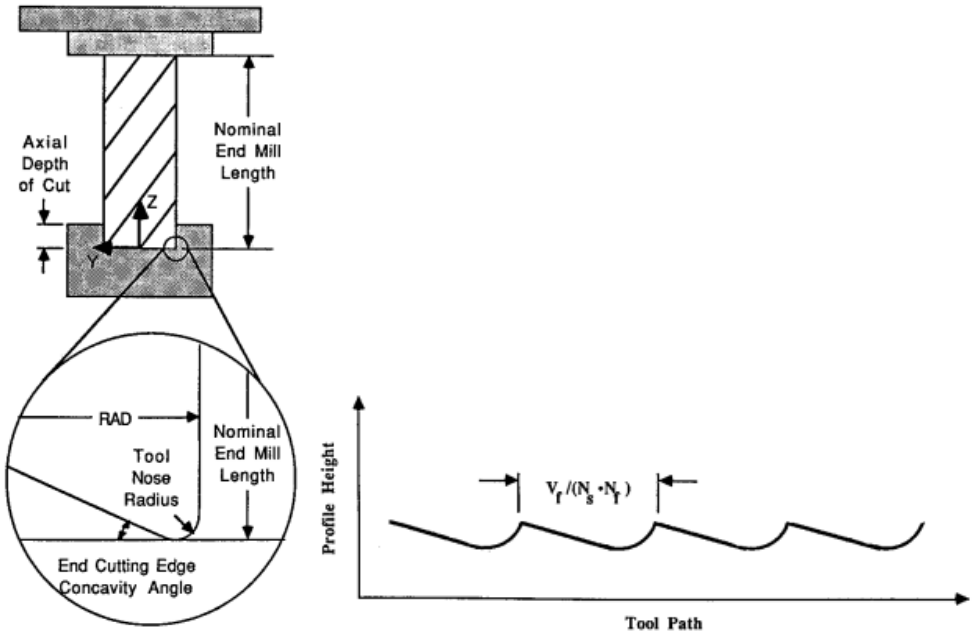

(a) (b)

Figure 8. (a) End milling process and geometry (b) Surface profile for straight cut after end mill cutting (Sutherland and Babin, 1988).

Another study was conducted into simulating surface generated by 4 flute flat end mill by Sutherland and Babin (1988) as shown in Figure 8. They concluded from their model that chip load and concavity angle are directly responsible for increasing average line roughness.

3.2.1 Effect of chip load and cutting speed on surface finish

Chip load is one of the critical parameters that defines the material removal rate (MRR) and the main goal of machining in industrial environment has always been to

achieve a high MRR. Cui et al. (2012) machined AISI H13 steel with a tool diameter of 125 mm with tungsten carbide inserts and found that chip load is directly proportional to surface roughness. In a study by Zawawi et al. (2014) on machining aluminum and P20 steel with a 12 mm diameter end mill, they found that surface roughness deteriorates by increasing chip loads. However, in micro machining, there has always been a debate on the effect of chip load on surface finish.

Vogler et al. (2004) micro milled ferrite and pearlite at chip loads from 0.25-3 µm/tooth, spindle speed of 120000 RPM, and with axial depth of cuts at 50 µm and 100 µm. They observed that a chip load of 3.0 µm/tooth has a lower line roughness compared to a chip load of 0.25 µm/tooth (Figure 9). They compared their experimental results with predicted results using finite element analysis and found the prediction to be in close agreement.

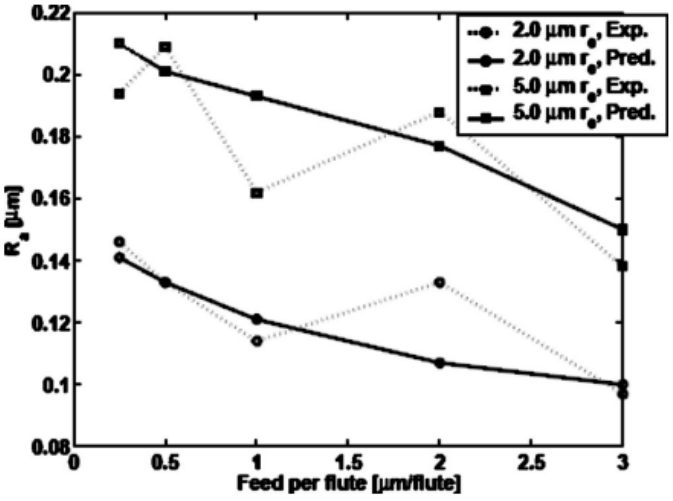

Figure 9. Comparison of line roughness measurements and predictions for ferrite (Vogler et al., 2004).

However, another study conducted by Dmytro (2013) on micromachining of ball end mills of 316L Stainless steel and Ni-Ti alloys shows that surface roughness increases with chip load. It is clearly evident from Figure 10 that increase in chip load with a constant cutter diameter, resulted in higher average line roughness.

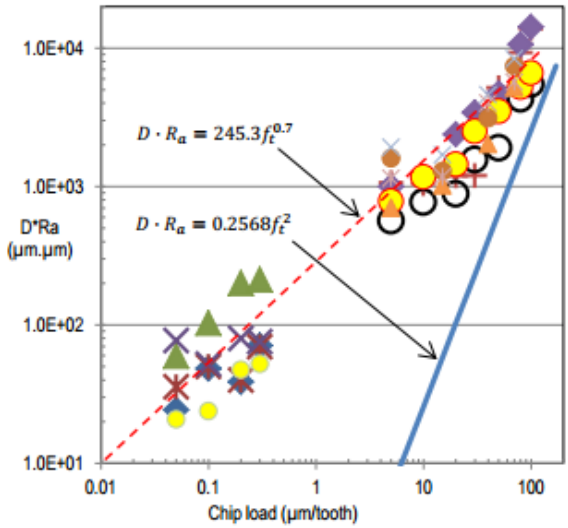

Figure 10. Relation between chip load and line roughness (Dmytro, 2013).

Another important study on uncut chip thickness and surface finish was done by Aramcharoen and Mativenga (2009) in which they machined H13 hardened steel at different ratios of uncut chip thickness to tool edge radius (r_r) as shown in Figure 11.

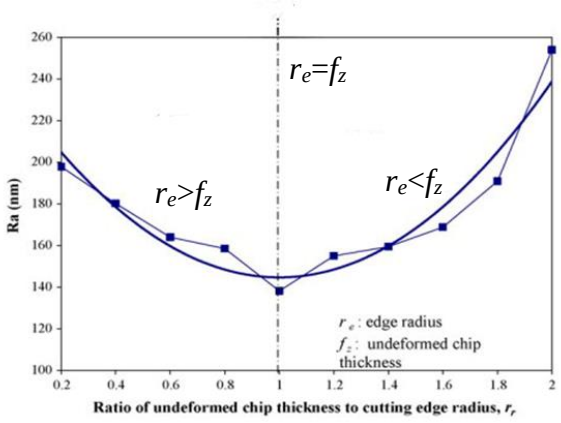

Figure 11. Surface roughness variation with ratio of underformed/uncut chip thickness to cutting edge radius (r_r) (Aramcharoen and Mativenga, 2009)

They based their study on 3 different cases.

1. r_r < 1, the surface roughness values decreases with increase in chip load as observed by Vogler et al., (2004).
2. r_r > 1, chip load has a positive correlation with surface roughness. This study is in acceptance with the study conducted by Dmytro (2013) on micromachining of stainless steel using ball end mills.
3. r_r = 1, the best surface finish occurs.

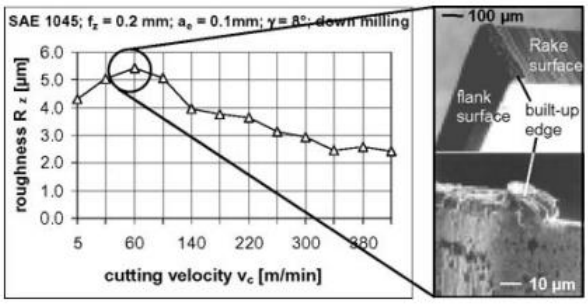

Figure 12. Dependence of roughness (R_z) with respect to cutting speed (Weule et al., 2001).

Weule et al., (2001) milled SAE 1045 steel with cutting velocities ranging from 5 m/min to 420 m/min. Chip load, depth of cut and type of cutting (up and down milling) were other variable parameters. They found that surface roughness decreases with increase in cutting velocity except for a small region (around 1-60 m/min) (Figure 12). This suggests the possibility of BUE formation on the rake surface of tool at these cutting speeds.

3.3.2 Tool coatings

Coatings (both soft and hard) on tungsten carbide tools have been effectively and efficiently used in macro machining till date with fair amount of decrease in cutting forces and surface finish. Tool coatings protect the cutting edge by forming an extra layer over rake surface and cutting edges and thus protecting the cutting edge from wear, resulting in longer tool life. Also depending upon the type of tool coating used, coefficient of friction between the coating material and workpiece material would be reduced, thereby ensuring reduced friction and temperatures at tool chip interface.

Aramchareon et al. (2008) studied the effect of hard coatings in micro milling of hardened H13 tool steel (45 HRC) using flat end mills under dry conditions. They evaluated effect of TiN, TiCN, TiAlN, CrN and CrTiAlN coatings on tools made from ultra-fine tungsten carbide structure. Also coating effectively increases the tool edge radius by almost 2 times. Details of cutting edge radius before and after for different types of coating are provided in Table 1. For most of micro cutting applications coating thickness is in the range of 1.5 ± 0.15 μm. The cutting edge radius before and after coating was measured on a scanning electron microscope (SEM).

Table 1. Cutting edge radius before and after coating tools (Aramcharoen et al., 2008).

Tool	Cutting edge radius$_{avg}$ (μm)		Difference of edge radius (μm)	Coating thickness (μm)
	Before coating	After coating		
Uncoated	2.07	–	–	–
TiN	0.76	2.05	1.29	1.38
TiCN	1.01	2.26	1.25	1.50
TiAlN	1.06	2.30	1.24	1.42
CrN	0.87	2.30	1.43	1.40
CrTiAlN	1.38	2.44	1.06	1.59

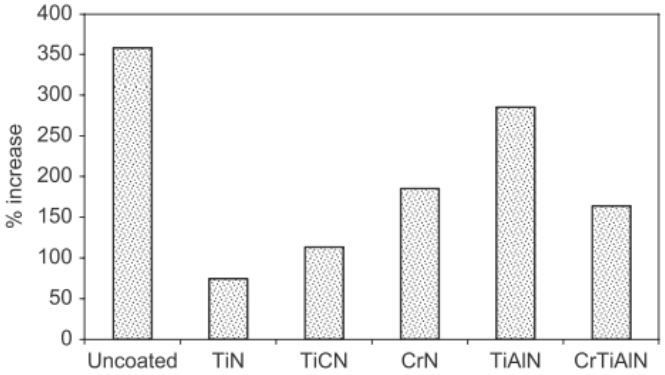

Figure 13. Percent increase in tool edge radius for coated and uncoated WC tools (Aramcharoen et al., 2008)

Figure 13 shows cutting edge radius enlargement after machining hardened H13 tool steel for a length of cut (L_c) of 20-25 mm. Overall, coated micro end mills perform better than uncoated tools due to improved friction characteristics at workpiece tool interface. Among coated tools TiN coating performs best in terms of percentage enlargement of cutting edge radius.

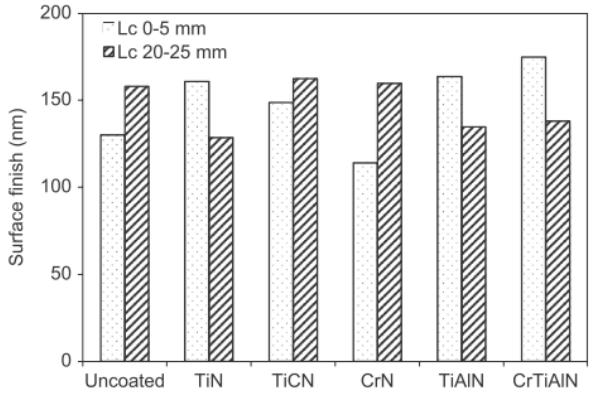

Figure 14. Comparison of surface finish for uncoated and coated tools, L_c = length of cut (Aramcharoen et al., 2008).

Figure 14 compares surface finish at the beginning of slot and after machining a length of 20-25 mm with both coated and uncoated tools. CrN tool initially shows promise of better performance over all other tools, but slowly deteriorates upon time. At the end of 20-25 mm length, surface finish of uncoated, TiCN and CrN tools are poor due to large flank wear and delamination of coating (Aramcharoen et al., 2008). However, a rationale behind improvement in surface finish for TiN, TiAlN and CrTiAlN was not provided.

3.3 BUILT-UP-EDGE MECHANISM AND EFFECTS

Built-up-edge is a phenomenon in which the chip material welds or sticks to the tool rake surface. This extra layer of workpiece material protects the original rake surface from wear. It also acts as a new cutting edge covering the original cutting edge thus modifying the tool geometry. This BUE occurs quite frequently while machining ductile materials such as stainless steel and mainly effects cutting forces, vibrations, tool life and surface finish. The BUE formation is dynamic in the sense that, it increases in size, breaks

off from the rake surface of the tool and forms again. Research on BUE formation has always been a topic of prime interest in the realm of manufacturing.

Heginbotham and Gogia (1961) had shown that cutting speed has a major influence on the formation of BUE. At about the same time, Zorev (1966) has reinforced that cutting speed has significant impact on the formation of BUE and proposed that cutting speeds for BUE formation in machining carbon steels are in the range of 1-50 m/min.

Sukvittayawong and Inasaki (1994) measured cutting force to detect BUE in turning process. Their assumption was based on the fact that, whenever BUE was formed on the face of the rake, the chip was no longer moving on the rake surface but on the BUE surface. This led to a negative effective end rake angle (ϕ), resulting in higher cutting forces from Merchants equation (Groover, 2004).

$$F_c = F_s * \frac{\cos(\delta - \phi)}{\cos(\theta + \delta - \phi)} \quad (3)$$

where F_c = cutting force (N)

F_s = shearing force (N)

δ = friction angle (^{o})

ϕ = end rake angle (^{o})

θ = shear plane angle (^{o})

As cutting speed was increased beyond a critical point, BUE breaks, resulting in positive rake angle, decreasing cutting forces again. This cyclic process of increase and decrease in cutting forces was used to detect formation of BUE. This increase in cutting force, however could be attributed to other machining changes like tool wear. There was

no particular reason explained why this variation in cutting force occurs only due to BUE formation.

Iwata and Ueda (1980) machined low carbon steel with high speed SKH-9 tool at cutting speed of 0.15 mm/min and test temperatures between 350-500 ^{o}C at tool rake surface. They proposed a complicated mechanism for formation of BUE based on SEM images of machining observed over time (Figure 15). They observed workpiece material to appear around the cutting edge of the tool. Consequently, they found two cracks: one below the flank face which grows in the primary shear zone along a slip line and other ahead of rake surface at a distance from the cutting edge. At this stage BUE becomes clearly evident and continues to grow along these cracks. The crack growth is in the region of severe strain concentration which starts from the current position of crack tip and continues to grow along a slip line.

This reinforces the fact that fracture behavior of workpiece material plays a significant role in BUE formation in addition to the adhesion property. Below 350-500^{o}C, there is not sufficient adhesion between workpiece and tool material to support formation of BUE while above this range the ability of material to recover its ductility inhibits crack formation which is necessary for BUE formation.

Figure 15. SEM images showing growth of BUE at time t=0s, t=15s and t=30s at a test temperature of 450^{o}C, Magnification 420x (Iwata and Ueda, 1980).

Formation of BUE has always been difficult to predict. A lot of research has been done to quantify and predict BUE formation. Fang et al. (2010) used a Neural network approach and developed Resource Allocation Network (RAN) and Multilayer Perceptron (MLP) Network models for round and sharp cutting edges to predict BUE formation in orthogonal machining of 2024-T351 aluminum alloy, corresponding to multitude of inputs including cutting speed, feed rate, cutting force, thrust force and vibration amplitude. Experiments were conducted at different extremes of speed (26 levels from 0.80-250 m/min) and feed rates (8 levels from 0.01-0.3 mm/rev). Based on input parameters they were able to classify three stages of BUE formation. When the cutting speed was below 20 m/min, BUE formation occurred at tool rake surface and grew in size. When the cutting speed was between 20-100 m/min, BUE formation is intermittent. At high cutting speeds, over 100 m/min, there is no BUE formation.

Childs (2011) used finite element analysis (FEA) to simulate machining of a type of carbon steel using cemented carbide tool at cutting speeds ranging from 1-150 m/min. His results indicated the BUE was significant in the speed range of 1-60 m/min. Cutting

force and thrust force per unit width were used to compare BUE formation for different speed ranges (Figure 16). Simulation results showed that BUE was observed when the temperature range at the rake chip interface was between 300-500^{o}C, which agreed with study from Iwata and Ueda (1980).

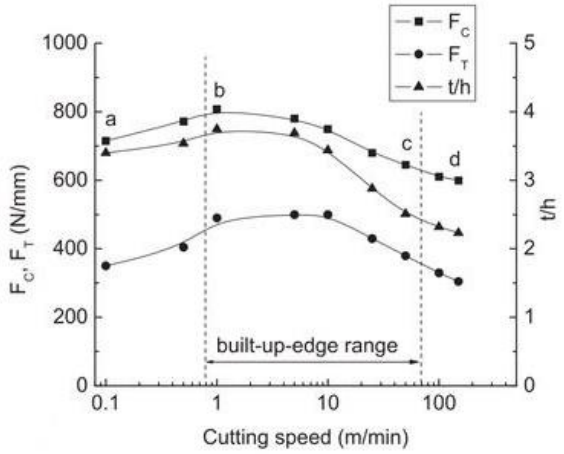

Figure 16. Cutting speed vs force per unit width (Childs, 2011).

Shahabi and Ratnam (2010) proposed an on-site inspection technique to detect and measure BUE using machine vision approach. They used subtraction method and polar-radius transformation algorithms on images captured by a high resolution CCD camera to detect BUE. Actual images of tools before and after cutting are aligned and image of tool before cutting is subtracted from image of tool after cutting, to find area of BUE. They found both the methods to perform within a mean difference of 6.5%.

3.4 STUDY OF TOOL VIBRATION ON SURFACE TOPOGRAPHY

Tool vibration is an inseparable phenomenon present and has a direct influence on the final surface produced especially when the tool vibration and surface finish are in the

same scale. Peng et al. (2012) simulated surfaces by using a 1mm diameter ball end mill, with a constant chip load of 80 µm/tooth, spindle speed of 7500 RPM and tool radius of 0.5 mm. They found that with increase in vibration amplitude, average surface roughness increases from 0.76 µm without vibration to 3.4 µm with vibration of 15 µm (Figure 17).

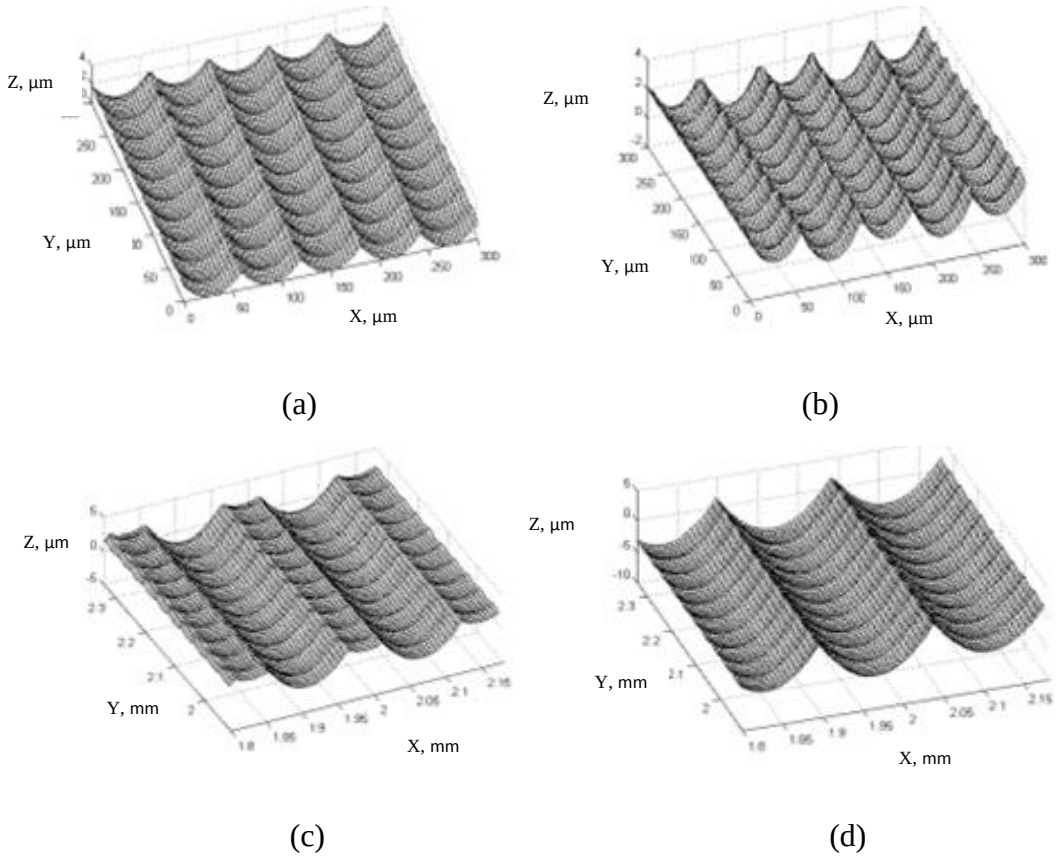

Figure 17. Effect of tool vibration on surface topography (a) vibration amplitude: 0µm (b) vibration amplitude: 1µm (c) vibration amplitude: 5 µm (d) vibration amplitude: 15 µm (Peng et al., 2012).

4. EXPERIMENTS

4.1 LIST OF EQUIPMENT

A variety of equipment have been used throughout the experimentation phase. These equipment can be broadly classified into machining equipment, data collection equipment and metrology equipment. A brief introduction on machines and their usage is described in the experiment section. A detailed list of specifications is provided in Appendix A.

1. HAAS OM2 milling machine
2. CLAUSING CSG818H Surface Grinder
3. UNIST lubrication system
4. KEYENCE laser displacement sensor (LK-G series)
5. OLYMPUS optical microscope
6. ZYGO ZeGage 3D optical surface profiler
7. TESCAN Vega LM3
8. UNI-T M890G digital multimeter
9. Metason 200 ultrasonic cleaner

4.2 EQUIPMENT CALIBRATIONS

4.2.1 Runout measurements

Tool runout in simple terms is imperfect alignment of tool in the spindle. Presence of tool runout cuts unequal quantities of material by each tooth. Tool runout is considered negligible in macro machining since runout is very small compared to slot width. However

in micro machining it is highly significant as tool runout is comparable to the slot width and hence even a small value of runout can result in inaccurate slot widths (Figure 18).

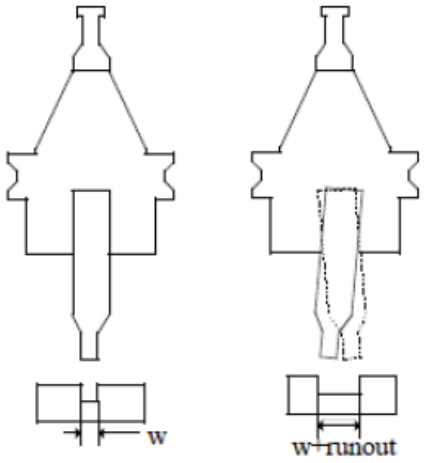

Figure 18. Comparison of machined channel with and without runout (Sujeev, 2009).

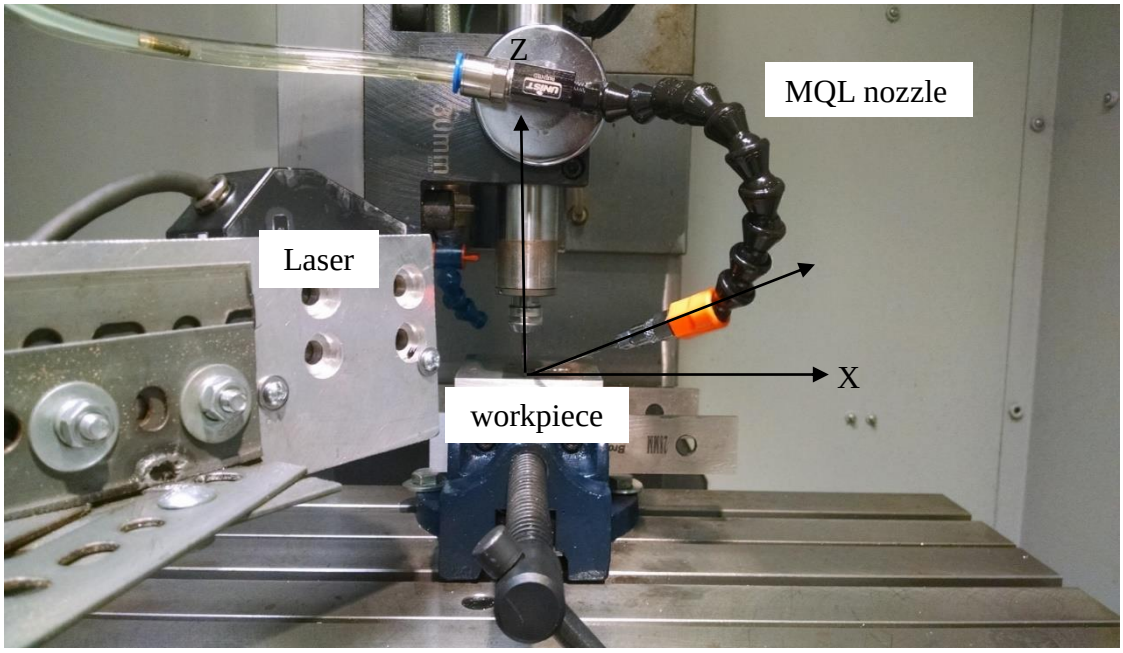

Figure 19. Experimental setup for runout measurements and milling experiments.

Keyence laser displacement sensor was used to measure tool runout. It was mounted on a rigid stand, independent of machine frame (Figure 19). Fast Fourier Transformations (FFT) were used to obtain frequency domain graphs to analyze the components of output signal. The time domain and frequency graphs were plotted in MATLAB. A Φ3.175mm plug gage was used to measure tool runout at tool rotational speeds ranging from 10,000-50,000 RPM in uniform increments of 10,000 RPM.

4.3 EXPERIMENTS

4.3.1 Tool specifications

Two sizes of milling cutters were used for the experiments. Uncoated high speed steel tool with tool diameter of 3.175 mm was used for machining aluminum 6061-T6. Coated and uncoated tungsten carbide (WC) flat end mills with tool diameter of 3.175 mm were used for meso milling experiments with A36 carbon steel (Table 2).

Table 2. Comparison of uncoated and TiAlN coated meso end mill cutters (MSC Industrial Supply, 2014).

Tool material	High speed steel	Tungsten carbide	Tungsten carbide
Type of coating	Uncoated	Uncoated	TiAlN
Number of flutes	2	4	4
Cutter diameter, mm	3.175	3.175	3.175
Shank diameter, mm	3.175	3.175	3.175
Cutter length, mm	15.830	15.830	8.830
Tool length, mm	38.320	38.320	38.320
Concavity angle (average of 10 measurements per flute, 2 flutes per tool)	3.5^o	6.2^o	11.5^o
Standard deviation of concavity angle	0.15^o	0.13^o	0.22^o

Micro flat end mills were used to mill 316L stainless steel. The diameter of these tools were 0.406 mm (TS-2-0160-S). A detailed list of tool specifications and properties is given in Table 3.

Table 3. Properties of uncoated WC micro tools (Performance Micro Tools, 2014).

Tool material	μ grained tungsten	μ grained tungsten
Type of coating	uncoated	AlTiN coated
Number of flutes	2	1
Cutter diameter, mm	0.406	0.8
Shank diameter, mm	3.175	3.175
Flute length, mm	0.6096	11
Tool length, mm	38.1	38.1
Concavity angle	7^o	5.2^o
Cutting edge radius, r_e, μm (Average of 10 measurements on both sides of machined slot)	2.21	3.6

The concavity angle for meso tools was measured using the Olympus optical microscope. The tool holder was placed along the Y-axis of the optical microscope table. A rectangle box was used as a reference to measure the angle accurately (Figure 20). The angle measurement was done using the measurement features in the embedded optical microscope software. However, the concavity angle for a micro tool was obtained from the tool manufacturer (Performance Micro Tools, 2014).

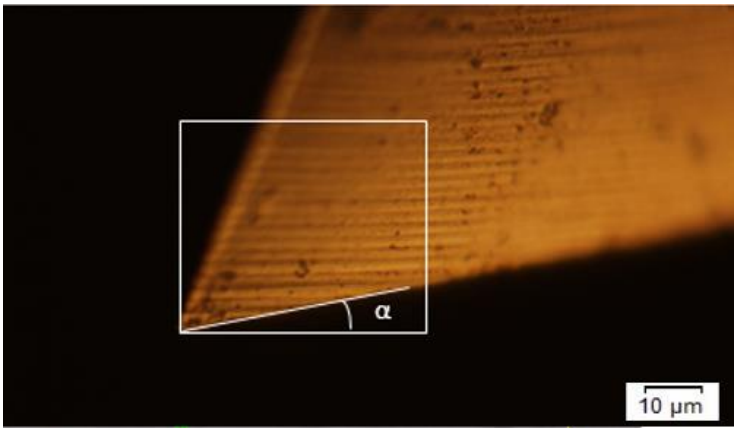

Figure 20. Side view of uncoated micro flat end mill showing concavity angle.

Figure 21. Sketch of sectional view of slot after micro milling with flat end mill.
r_e=radius of cutting edge

Figure 21 shows cross sectional view of slot after machining with a micro end mill. Since the tool geometry is replicated on the slot, measurement of radius of cutting edge (r_e) was done at the beginning of the slot, as the tool remains new at the beginning.

4.3.2 Workpiece material properties

Three different materials were chosen to conduct experiments.

- Aluminum 6061 T6 was initially machined on meso scale using high speed steel tool (Φ3.175 mm) to validate the theoretically derived average line roughness equation.
- A36 carbon steel was chosen to conduct experiments on meso scale with tungsten carbide tools (Φ3.175 mm) to investigate significant factors effecting the quality of surface and BUE formation. These critical factors were later varied during designing experiments in micro milling.
- 316L stainless steel material has been picked for micro milling experiments owing to its vast application in the realm of medical applications.

The physical properties and chemical composition of the above materials can be found in Table 4 and Table 5 respectively.

Table 4. Physical properties of workpiece materials (Azom, 2014) (Steel Grades, 2014).

Material of workpiece	**Yield strength (MPa)**	**Ultimate tensile strength (MPa)**	**Modulus of elasticity (GPa)**	**Hardness (R_B)**	**Density (g/cm^3)**
Al-6061	260-310	207	69	95-97	2.7
A36 carbon steel	250	400-550	200	67.0-83.0	7.85
316L stainless steel	170	485	193	95	8.0
Pure titanium	170	240	21-69	70	6.45

Table 5. Chemical composition of workpiece materials (Azom, 2014) (Steel Grades, 2014).

Workpiece material	**Chemical composition (weight %)**
Aluminum 6061 T6	0.8-1.2 Mg, 0.4-0.8 Si, ≤0.7 Fe, 0.15-0.4 Cu, ≤0.25 Zn, ≤0.15 Ti, ≤0.15 Mn, 0.04-0.35 Cr, Balance Al
A36 carbon steel	0.25-0.29 C, 0.02 Cu, 98.0 Fe, 1.03 Mn, 0.04 P, 0.28 Si, ≤0.05 S
316L stainless steel	≤0.03 C, ≤2.0 Mn, ≤0.75 Si, ≤0.045 P, ≤0.03 S, 16.0-18.0 Cr, 2.0-3.0 Mo, 10.0-14.0 Ni, Balance Fe
Pure titanium	<0.03 N, <1 C, <0.18 O, <0.2 Fe, Balance Ti

4.3.3 Experimental procedure for meso and micro milling

All the experiments were conducted on HAAS OM2 CNC milling machine. The maximum tool rotation speed achievable in the machine is 50,000 RPM with a repeatability of 3 μm (HAAS, 2014).

4.3.3.1 Workpiece preparation

Steps for workpiece preparation are similar for A36 carbon steel and 316L stainless steel. However for meso milling of aluminum 6061-T6, a block of aluminum milled to dimensions 85 mmX75 mmX17 mm was sufficient.

For machining A36 carbon steel, plates were milled to dimensions of 60 mmX75 mmX5 mm and its top surface was ground on a CLAUSING CSG818H surface grinder.

The surfaces were ground for oxide removal and flatness/parallelism requirement. Cold rolled 316L stainless steel plates of dimensions 50 mmX90 mmX0.5 mm were used.

Steps for workpiece preparation (meso and micro milling):

1. An aluminum 6061-T6 block was milled to dimensions 85 mmX75 mmX17 mm.
2. The top surface of aluminum was cleaned with 70% isopropyl alcohol to get rid of dirt and oil.
3. The aluminum block was used as a base to support and raise the height of A36 carbon steel and 316L stainless steel. Parallel bars were further used to raise the workpiece height and ensure that the top surface of workpiece was parallel to the vice. Hence the aluminum block was placed on hot plate as shown in Figure 22 for heating.
4. Mounting wax sticks (P/N MWM070, melting point=70 ^{o}C) was melted on the top surface of aluminum block and this wax was smeared all across the surface to ensure uniformity.
5. After the wax was melted, workpiece material (A36 carbon steel or 316L stainless steel) was carefully placed on the aluminum block and weight added on the top to remove any air that might have been trapped inside the molten wax.
6. The workpiece was allowed to cool for about 1.5-2 hours to allow for wax to solidify.

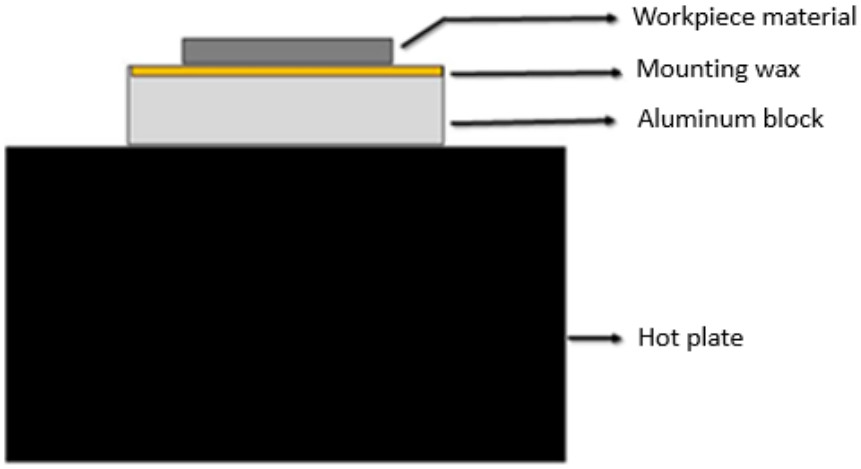

Figure 22. Schematic diagram (side view) of workpiece preparation.

4.3.3.2 Tool offset

Tool is to be repositioned in Z-direction (Figure 19) with respect to workpiece every time a new tool is inserted. New work coordinates must be defined every time a tool is replaced. Variation in Z-offset in the range of microns could largely impact the axial depth of cut. To avoid direct touch, an indirect technique was developed for finding Z-offset. The tool was lowered and touched to a thin cantilever beam that completed a circuit. The set up consists of a precision gage block of known thickness. Three thin layers of 3double sided sticky tape was stuck side to each other (Figure 23). A small black dot was marked on a thin copper strip and was carefully placed on the double sided sticky tape such that the black dot faces upwards. At least a quarter of the length of copper strip was let to hang freely. The copper strip now acted as a cantilever beam thus bending freely when the tool touched.

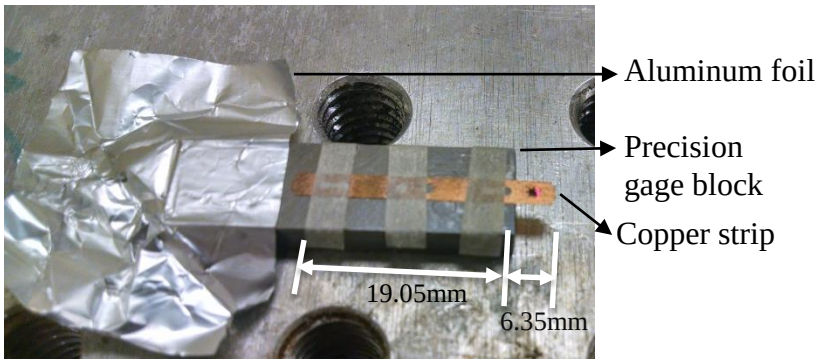

Figure 23. Precision gage block (thickness=3.81mm) with copper strip hanging with support of double side sticky tape.

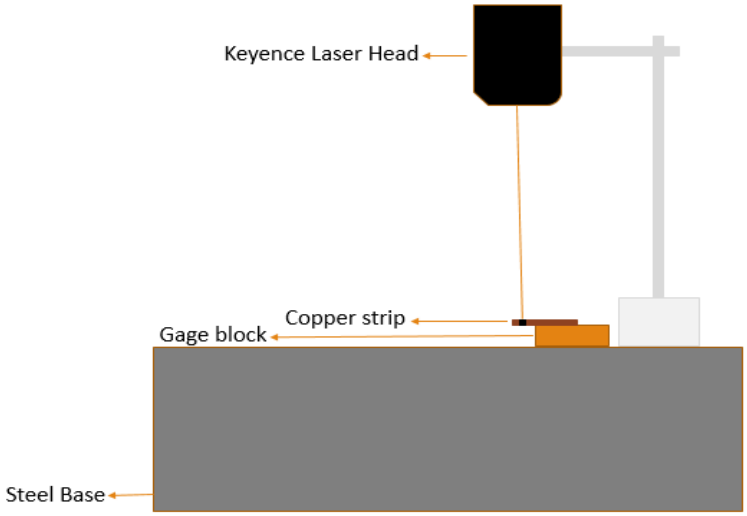

Figure 24. Schematic diagram representing precision gage block and Cu strip thickness measurements with Keyence laser displacement sensor.

Steps for measuring precision gage block and Cu strip thickness and micro tool offset measurements:

1. The height of this black dot (precision gage block and Cu strip thickness) from a steel table was repeatedly measured 20 times by Keyence laser displacement sensor (Figure 24). Average of these 20 value were recorded.

2. A small strip of aluminum was adhered to the other end of gage block. This was to connect one end of the multimeter to the precision gage block and Cu strip.
3. The micro tool was moved close to the point where we want to start machining in the X and Y directions of the milling machine (Figure 19) and the gage block with Cu strip was placed on the workpiece.
4. X and Y offsets were estimated and 'Part Zero Offset' option on the control panel of the CNC machine was selected to record X and Y coordinate locations.
5. One end of the multi meter was connected to the shank of micro tool and other end was connected to the aluminum strip (Figure 25).

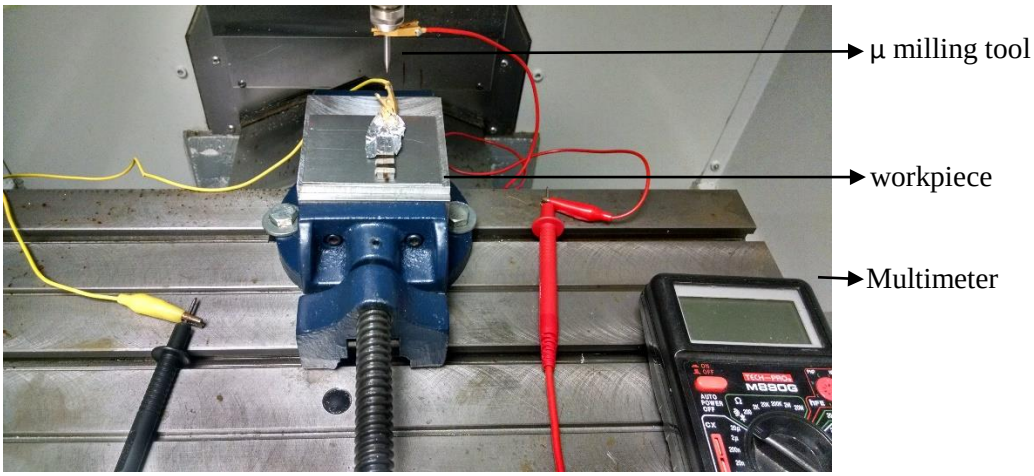

Figure 25. Set up for measuring tool offset.

6. The micro tool was lowered in the Z direction (in increments of 1 μm when close to the gage block) towards the black dot. As soon as the tool touched the copper strip, the circuit was complete and multi meter reading indicated change in

conductivity by making a beep sound. The micro tool was rotated all along the way to ensure better tool workpiece contact

7. As soon as a change in resistivity was observed the 'Part Zero Offset' was selected to record the current position of Z. The average value of gage block thickness with Cu strip, which was measured earlier was compensated from the current Z-offset value.

4.3.3.3 Keyence laser displacement sensor

The Keyence laser displacement sensor was used to capture the tool vibration signal during meso and micro milling experiments. The laser head emits red semiconductor laser with a wavelength of 655 nm (Keyence, 2015) which was reflected of the tool shank and is received by the laser head. The resolution of the instrument is 0.1 μm. The laser head was let to warm up for at least 30 minutes to stabilize the system before taking recording data. LK-Navigator software was used to capture and save the vibration signal. Also, the maximum number of data points that could be captured at one go is 65,000 (Keyence, 2015). Due to constriction of space around the machine, the laser sensor was placed at an angle of 45^{o} from X and Y axis of machine. The laser head of the sensor was held in position with the help of a metal support stand. This support stand was adjusted to ensure that the laser reflected off the tool shank, just above the cutting teeth (Figure 19).

4.3.3.4 UNIST micro mist system set up

The UNIST micro mist system was set up to provide lubrication during milling experiments. It provided minimum quantity lubrication (MQL) during meso and micro milling experiments. The number of pulses was set at 8 per minute. Also the system can

spray the lubricant at any angle and location in the milling machine. Coolube 2210EP was used for MQL. Input air pressure was set at 400 kPa and lubricant consumption rate was 0.022 cm^3/min (1.32 ml/hr). If the micro mist nozzle was set up along the Y-axis of the machine, the chips would interfere with cutting and might be responsible for degraded surface. Hence it was decided to place the micro mist nozzle at approximately 30^0 to the X-direction, 45^0 to the Y-direction and 60^0 to the Z-direction (Figure 19).

4.3.4 Experimental conditions for meso milling

The meso milling experiments were done in two stages. The first stage of experiments involved experiments on aluminum 6061-T6 for verifying the theoretical line roughness equation. The experimental conditions are given in Table 6. The values of chip loads ranged from 0.0005 in (12.7 mm) to 0.004 in (101.6 mm). Medical manufacturing students (ENTC 418, spring 2014 and 2015) were given the choice to pick chip loads from a specified range in accordance with Machinery's Hand-book (29^{th} edition). These experiments were done as part of one of their lab exercises. The second stage of meso milling experiments were conducted on A36 carbon steel to preliminarily identify the significant parameters that effect BUE formation.

Slot milling was performed with each slot at a distance of 5 mm away. A total of two WC and AlTiN-WC flat end mills were used for the experiments. The uncoated tool was used to machine 4 slots and the coated tool was used to machine 4 slots. The length of machined slot was around 8 mm. Cutting speeds and chip loads were selected from the Machinery's Hand-book (29^{th} edition). Cutting speeds of 15 m/min and 80 m/min were chosen to ensure that one speed lies within the BUE range and one speed outside the range

(Childs, 2011). Similarly, depth of cut values were chosen to make sure they were large enough to study its effect on surface roughness. Surface roughness was measured at eight places along the length of slot (center) approximately 1 mm away and average of these values were calculated. Taguchi's half factorial design was selected as it was crucial to initially identify the parameters that significantly affected the surface roughness. Since four attributes were varied at two levels each, Taguchi's half factorial design suggested eight randomized experiments to find individual significant factors (Table 6). Open source statistical software R was used to fit a linear model between all the four response variables. The results are presented in Table 12.

Table 6. Meso milling experimental conditions.

Workpiece material	Tool Coating and diameter (mm)	Depth of cut (µm)	Cutting fluid	Cutting speed (m/min)	Chip Load (µm/tooth)
Al 6061 T6	uncoated HSS, Φ3.175	100	Dry	30/60	12.7
		100	Dry	30/60	20.32
		100	Dry	30/60	25.4
		100	Dry	30/60	30.48
		100	Dry	30/60	38.1
		100	Dry	30/60	50.8
		100	Dry	30/60	63.5
		100	Dry	30/60	76.2
		100	Dry	30/60	88.9
		100	Dry	30/60	101.6
A36 carbon steel	uncoated WC, Φ3.175	50	Dry	15	15
		50	MQL	80	15
		100	Dry	80	15
		100	MQL	15	15
	AlTiN WC, Φ3.175	50	Dry	80	15
		50	MQL	15	15
		100	Dry	15	15
		100	MQL	80	15

4.3.5 Experimental conditions for micro milling

Cutting speed and chip load are two factors that were varied at four levels during the experiments. Taguchi design of experiments suggested a total of 16 randomized experiments. A new uncoated WC tool with 2 cutting flutes was used for each cutting condition. A slot of length 12 mm was machined under MQL. The experimental conditions for micro milling are shown below in Table 7. A low cutting speed of 10m/min was chosen to ensure that a minimum spindle speed was maintained and high cutting speed of 60m/min was selected as it was the maximum achievable RPM on the milling machine.

Table 7. Micro milling experimental conditions.

Material	**Tool coating and diameter (mm)**	**Depth of cut (µm)**	**Cutting fluid**	**Cutting speed (m/min)**	**Chip Load, (µm /tooth)**
316L stainless steel	uncoated WC, Φ0.406	30	MQL	10	0.05
				27	0.05
				44	0.05
				60	0.05
				10	0.2
				27	0.2
				44	0.2
				60	0.2
				10	0.5
				27	0.5
				44	0.5
				60	0.5
				10	1.0
				27	1.0
				44	1.0
				60	1.0
NiTi	AlTiN coated, Φ0.8	30	Dry	10	2
					4
					6
					8

4.3.6 Post experimental measurement procedures

The machined tools and workpiece surfaces were ultrasonically cleaned in 70% isopropyl alcohol and pressurized air to get rid of dirt, chips and lubricant.

4.3.6.1 ZYGO ZeGage 3D optical surface profiler - Surface roughness

Zygo 3D profiler was used to measure the values of average line (R_a) and surface roughness (S_a). Also all the measurements were randomly taken along the center of slot randomly. Average of 15 measurements were recorded for each condition or slot. For taking the measurements, the workpiece is initially placed on the T-slot table of the Zygo profiler. A scanning length of 20 µm was selected for our purposes. Additional post processing functions provided by the ZeMaps software were utilized to enhance the quality of the image. Also, before taking the measurements the optical profiler was calibrated with a standard calibration piece of known line roughness.

4.3.6.2 ZYGO ZeGage 3D optical surface profiler -Tool wear

Zygo 3D profiler was used to measure area loss of cutting tool material. Images of top view of all tools before machining were taken. Similarly, images of tools after machining were also pictured and superimposed on top view of pictures of new tools. The loss in volume for one cutting edge is magnified and calculated using an open source software Image J. Similarly, wear for other side is calculated and average is calculated.

4.3.6.3 OLYMPUS optical microscope - BUE density

OLYMPUS optical microscope and Image Pro v4.5 software were used to calculate BUE density. BUE area density is defined as the absolute number of Built-up-edges per square millimeter area. Similarly, BUE linear density is defined as the absolute

number of BUE per millimeter along the center of slot. BUE density is an attempt to quantify the presence of BUE on the machined surface to qualitatively compare two different machining conditions. The following approach has been taken to quantify the BUE density.

a) An average of 20 image samples were taken for a particular condition with 10 samples on up-milling side and 10 on down-milling side of each slot under the Olympus optical microscope. Images with sampling area of 100 µm X 100 µm were captured.

b) All the images on optical microscope were then taken in 0-255 range gray scale. Different values of gray scale ranging from 50-90 were initially selected to find the best value that most closely counts the number of black dots. A gray scale value of 75 was chosen as it closely matched the actual number of BUE's. Counting tool from Image Pro 4.5 software was used to count the number of BUE images on the machined surface.

4.3.6.4 TESCAN Vega LM3 – Scanning electron microscope

TESCAN Vega LM3 was used to take high resolution and magnification images of workpiece surfaces and tools. All the images were taken at a high vacuum of 9 X 10^{-3} Pa with a resolution of 3 nm at 30 kV accelerating voltage.

4.3.6.5 Statistical software

The R statistical software was used for preliminary data analysis after meso milling of A36 carbon steel. A simple R code was run to fit a linear regression model with surface roughness (S_a) as response variable. The values of estimates from the output table aided

in developing a surface roughness model with machining parameters as input variables. A negative value of estimate implied that the input variable associated with the estimate was negatively correlated with surface roughness. Also p-value was the most important parameter in deciding the important factor affecting surface roughness (S_a). A smaller p-value implies that the factor affects the response more.

5. RESULTS AND DISCUSSION

5.1 TOOL RUNOUT RESULTS

The spindle speed frequency, f_z, at 10,000 RPM is calculated as following:

$$f_z = \frac{N\ rev}{min} * \frac{1\ min}{60\ sec} = \frac{10000}{60} = 166.67 \text{ Hz}$$

Similarly, spindle speed frequency, for other rotational speeds are shown in Table 8.

Table 8. Spindle speed frequencies calculated at various tool rotational speeds.

Tool Revolution (RPM)	**Spindle speed frequency (f_z)**
10,000	166
20,000	333
30,000	500
40,000	666
50,000	833

Time series plots for different rotational speeds are shown in Figures 26 (a), (b), (c), (d) and (e).

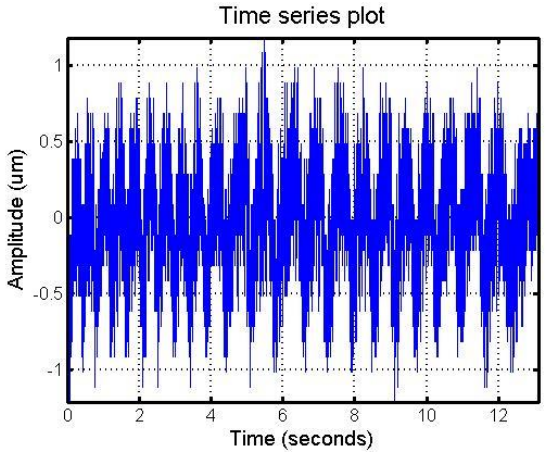

(a)

Figure 26. Time series plot at different tool rotation speeds (a) 10,000 RPM. (b) 20,000 RPM. (c) 30,000 RPM. (d) 40,000 RPM. (e) 50,000 RPM.

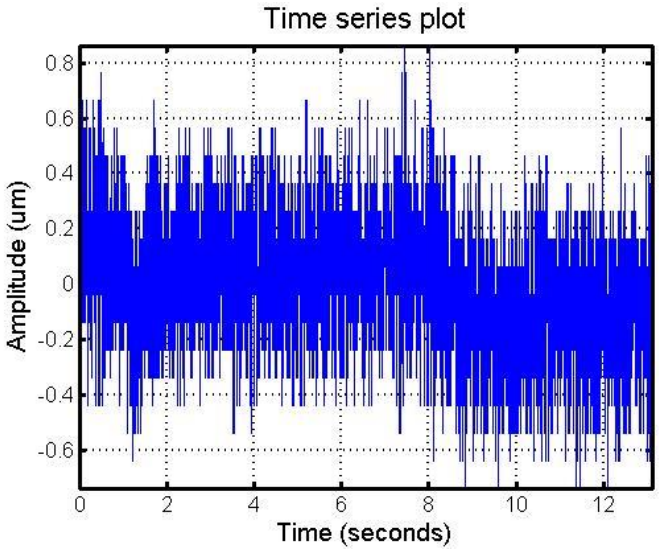

(b)

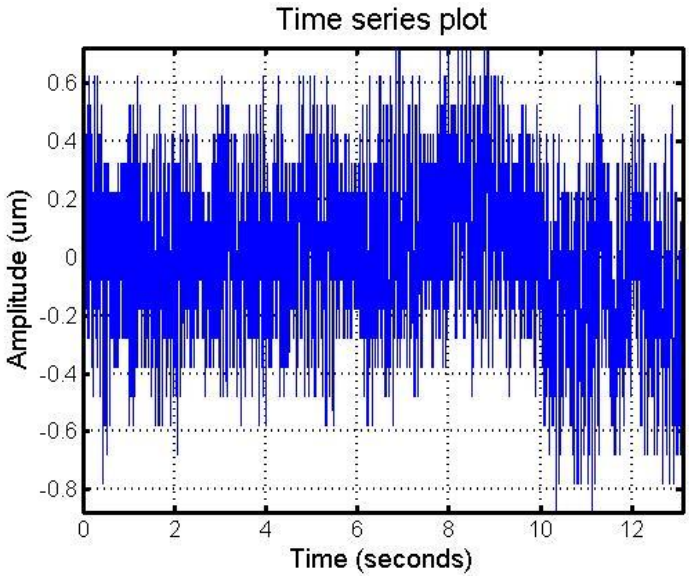

(c)

Figure 26 Continued.

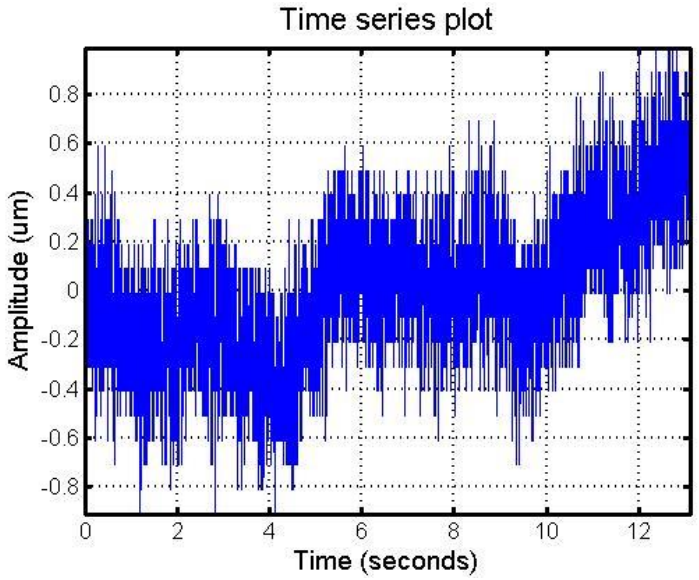

(d)

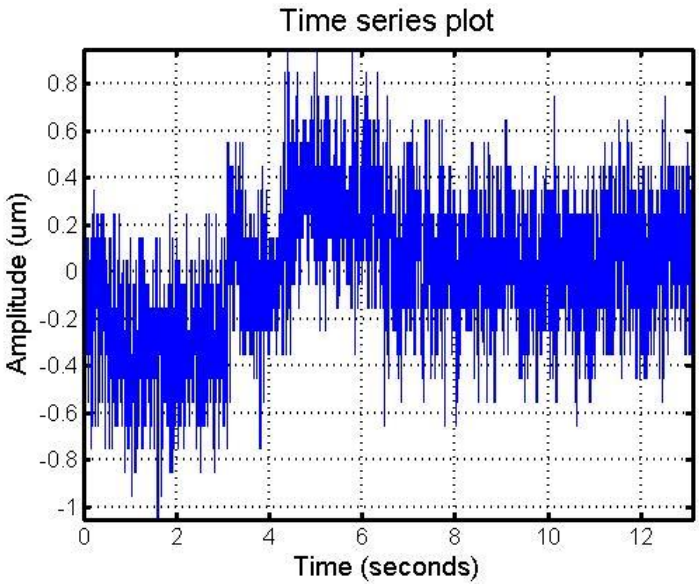

(e)

Figure 26 Continued.

Average and standard deviation of tool runout at different tool rotational speeds in increments of 10,000 RPM are recorded and calculated. The difference between the 3

standard deviations is compensated for electronic drift (HAAS, 2014) of the system and final values of runout are given in Table 9.

Tool runout = (Average + 3σ) – (Average - 3σ) – electronic drift (4)

Tool runout = 6σ – electronic drift ($\pm$ 0.5 µm) (5)

Table 9. Tool runout values measured at different speeds.

Tool Revolution (RPM)	**Tool runout (µm)**	**Average of time series plot (µm)**	**Standard deviation, σ (µm)**
10,000	0.598	-1.182×10^{-12}	0.2663
20,000	0.807	-1.941×10^{-12}	0.3011
30,000	0.561	2.388×10^{-12}	0.2601
40,000	0.435	2.587×10^{-12}	0.2391
50,000	0.435	2.587×10^{-12}	0.2391

The periodic peaks on the FFT plots in Figure 27 represent the spindle frequencies. The rest of the smaller peaks might be due to noise from the harmonic vibrations, laser noise and external disturbances in the surrounding environment. The peaks at low frequency zones were due to noise created by pulsating MQL system.

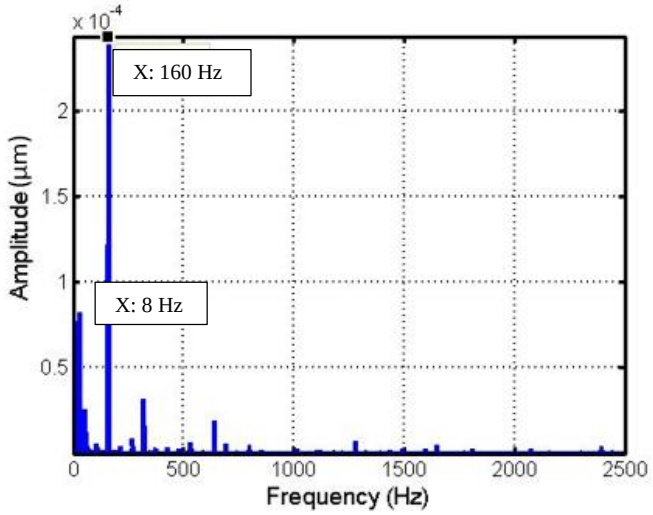

(a)

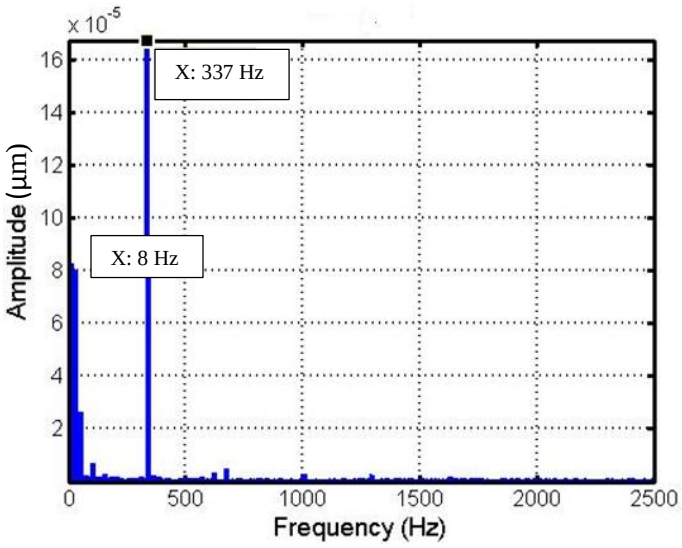

(b)

Figure 27. Frequency domain plot at different tool rotational speeds (a) 10,000 RPM. (b) 20,000 RPM. (c) 30,000 RPM. (d) 40,000 RPM. (e) 50,000 RPM.

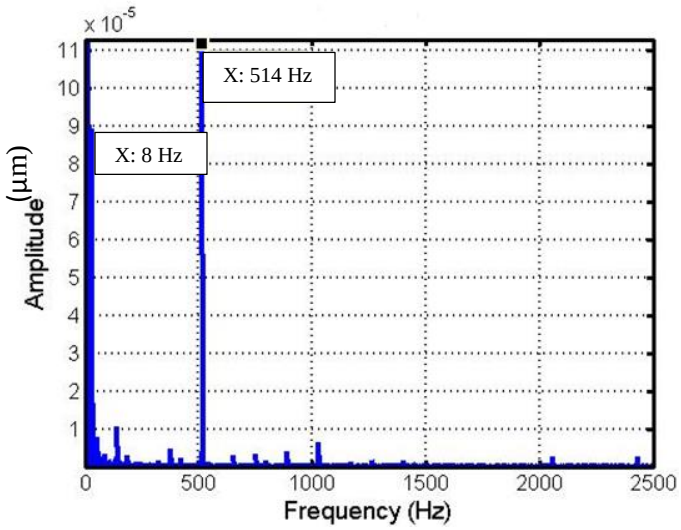

(c)

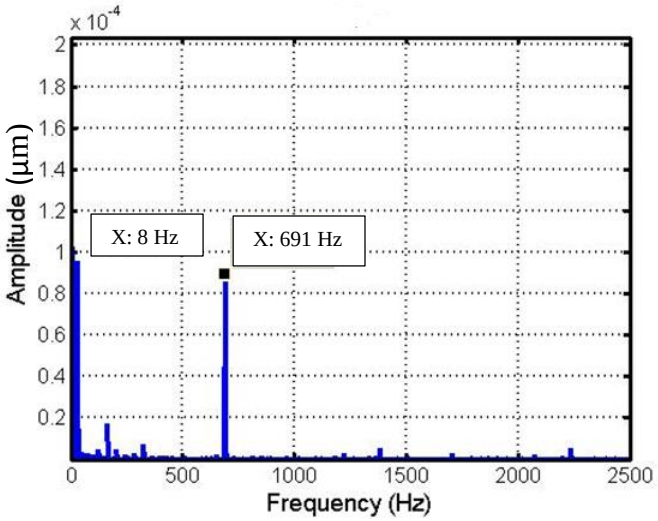

(d)

Figure 27 Continued.

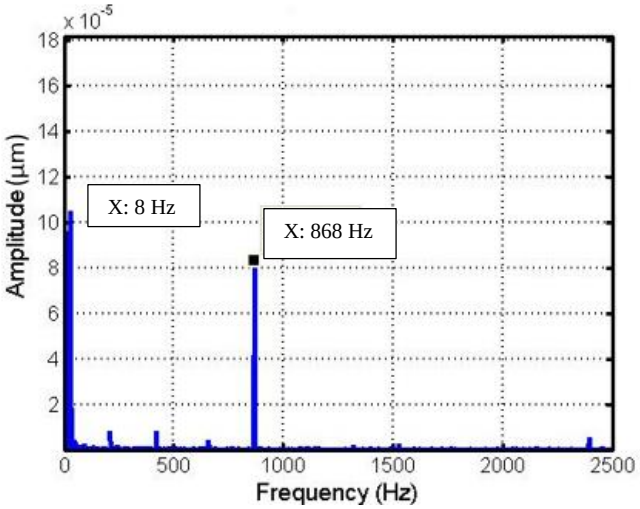

(e)

Figure 27 Continued.

A Φ3.175mm plug gage was used for runout measurements. It was observed that the runout decreases as the tool rotational speed was increased as the machine achieves stability at high tool rotational speeds (Table 9). Also the measured frequency was a little different from the theoretical frequency (f_z), due to electronic drift in the system.

5.2 TOOL OFFSET

To check the accuracy, consistency and repeatability of tool offset technique before machining, series of tool offset measurements were conducted and the results are presented in Figure 28.

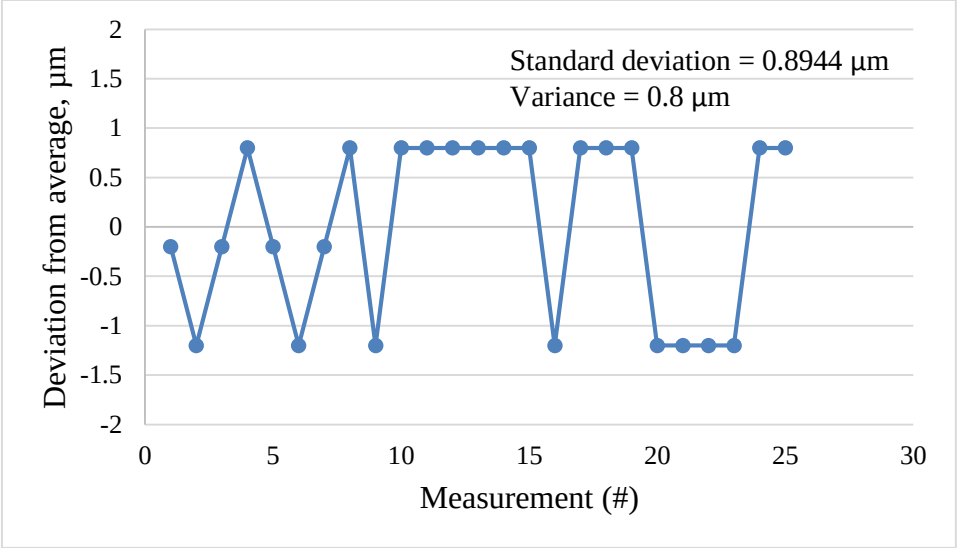

Figure 28. Repeatability and consistency of tool offset values.

From Figure 28, it is clear that the standard deviation of this technique is 0.8 µm. However, the range of this technique is 2.5 µm which is less than the repeatability of 3 µm as specified by machine manufacturer.

5.3 DETECTION OF BUILT-UP-EDGE

BUE formation is critical factor that directly affects surface finish. There are many factors responsible for the formation of BUE. A lot depends on machining parameters like cutting speed, depth of cut, type of lubrication, chip load, workpiece and tool material combination, tool condition etc. Varying one or combination of the above said factors would generate different workpiece surfaces. Also BUE formation is intermittent and highly unpredictable. Formation of BUE is observed with almost all machining parameter combinations. The intensity or density of BUE's however are different for different cutting conditions. To quantify the presence of BUE, it is necessary to successfully identify BUE.

BUE can generally be detected at 3 different places after machining:

- Rake and clearance surfaces of a cutter after machining
- Chips collected during machining
- Workpiece surface after machining

The most commonly followed technique to identify BUE is by observing the rake surface of the tool as seen in Figure 29. During machining the temperatures around chip-workpiece interaction zone reach favorable temperatures suitable for formation of BUE (Iwata and Ueda, 1980).

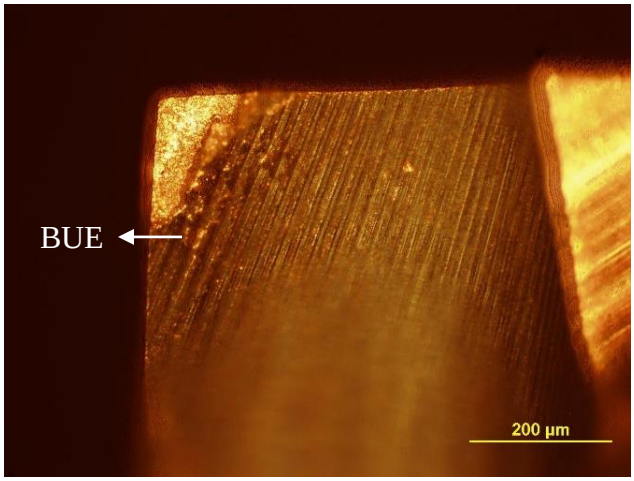

Figure 29. Tool rake surface of uncoated WC after machining 4 slots, length 32 mm, Uncoated Φ0.406 mm WC flat end mill, 15-80 m/min speed, 15 µm/tooth chip load, 100 µm depth, dry and MQL, A36 carbon steel workpiece.

Another technique is to observe chips for BUE. During machining when chips flow along the rake surface of milling cutter, BUE on the rake surface might break and weld to the chip surface as observed in Figure 30. The chips generated after machining are usually

curled. Also since only one side of the chip interacts with the tool rake surface, evidence for BUE must be searched carefully on only one side. Hence there is a very slim probability that only a few chips might actually be suitable for viewing.

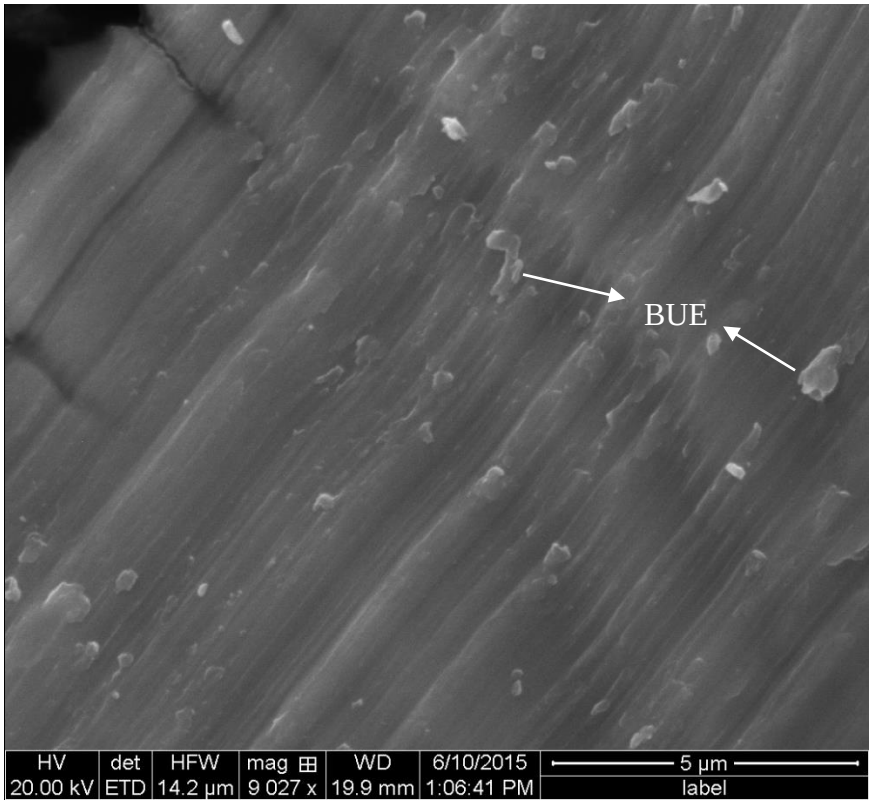

Figure 30. Scanning electron microscopy image of chips collected after machining pure titanium, Uncoated WC tool, Φ0.406 mm, 2 flute, 10 m/min speed, 0.2 µm/tooth chip load, 10 µm depth, dry.

The third place where BUE can be found is the workpiece surface after machining as seen in Figure 31. The BUE that is welded on to the rake surface shields the actual cutting edge and acts as a cutting edge. Due to cutting forces involved and growing BUE size, BUE breaks from the tool and sticks to the surface of workpiece, resulting in poor surface finish.

In this study, BUE found on machined surface was observed and quantified, while showing evidence of BUE on tools.

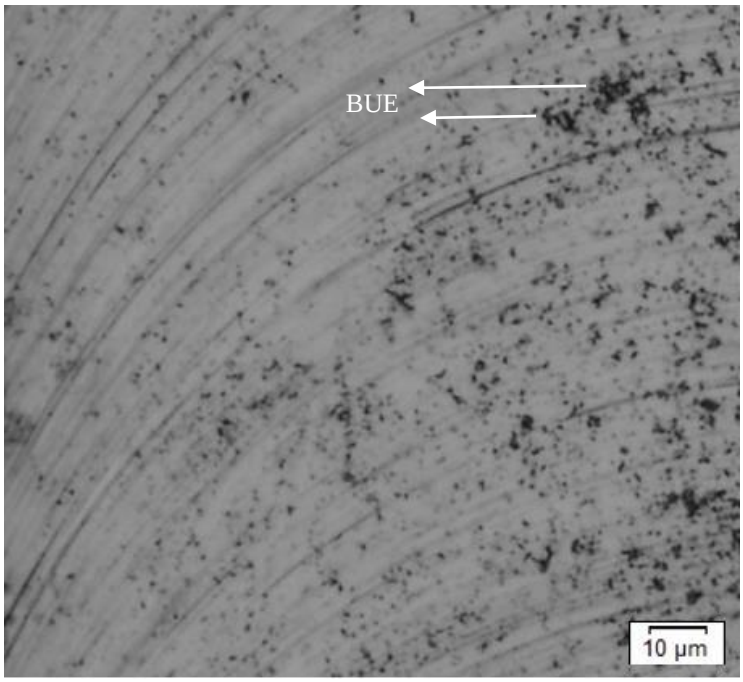

Figure 31. Machined surface of 316L stainless steel with uncoated WC tool, Φ0.406 mm, 2 flute, 10 m/min speed, 0.05 µm/tooth chip load, 30 µm depth, MQL.

5.4 SURFACE ROUGHNESS AND BUILT-UP-EDGE

Zygo surface profiler was used to measure average surface roughness (S_a) and average line roughness (R_a) of the machined slots on the workpiece to find the correlation between average surface roughness, linear and area densities of BUE. From Figure 32, 33 and Figure 34, it is quite obvious that as linear and area BUE density increases the corresponding average line roughness values increase. The correlation between all the three variables was calculated in Excel to find the degree of linear dependence between

variables (Table 10). Since the values of correlation lie from 0 to 1, we can conclude that BUE densities, line and surface roughness are positively correlated and BUE density is one of the reasons for a higher surface roughness.

Table 10. Correlation between Linear density of BUE, Area density of BUE and Line roughness, R_a, A36 carbon steel, 5 m/min speed, high speed steel tool, Φ3.175 mm, 12 mm length, 3 µm/tooth chip load, 50 µm depth, dry.

Variables	**Correlation**
Linear density versus Line roughness	0.795
Area density versus Line roughness	0.875
Linear density versus Area density	0.938

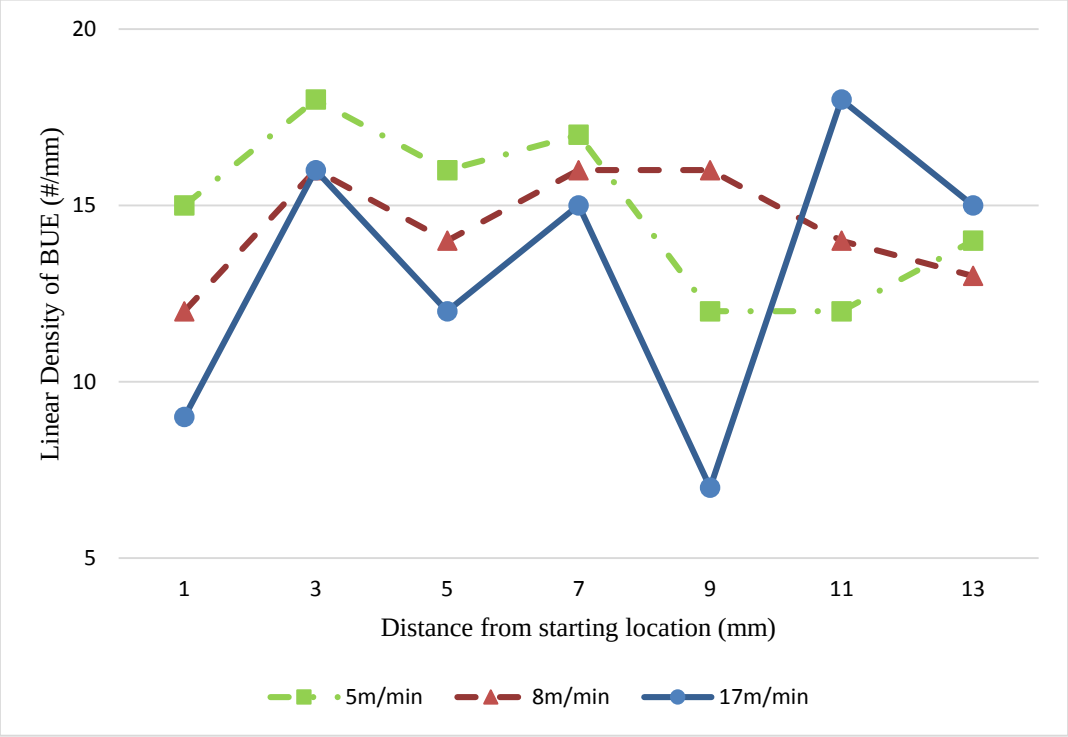

Figure 32. Linear density of BUE at center of slot, A36 carbon steel, high speed steel tool, Φ3.175 mm, 12 mm length, 3 µm/tooth chip load, 50 µm depth, dry.

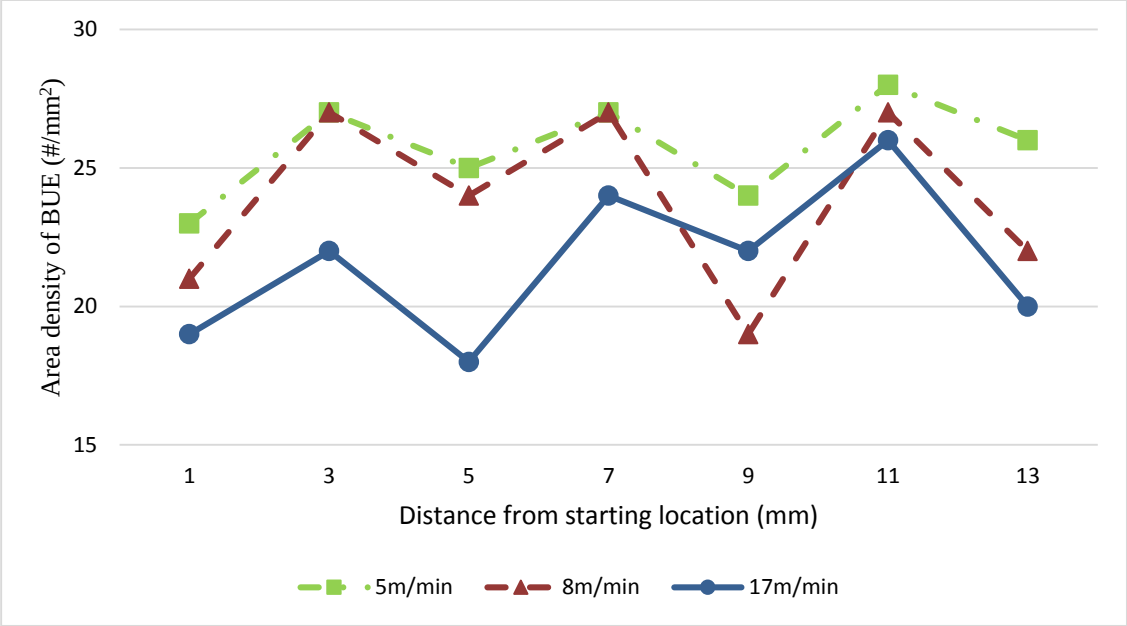

Figure 33. Area density of BUE at center of slot, A36 carbon steel, high speed steel tool, Φ3.175 mm, measurement area-15625 µm^2, 3 µm/tooth chip load, 50 µm depth, dry.

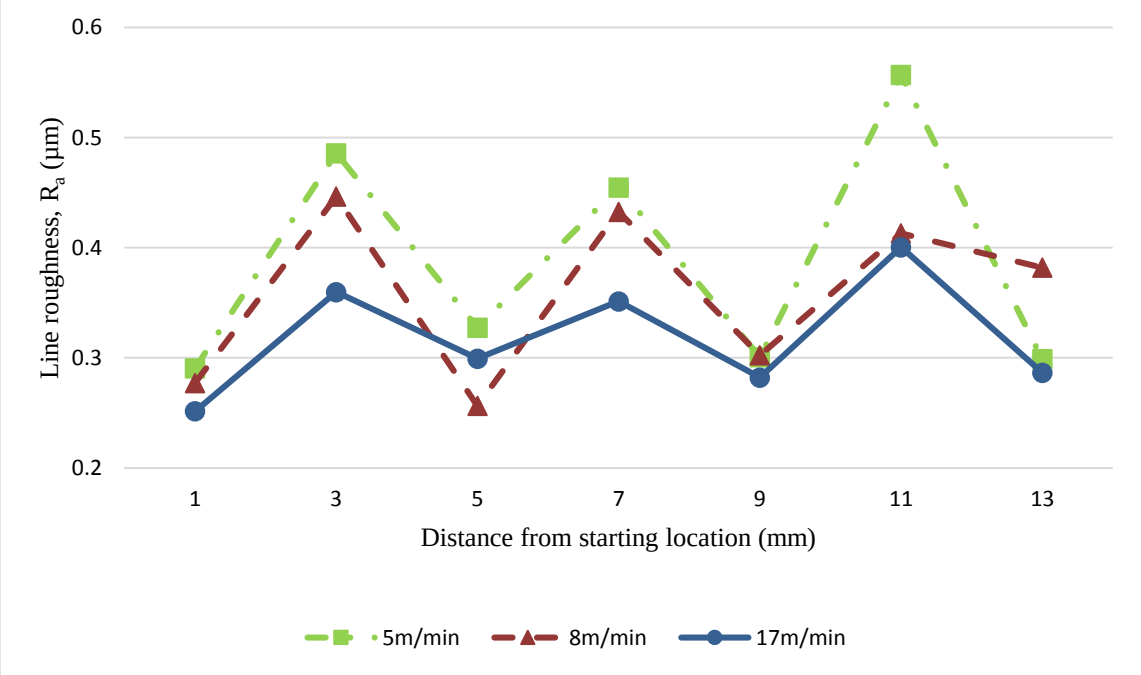

Figure 34. Average line roughness at center of slot, A36 carbon steel, high speed steel tool, Φ3.175 mm, 3 µm/tooth chip load, 50 µm depth, dry.

5.5 THEORETICAL MODEL

A theoretical model was developed based on following assumptions to predict line roughness.

Assumptions:

1. Tool edge radius is negligible compared to depth of cut
2. Chip load and depth of cut are much larger than tool edge radius to avoid ploughing
3. Tool surface and chip has negligible friction
4. Machined surface is free from built-up-edge

The derivation is provided in appendix B. The model is shown in equation (6).

$$R_a = 0.277 \, tan\alpha \, f \tag{6}$$

R_a = line surface roughness (μm)

f = chip load (μm/tooth)

α = concavity angle of flat end mill (^{o})

This equation is used to predict line roughness for meso and macro milled surfaces. Equation 6 proposes that line roughness is directly affected by chip load and concavity angle which is in strong agreement with previous research on surface finish modeling with a deviation of 5.4% from equation (2) (Wang and Chang, 2004). Hence to validate this equation, surface finish data of milled aluminum 6061-T6 are plotted in Figure 35.

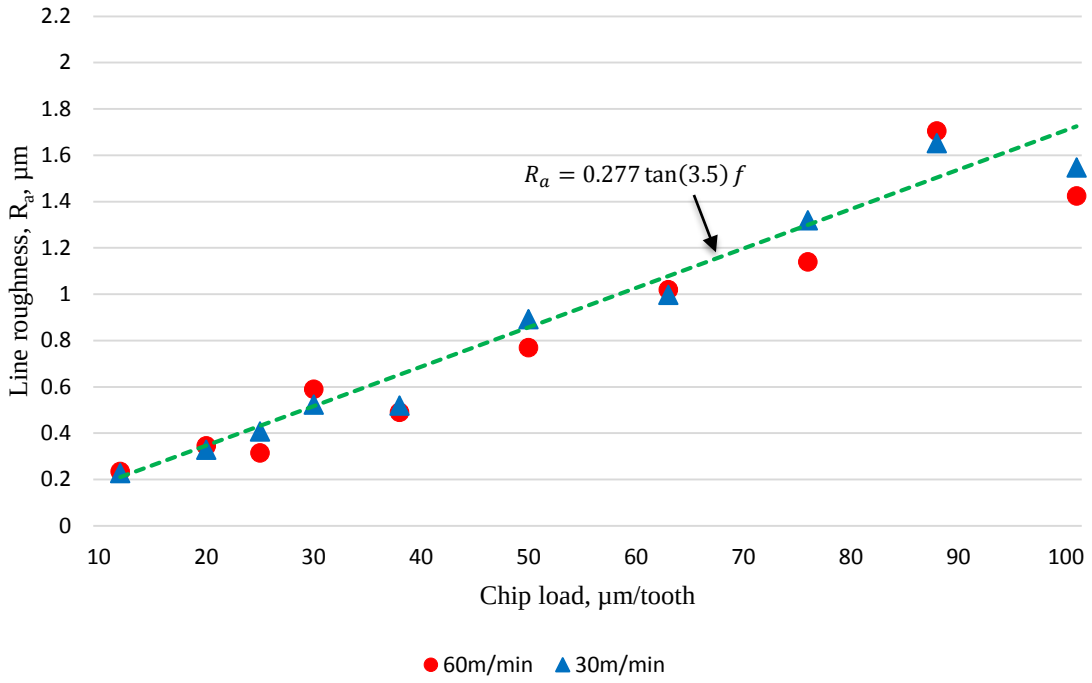

Figure 35. Predicted and actual line roughness R_a values of slots measured at center. Al 6061-T6, high speed steel tool, Φ3.175 mm, 2 flute, 100 µm depth, dry, 3.5° concavity angle.

5.6 RESULTS OF MESO MILLING EXPERIMENTS

5.6.1 Surface Roughness

A series of controlled meso milling experiments were conducted on A36 carbon steel. The experimental conditions are described in Table 6. Surface roughness was used as a response variable to find the factors that affects the formation of BUE due to their correlation. A linear regression model was fit using surface roughness as response variable and cutting speed, depth of cut, tool coating and cutting fluid as input variables (Table 11). In the second stage of iterations, interaction been input variables were also considered. A small p-value (less than a significant value, assumed to be 0.1), is required for that

respective input variable to influence surface roughness. A series of iterations were done and less influential variables were eliminated in successive models. It was found that cutting speed, depth of cut, cutting fluid and interaction between cutting fluid and depth of cut effected BUE formation, with cutting speed clearly the dominant factor due its smallest p-value (Table 11). Also cutting speed and surface roughness are negatively correlated (negative value of estimate), which means that increasing the cutting speed decreases the surface finish resulting in smooth surfaces. The next significant factor was the depth of cut. As the depth of cut increases, amount of rake surface interacting with chip flow increases, thus providing a larger surface area for workpiece material to stick to the rake surface of tool increasing the tendency to form BUE. Also using MQL and AlTiN coated flat end mills improve surface finish due to positive value of estimates.

Equation (7) predicts the surface roughness values based on the estimates for input variables (Table 11). To predict surface roughness, input variables can be plugged into equation (7) with a value of '1' for MQL cutting and '0' for dry cutting.

Surface roughness = (0.415) + (0.013*Depth of cut μm) + (0.733*Cutting fluid) - (0.008*Cutting speed) - (0.013*Depth of cut: Cutting fluid) (7)

The estimate from Table 11 gives the coefficient of each variable in the prediction equation and with an accuracy level given by standard error. Also the measured values of surface roughness varied from 0.332 μm-1.539 μm with the low values occurring at high cutting speeds (80 m/min) and high values occurring at low cutting speeds (15 m/min) respectively (Figure 36). The raw data are in appendix D.

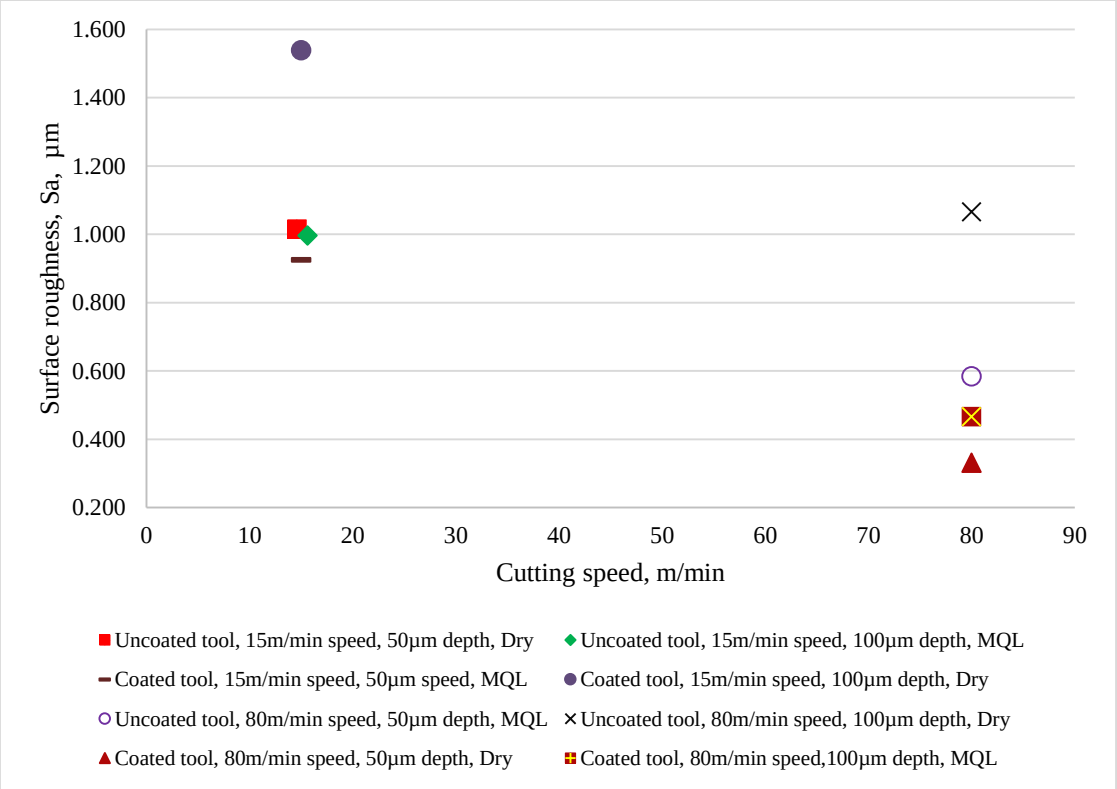

Figure 36. Average surface roughness, S_a, A36 carbon steel, uncoated and coated WC tool, Φ3.175mm, 4 flutes, 15 µm/tooth chip load.

Table 11. Preliminary linear model fit using R statistical software.

Variable	**Estimate**	**Std. Error**	**p value**
Intercept	0.954000	0.362163	0.0780
Tool coating	-0.100000	0.192650	0.6396
Depth of cut	0.015150	0.009632	0.2138
Cutting fluid	-0.245000	0.192650	0.2931
Cutting speed	-0.007800	0.002964	0.0782

Table 12. Final linear model fit using R statistical software

Variable	Estimate	Std. Error	p value
Intercept	0.415000	0.166709	0.08853
Depth of cut	-0.012580	0.002004	0.00817
Cutting fluid	0.733000	0.224098	0.04675
Cutting speed	-0.007800	0.001090	0.00562
Depth of cut : Cutting fluid	-0.013040	0.002835	0.01931

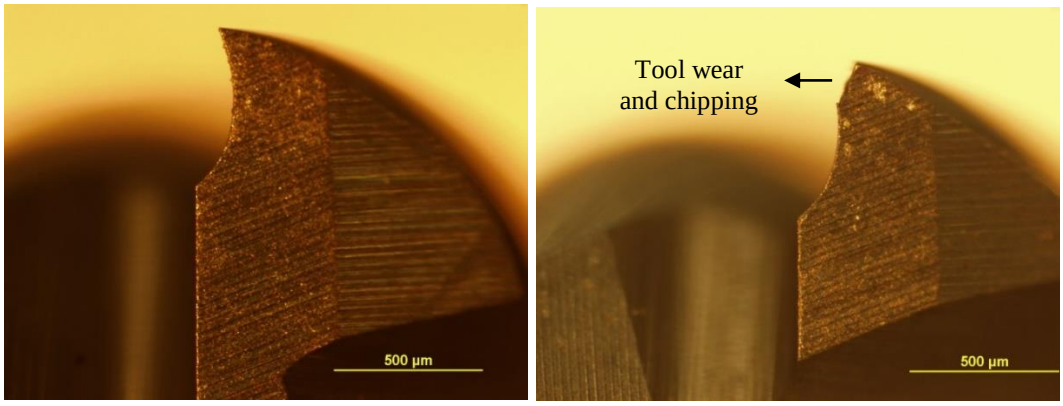

(a) (b)

Figure 37. (a) Uncoated WC tool before machining (b**)** Tool chipping and wear observed on uncoated WC tool. Machining 4 consecutive slots, 32 mm length, 15 m/min and 80 m/min speed, 15 µm/tooth chip load, dry and MQL, 50 µm and 100 µm depth, A36 carbon steel.

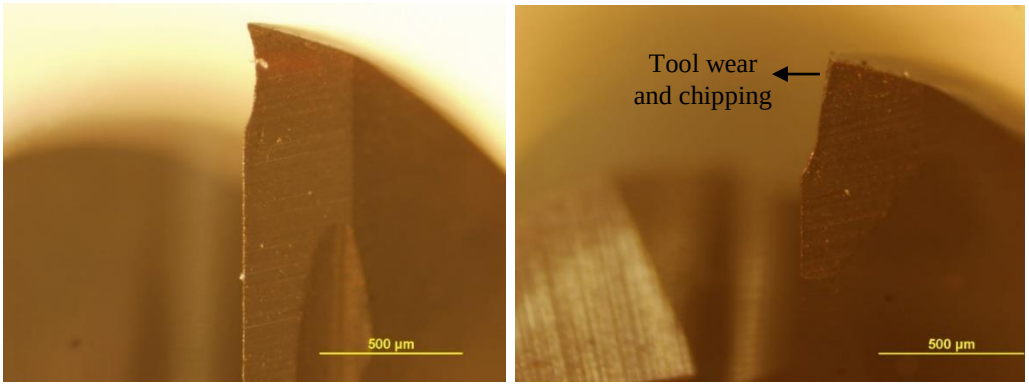

(a) (b)

Figure 38. (a) TiAlN coated WC tool before machining (b) Tool chipping and wear observed on TiAlN coated WC tool. Machining 4 consecutive slots, 32 mm length, 15 m/min and 80 m/min speed, 15 µm/tooth chip load, dry and MQL, 50 µm and 100 µm depth, A36 carbon steel.

Figure 37(a) and (b) show microscopic images of uncoated WC tool before and after machining 4 consecutive slots respectively for a total length of 32 mm (Table 6). All the four cutting edges were observed for evidence of wear and it was found that one of the cutting edges on both the tools had been chipped. Similar results were observed for AlTiN coated tool as shown in Figure 38(a) and (b). Also, it was found that wear and chipping was more for uncoated WC flat end mills over coated WC cutters. The four rake surfaces were also observed for evidence of BUE after machining 4 slots for a length of 32 mm. Presence of BUE on the rake surfaces is clearly evident from Figure 39. Workpiece surfaces were also observed along with the tool rake surfaces.

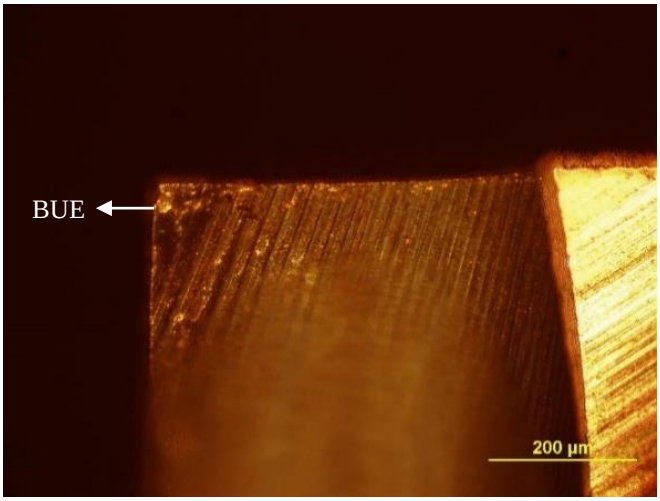

Figure 39. Built-up-edge formation observed on rake surfaces of uncoated WC tool. Machining 4 consecutive slots, 32 mm length, 15 m/min and 80 m/min speed, 15 µm/tooth chip load, dry and MQL, 50 µm and 100 µm depth, A36 carbon steel.

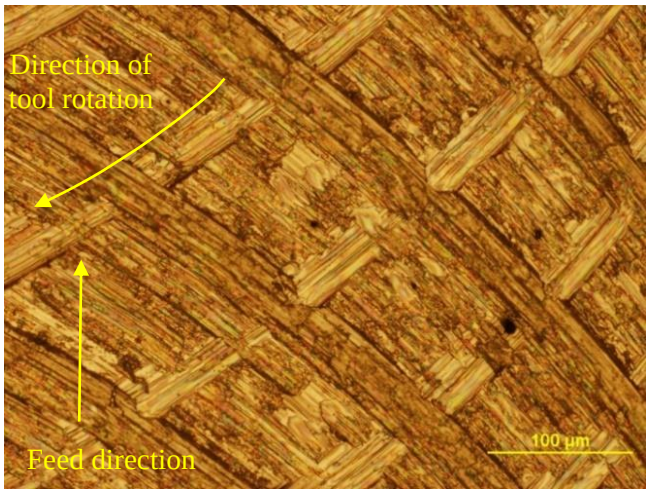

Figure 40. Machined surface of A36 carbon steel. Uncoated WC tool, Φ3.175 mm, 4 flutes, 15 m/min speed, 15 µm/tooth chip load, 100 µm depth, MQL, S_a=0.997µm.

Figure 40 shows machined surface of A36 steel at the cutting speed of 15 m/min and chip load of 15 µm/tooth. As seen from the image it is clear that this surface finish is high when compared to machined surface at 80 m/min cutting speed due to smearing of

BUE on the machine surface (Figure 41). This is evident by visually comparing the chip load marks on Figure 40 and 41. Lower values of surface roughness (S_a), at high speed is due to high quality of finished surface without BUE presence. Also, as seen from Figure 36, surface roughness of machined surfaces at 10 m/min were relatively higher compared to surface roughness of surfaces at 80 m/min irrespective of other machining variables.

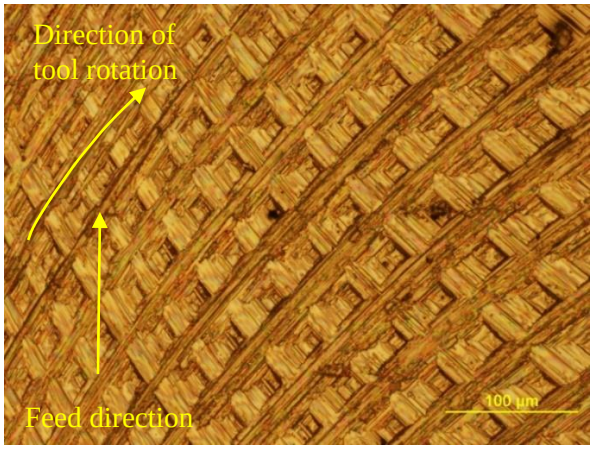

Figure 41. Machined surface of A36 carbon steel. Uncoated WC tool, Φ3.175 mm, 4 flute, 80 m/min speed, 15 µm/tooth chip load, 50 µm depth, MQL, S_a=0.584µm.

5.7 RESULTS OF MICRO MILLING EXPERIMENTS

5.7.1 BUE Density

Area BUE density is used to quantify BUE on the machined surface to qualitatively compare different machining conditions in micro milling experiments. The detailed procedure to count and quantify BUE is described in section 4.3.6.3. Formation of BUE is inevitable and found with all combinations of cutting speeds and chip loads. Figure 42 shows BUE welded on machined surface after breaking off from tool.

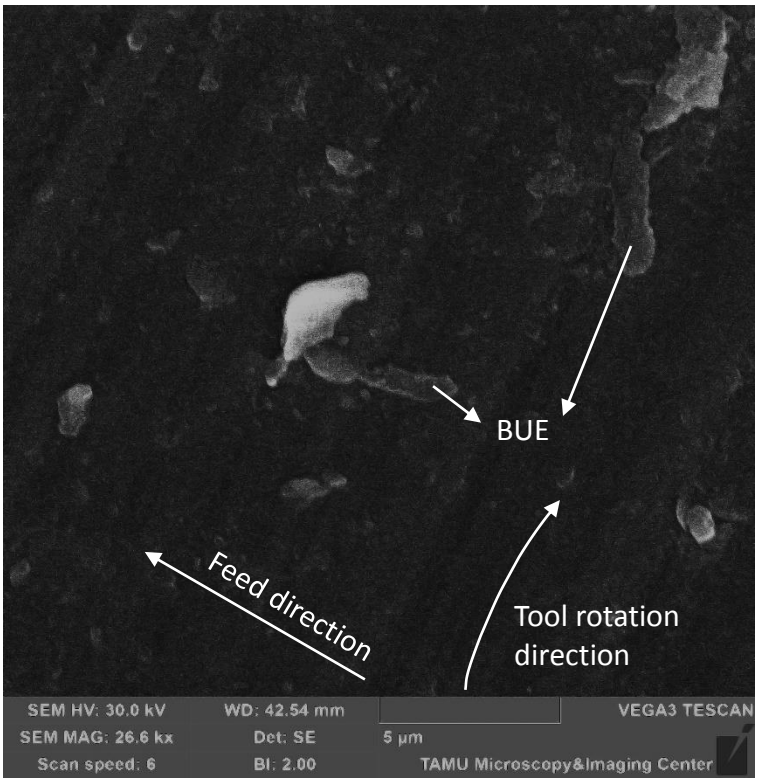

Figure 42. Scanning electron microscopy image of machined 316L stainless steel. Uncoated WC micro mill, Φ0.406 mm, 10 m/min speed, 0.05 µm/tooth chip load, 30 µm depth, MQL.

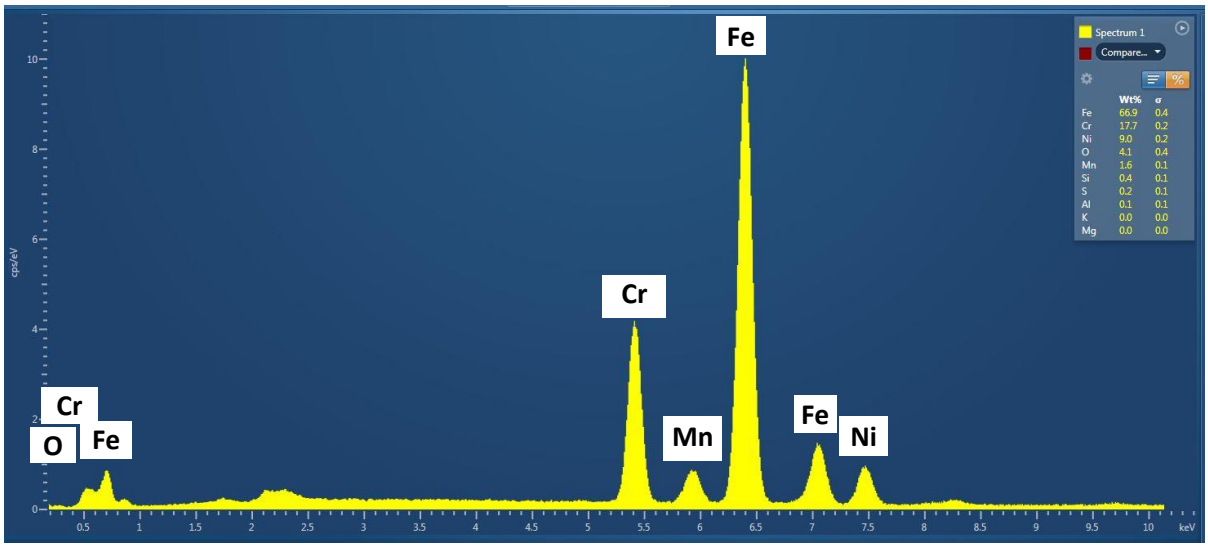

Figure 43. Energy dispersive X-ray spectroscopy (EDS) of BUE.

Table 13. Comparison between material composition of 316L stainless steel and BUE (Azom, 2014) (Steel Grades, 2014).

Material	**316L stainless steel (%weight)**	**BUE (%weight)**
Cr	16-18	17.7
Ni	10-14	9
O	0	4
Mn	<2	1.6
Si	<0.75	0.4
Fe	Balance	69

Energy dispersive X-ray spectroscopy (EDS) of BUE were done on the SEM (Figure 43). By comparing the material composition of BUE with that of 316L stainless steel, we confirm the BUE is from 316L stainless steel (Table 13). Due to the use of MQL during machining experiments and high temperature in the shear zone, BUE oxidizes (presence of oxygen in Table 13) and appear as black dots on optical microscopic images.

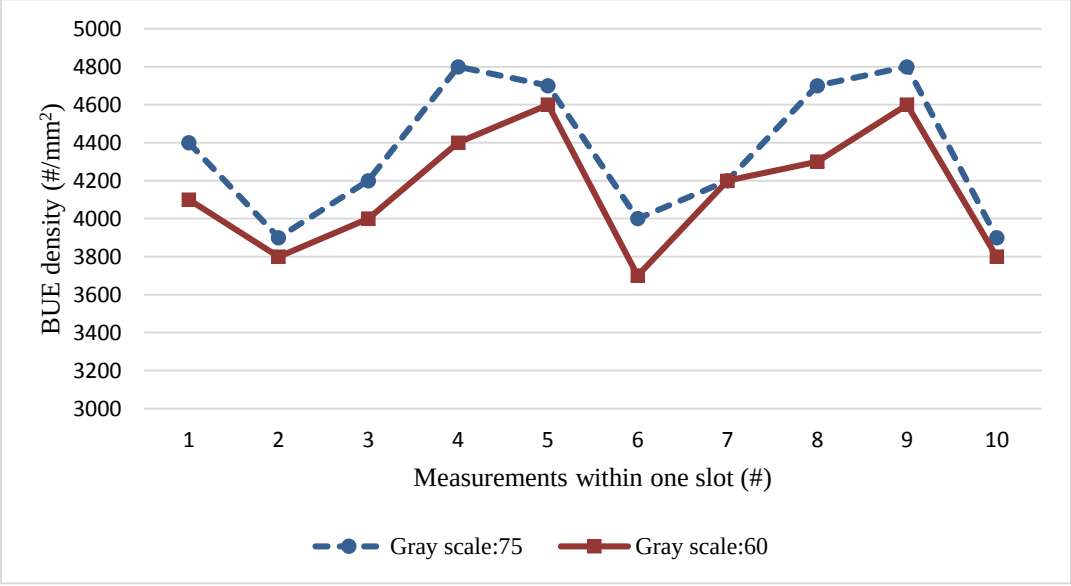

Figure 44. BUE density showing variation for different grayscale. 27 m/min speed, 1 µm/tooth chip load, uncoated WC tool, Φ0.406 mm WC tool, 30 µm depth, MQL.

Since the Image Pro v4.5 software counting tool was relied for BUE density, changing the value of gray scale might result in a different count. A gray scale value of 75 was chosen as it more closely represented the actual number of BUE. Also changing the gray scale value varied the BUE density relatively (Figure 44). Black spots on the images that were falsely counted as BUEs were manually ignored (Figure 45).

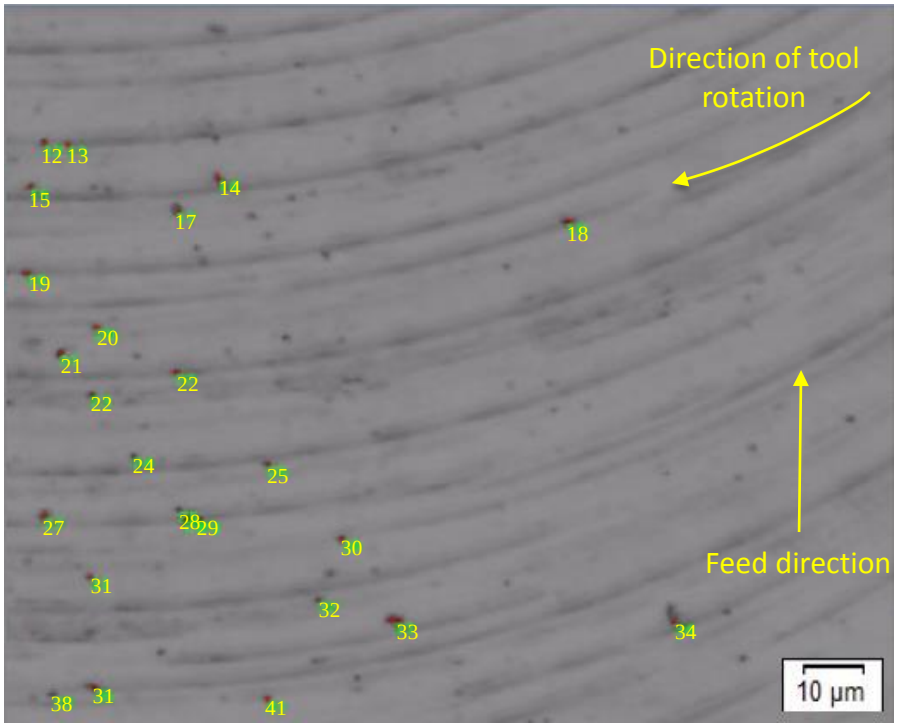

Figure 45. Grayscale image with BUE count on Image Pro software. 316L stainless steel, 44 m/min speed, 0.5 µm/tooth chip load, uncoated WC tool, Φ0.406 mm, 30 µm depth, MQL.

It was also observed that down milling side of the slot has a higher BUE density compared to the up milling side. It was postulated that the direction of MQL nozzle was conveniently placed to remove chips and provide better lubrication on the up milling side

over down milling side. This led to increased friction and temperature between chips and workpiece in the down milling side resulting in higher BUE density (Figures 46-48). Also during up milling width of chip starts from minimum and increases to a maximum at the center of slot and might stick to the tool rake surface. As cutting continues to the down milling side, this further builds up to the tool rake surface resulting in BUE fracture and subsequent sticking on to the machined surface.

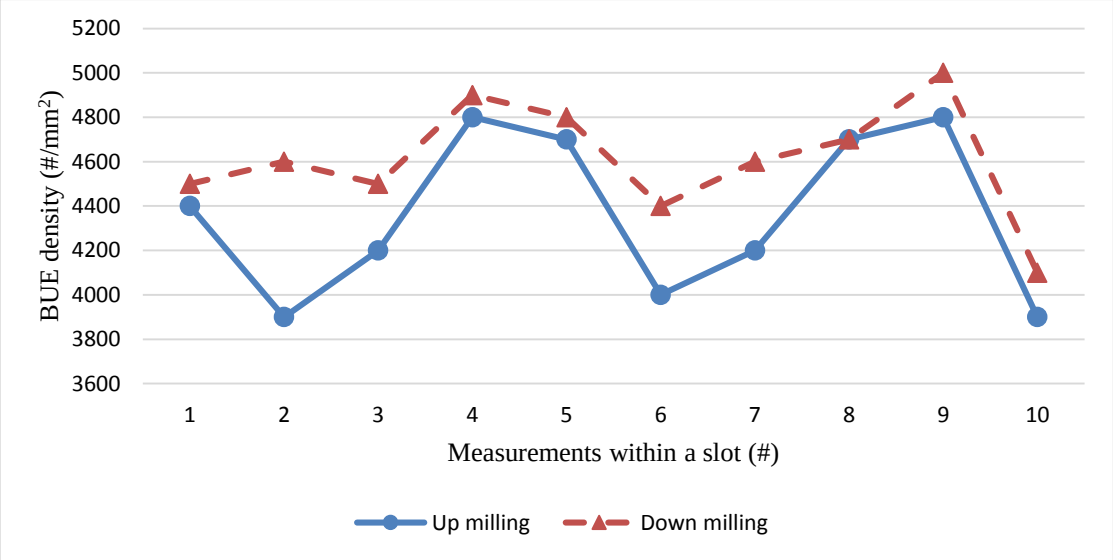

Figure 46. BUE density variation in up and down milling within a sample. 316L stainless steel, 27 m/min speed, 1 µm/tooth chip load, uncoated WC tool, Φ0.406 mm, 30 µm depth, MQL.

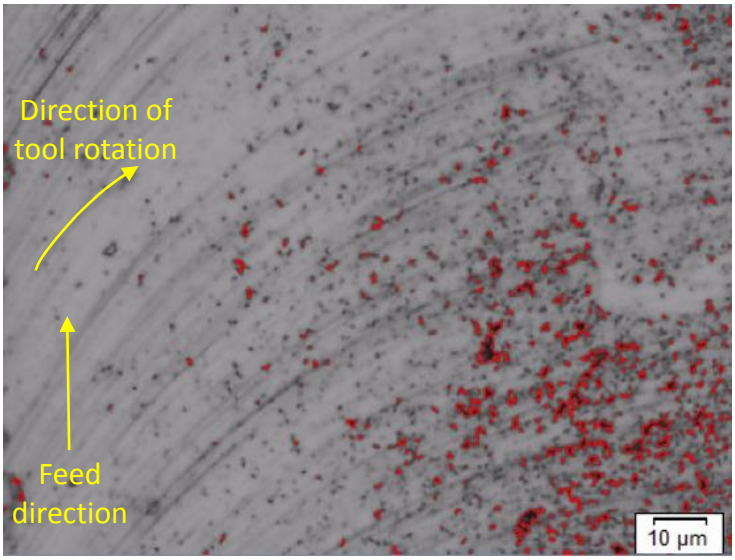

Figure 47. Grayscale image with BUE count on Image Pro software. 316L stainless steel, 10 m/min speed, 0.05 µm/tooth chip load, uncoated WC tool, Φ0.406 mm, 30 µm depth, MQL, up-milling.

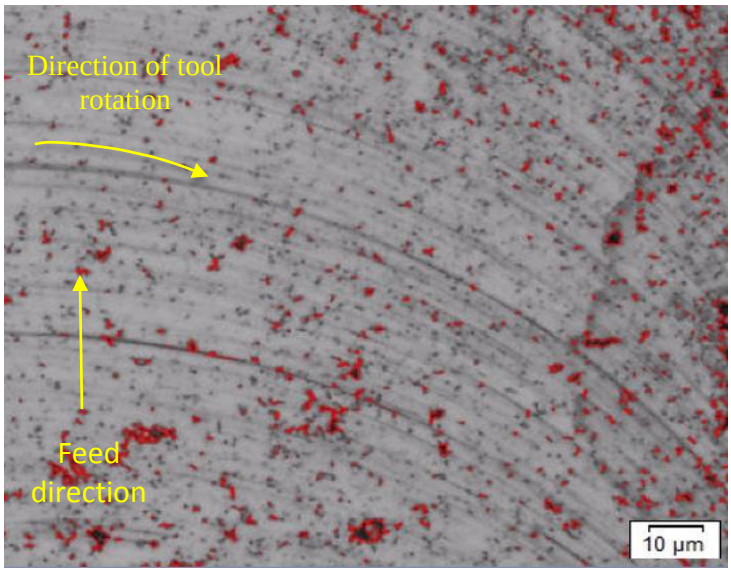

Figure 48. Grayscale image with BUE count on Image Pro software. 316L stainless steel, 10 m/min speed, 0.05 µm/tooth chip load, uncoated WC tool, Φ0.406 mm, 30 µm depth, MQL, down-milling.

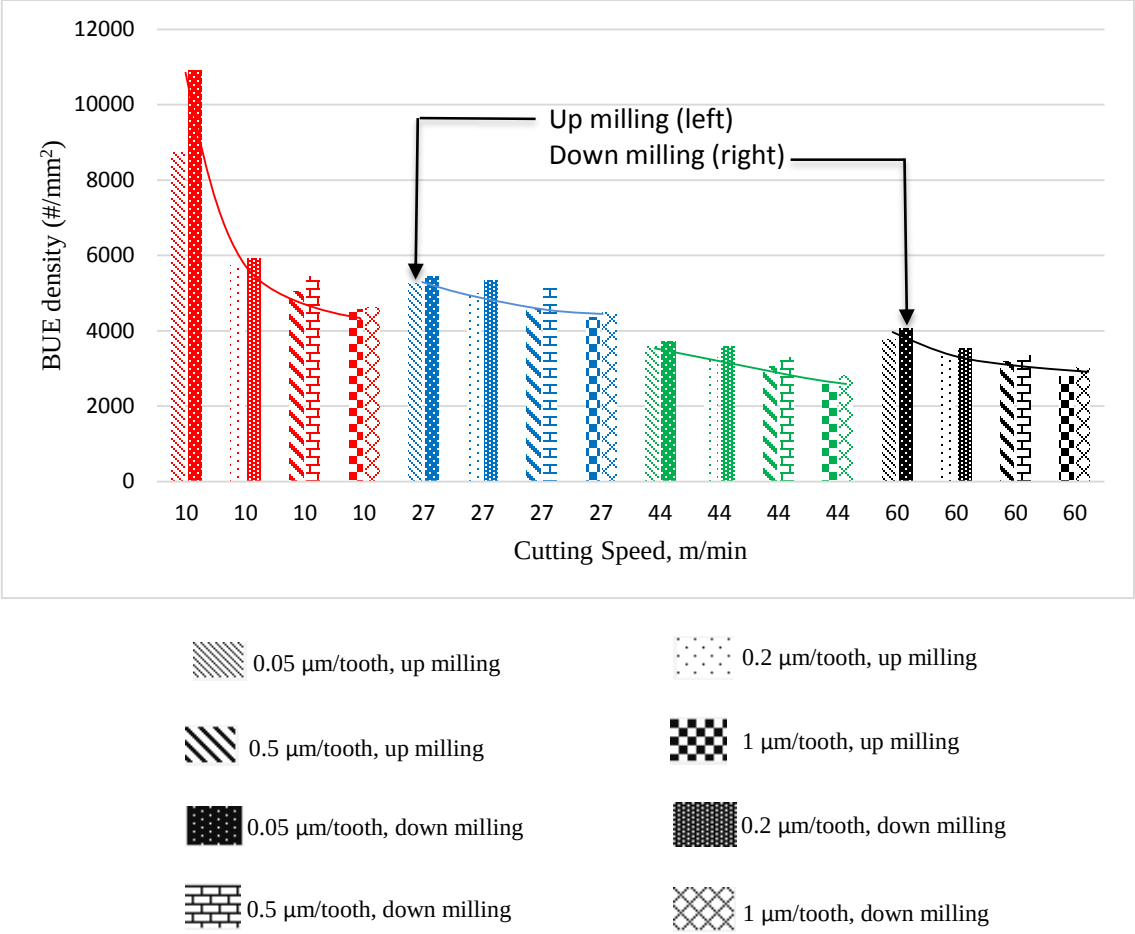

Figure 49. BUE Density (average of 20 samples per slot) on micro milled slots. 316L stainless steel, 10-60 m/min speed, 0.05-1 µm/tooth chip load, 30 µm depth, Φ0.406 mm uncoated WC flat end mill, 2 flutes, MQL.

The results of BUE density for each of the machining conditions are presented in Figure 49. It was observed that BUE density decreases with increasing cutting speeds and increasing chip loads. Since the minimum cut thickness for most of tool-workpiece material combinations lie from 20%-30% of their cutting edge radius (r_e) (0.44-0.66 µm in this case, since r_e=2.21 µm) (Yuan et al., 1996), cutting below chip load of 0.5 µm resulted in ploughing. This led to high BUE density and surface roughness at low chip loads. Also for the same cutting condition, up milling has lower BUE density over down

milling as discussed before. A combination of low cutting speed and low chip load resulted in surface with high BUE density and vice versa.

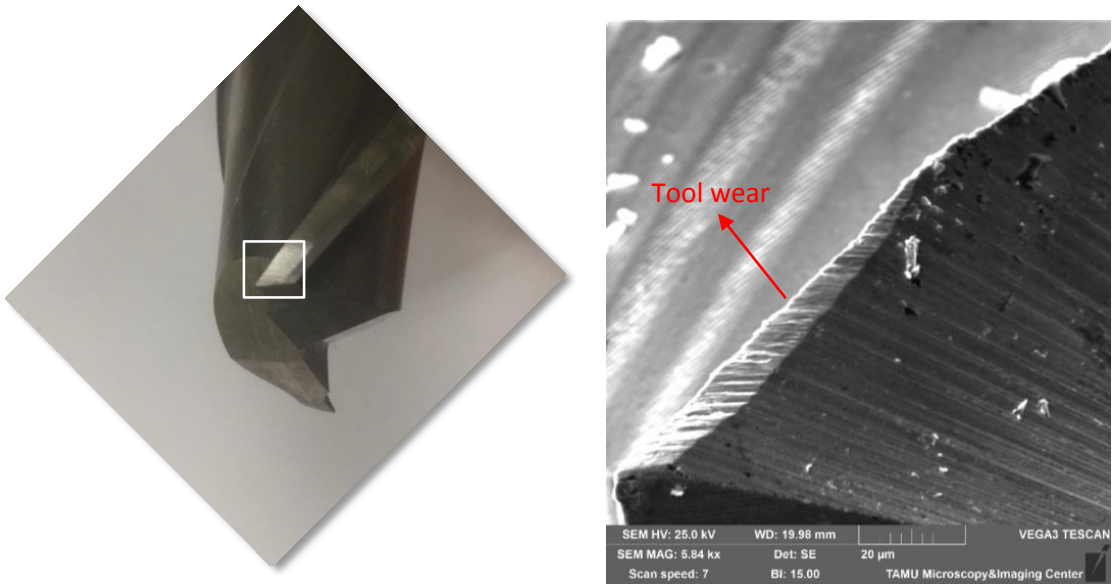

(a) (b)

Figure 50. (a) Flat end mill showing view area of micro end mill tool. (b) Scanning electron microscopy image of cutting edge of uncoated WC tool, Φ0.406 mm, 10 m/min speed, 0.05 µm/tooth chip load, 30 µm depth, 24 mm milling length, MQL.

Figure 50 (a) shows the area of flat end mill magnified for viewing tool wear and BUE. Figure 50 (b) shows SEM image of a cutting edge of uncoated WC tool at cutting speed of 10 m/min and a chip load of 0.05 µm/tooth for a total milling length of 24 mm. Tool wear is obvious on the cutting edge. The arrows in Figure 51 (a) point towards the viewing direction in Figure 51 (b). Also from Figure 51 (b), significant BUE is observed on the tool cutting edge. Energy dispersive X-ray spectroscopy revealed the presence of tungsten and cobalt (materials from uncoated WC tool) and iron, cobalt and nickel (materials from BUE) (Figure 52 and Table 14). Similarly Figure 53 (a) shows area of flat

end mill viewed in Figure 53 (b). Figure 53 (b) contains SEM image of the cutting edge of uncoated WC tool after micro milling at 60 m/min cutting speed and 1 µm/tooth chip load. A lot of tool wear is observed on the cutting edge with little BUE on the rake surface.

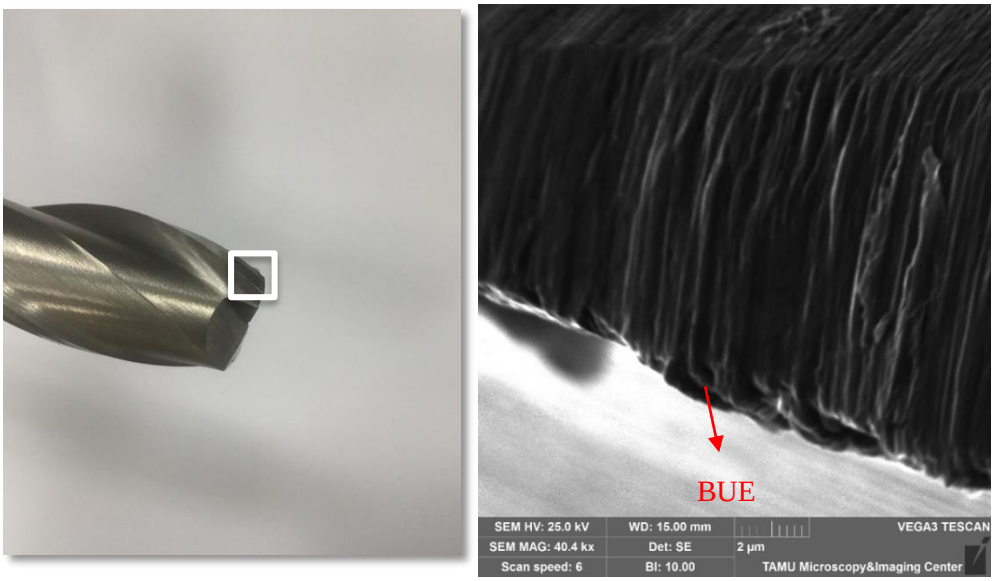

(a) (b)

Figure 51. (a) Flat end mill with arrows pointing towards view area of micro end mill tool. (b) Scanning electron microscopy image of cutting edge. Uncoated WC tool with BUE, Φ0.406 mm, 10 m/min speed, 0.05 µm/tooth chip load, 30 µm depth, 24 mm milling length, MQL.

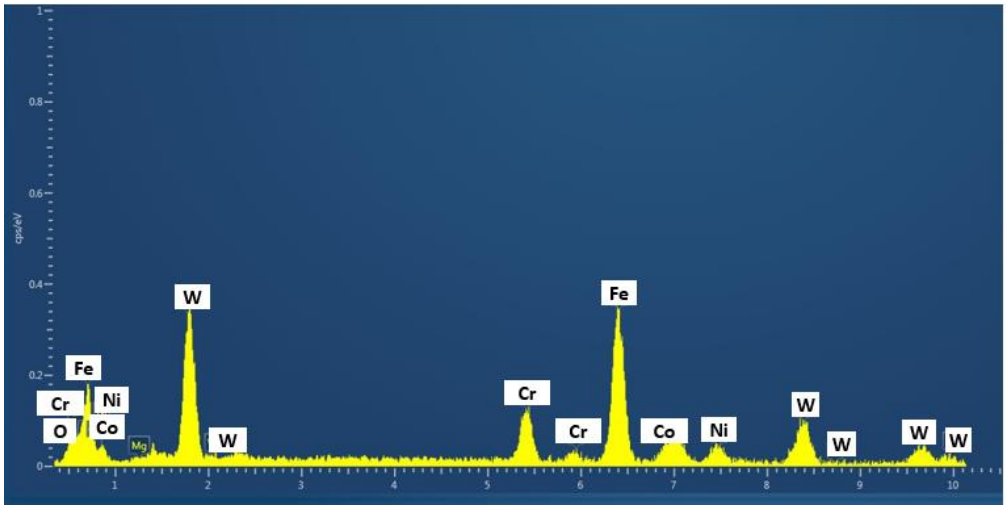

Figure 52. Energy dispersive X-ray spectroscopy results of BUE on tool.

Table 14. EDS of BUE on cutting edge, Uncoated WC tool with BUE, Φ0.406 mm, 10 m/min speed, 0.05 µm/tooth chip load, 30 µm depth, 24 mm milling length, MQL.

Material	**Weight (%)**
W	40.3
Fe	32.5
O	8.6
Cr	8.5
Ni	5.3
Co	4.3

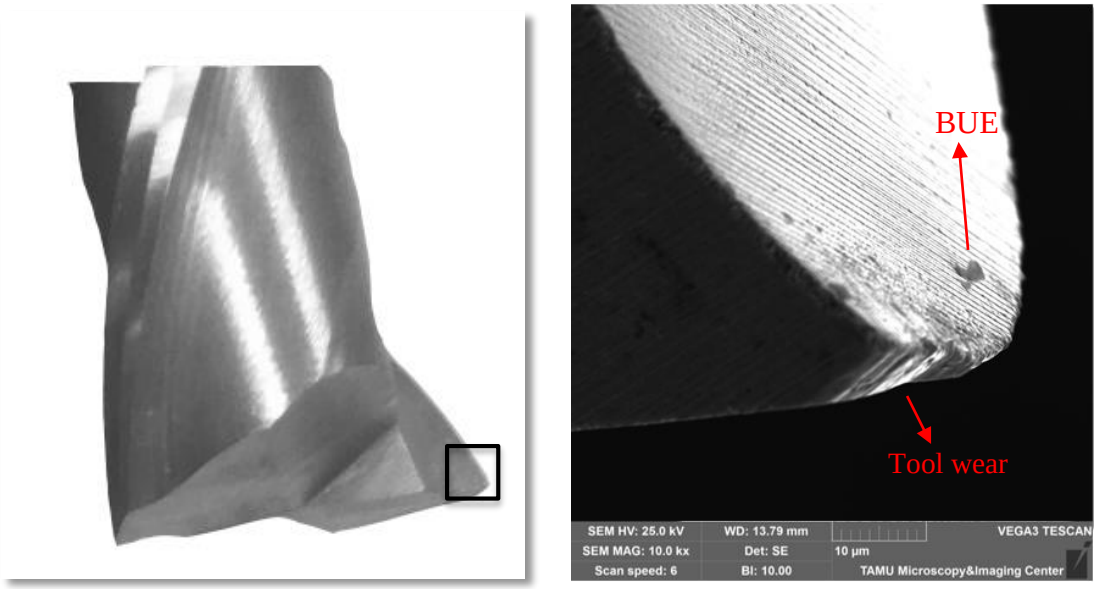

(a) (b)

Figure 53. (a) Flat end mill showing view area of micro end mill tool. (b) Scanning electron microscopy image of rake surface and cutting edge. Uncoated WC tool with BUE, Φ0.406 mm, 60 m/min speed, 1 µm/tooth chip load, 30 µm depth, 24 mm milling length, MQL.

Figure 54 (a) shows the area of a flute magnified for viewing BUE. Figure 54 (b) shows BUE formed after machining pure titanium with Φ0.8 mm AlTiN coated WC tool for 4 slots of 12 mm each at chip loads of 2,4,6 and 8 µm/tooth and 10 m/min cutting speed. Since the same cutting tool was used for milling all the 4 slots, considerable tool wear and BUE was observed on the cutting edge and rake surface.

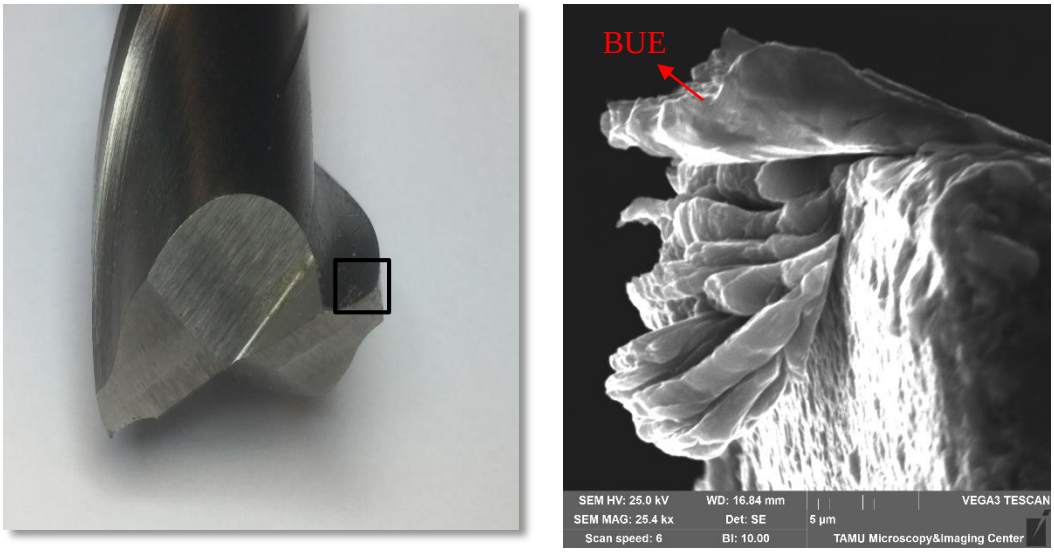

(a) (b)

Figure 54. (a) Flat end mill showing view area of micro end mill tool. (b) Scanning electron microscopy image of rake surface and cutting edge. AlTiN WC tool with BUE, Φ0.800 mm, 10 m/min speed, 2-8 µm/tooth chip load, 30 µm depth, 48 mm milling length, MQL.

5.7.2 Surface roughness

Average roughness values (S_a) were between 0.1 µm to 0.2 µm for cutting speeds below 30 m/min and there was shift in roughness values to below 0.1 µm when milling at cutting speeds increased over 40 m/min (Figure 55). Childs (2011) reported that as cutting speed increases from 0.5 m/min to 40 m/min, the maximum temperature at rake surface increases from 80 ºC to 500 ºC and at low temperatures the strain rate levels led to BUE formation. This can be avoided by machining at cutting speeds >40 m/min. The raw data for surface roughness are tabulated in appendix D.

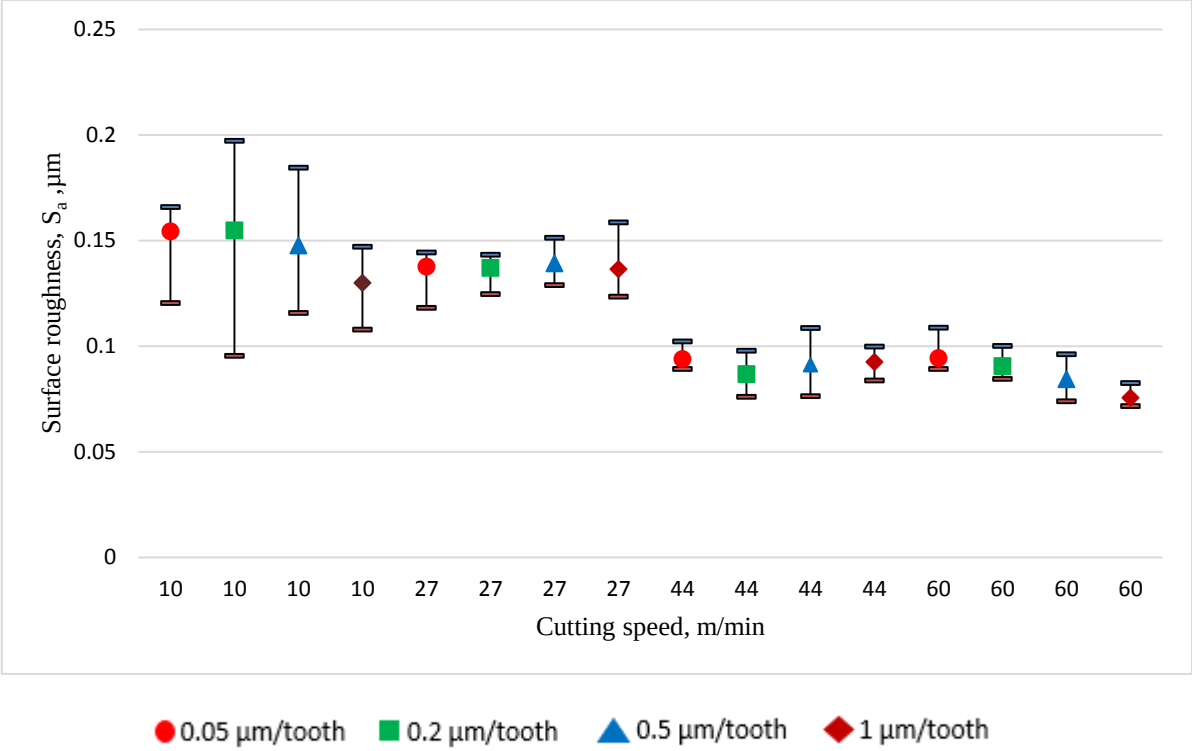

Figure 55. Surface roughness S_a (average of 15 values) measured at center of slot. Micro milling, 316L stainless steel, 10-60 m/min speed, 0.05-1 µm/tooth chip load, 30 µm depth, Φ0.406 mm uncoated WC flat end mill, 2 flutes, MQL.

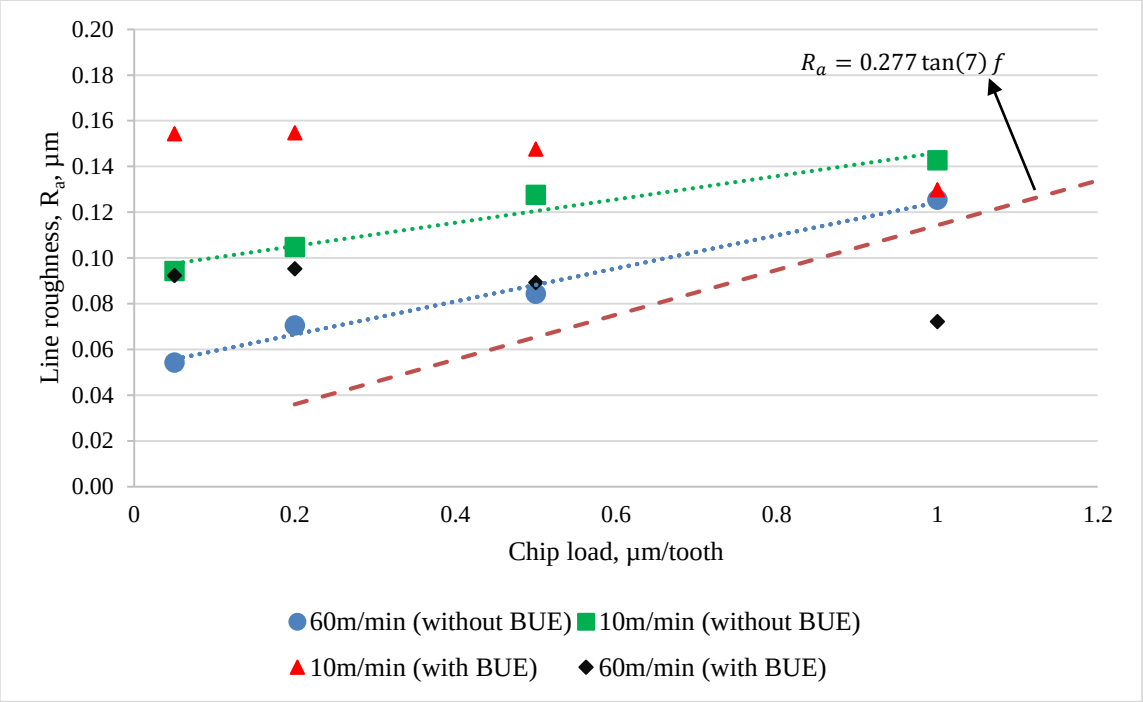

Figure 56. Predicted and actual line roughness, R_a values of slots measured at center. 316L stainless steel, Φ0.406 mm uncoated WC tool, 2 flute, 10-60 m/min speed, 0.05-1 µm/tooth chip load, 30 µm depth, MQL, 7° concavity angle.

Equation (6) was used to predict line roughness of micro milled slots on 316L stainless steel workpiece. According to equation (6), chip load and concavity angle of tool determined the line roughness, under the assumption that surface was free from BUE. It can be observed from Figure 56 that when the line roughness was measured at places in absence of BUE, the equation performed considerably well in predicting the line roughness accurately. However, when the line roughness was measured at places in presence of BUE, the equation failed to predict accurately. This is because BUE masks the actual effect of chip load on line roughness. Figure 57 shows surface finish data of micro milling of 316L stainless steel and meso milling of aluminum 6061-T6 combined into single plot.

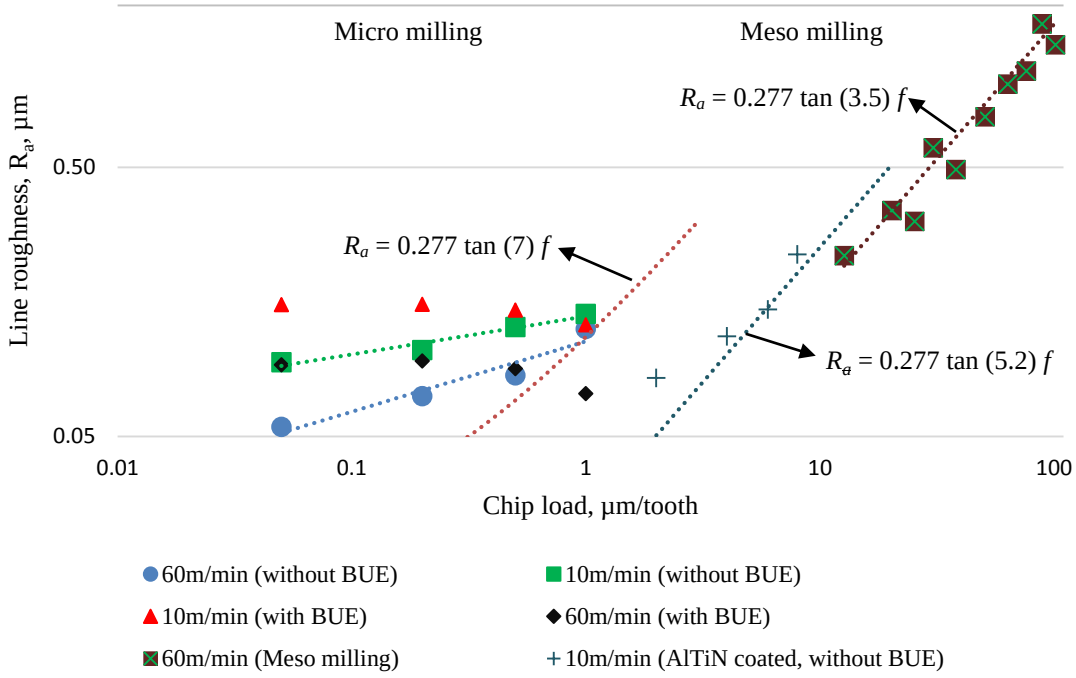

Figure 57. Predicted and actual line roughness, R_a values of slots measured at center.

- 316L stainless steel: Φ0.406 mm uncoated WC tool, 2 flute, 10-60 m/min speed, 0.05-1 µm/tooth chip load, 30 µm depth, MQL, 7° concavity angle.
- Pure titanium: Φ0.8 mm AlTiN coated WC tool, 1 flute, 10 m/min speed, 2-8 µm/tooth chip load, 30 µm depth, dry, 5.2° concavity angle.
- 6061-T6 aluminum: Φ3.175 mm uncoated high speed steel tool, 2 flute, 60 m/min speed, 12.7-101.6 µm/tooth chip load, 100 µm depth, dry, 3.5° concavity angle.

5.7.3 Tool wear

Tool wear was also observed during micro milling 316L stainless steel with uncoated WC flat end mills. Average tool wear was calculated as area loss of cutting tool material at the cutting edge radius on both the flutes of a milling cutter (Figure 58-59). The area loss was multiplied by the depth of cut to get the volumetric loss.

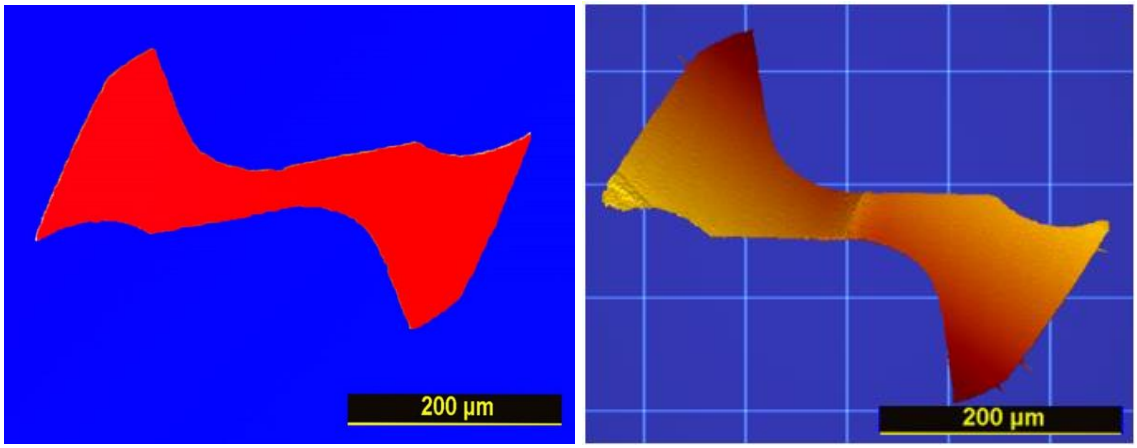

(a) (b)

Figure 58. (a) Top view of new micro tool (b) Top view of micro tool after 24 mm milling distance, 316L stainless steel, 27 m/min speed, 1 µm/tooth chip load, Φ0.406 mm uncoated WC tool, 30 µm depth, MQL.

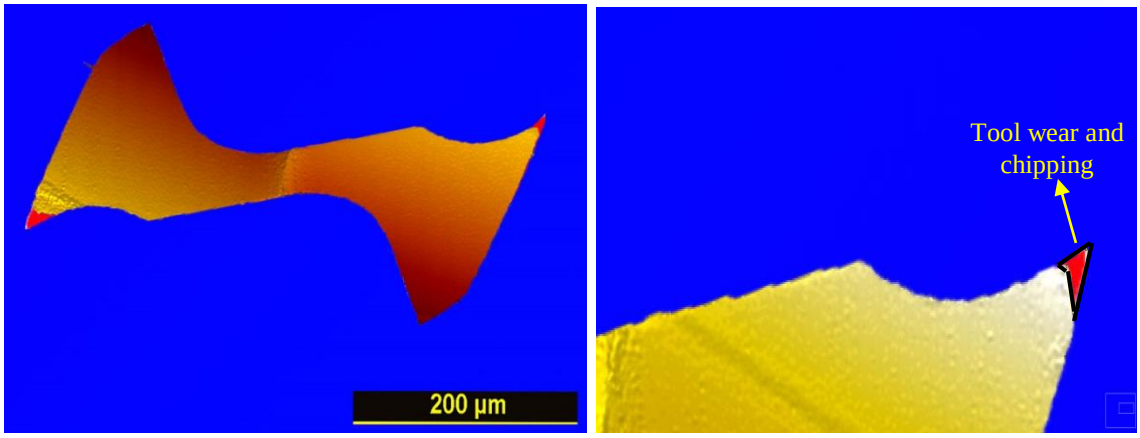

(a) (b)

Figure 59 (a) Top view of machined tool superimposed on top view of new micro tool (b) One of the cutting edges magnified to calculate tool wear and chipping after milling 24 mm, 316L stainless steel, 27 m/min speed, 1 µm/tooth chip load, Φ0.406 mm uncoated WC tool, 30 µm depth, MQL.

Since the cutting conditions (chip load and cutting speed) are different for each slot, machining times are different for each slot as shown in Table 15. All the slots were machined for an equal distance of 24 mm with unequal milling times. The wear rate (after each second of machining time) and tool wear per machining length were calculated for comparison.

Table 15. Tool wear and chipping for micro milling experimental conditions, 316L stainless steel workpiece, Φ0.406 mm uncoated WC tool, MQL

Cutting speed (m/min)	Chip Load, (µm /tooth)	Total machining time (seconds)	Average tool wear ($µm^3$)	Tool wear rate ($µm^3$/sec)	Tool wear per machining length ($µm^3$/mm)
10	0.05	918.5	3535	2	147
	0.2	340.2	4348	6	181
	0.5	208.7	2683	6	111
	1	153.1	1491	5	62
27	0.05	229.6	4341	9	181
	0.2	85.0	3681	22	153
	0.5	52.2	2511	24	105
	1	38.3	2931	38	122
44	0.05	91.8	12255	67	511
	0.2	34.0	7632	112	318
	0.5	20.9	1941	46	81
	1	15.3	1797	59	75
60	0.05	45.9	6293	69	262
	0.2	17.0	4261	125	178
	0.5	10.4	1474	71	61
	1	7.7	2587	169	108

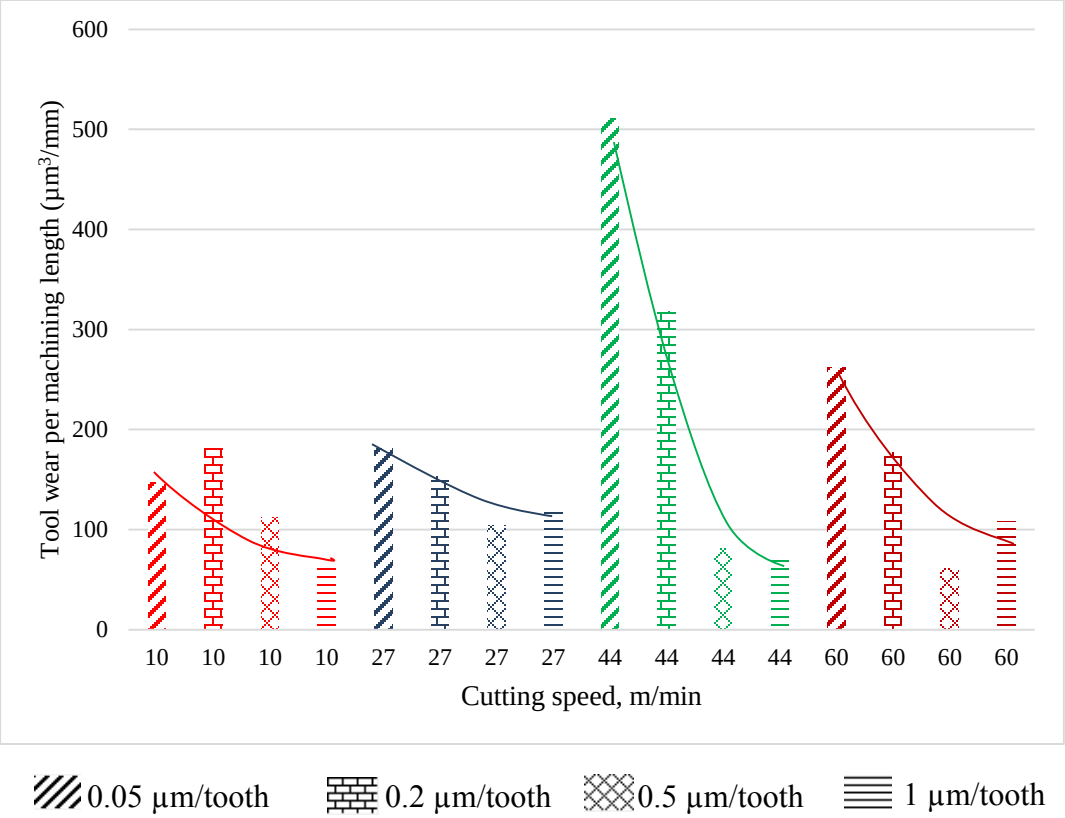

Figure 60. Average tool volumetric loss per machining length after micro machining slots with 10-60 m/min cutting speed, 0.05-1 µm/tooth chip load, 30 µm depth, Φ0.406 mm uncoated WC flat end mill, 2 flutes, 316L stainless steel workpiece.

Figure 60 shows that tool wear per machining length is highly dependent on chip load and speed. As chip load was increased from 0.05 µm/tooth to 1 µm/tooth, tool wear decreased for the same milling distance. For the same distance, the distance travelled by tool edge radius is more at low chip loads over high chip loads resulting in large tool wear at low chip loads. Also for same chip loads, tool wear increases with increase in cutting speed. The results agreed well with study conducted by Rahman et al. (2001) on micro milling copper where they suggested that tool wear increases with decrease in depth of cut and increase in cutting speed. Although tool wear increases at high cutting speeds, a

decrease in surface roughness (S_a) was observed due to absence of BUE at high speeds (Figure 55). Similar results were obtained by Song and Jian (2010) after milling Ti-6Al-4V alloy with a 25 mm diameter H25 tool steel.

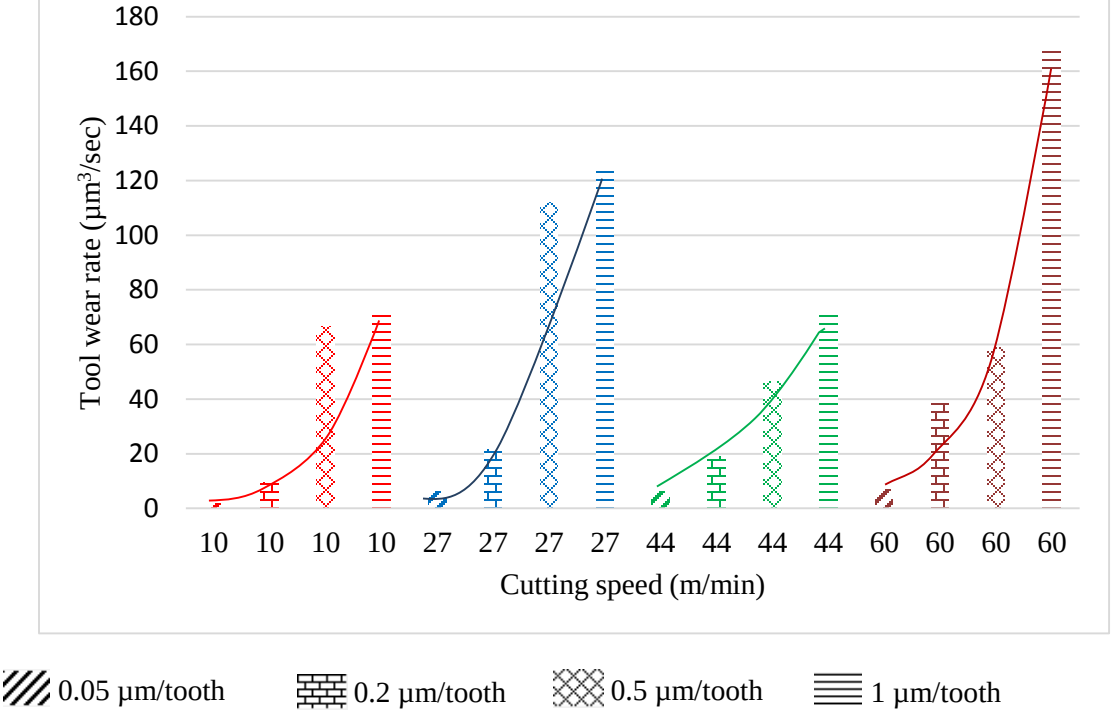

Figure 61. Average tool volumetric loss per machining time after micro machining slots with 10-60 m/min cutting speed, 0.05-1 µm/tooth chip load, 30 µm depth, Φ0.406 mm uncoated WC flat end mill, 2 flutes, 316L stainless steel workpiece.

Another quantifier for measuring tool wear with respect to machining time is tool wear rate (µm^3/sec) (Figure 61). This is applicable when tool life criteria in terms of time is necessary. Since at high chip loads, the machining time was less, tool wear rate was high. Similarly, for same chip load and different cutting speeds, tool wear rate increases with increase in cutting speed.

5.7.4 Surface roughness prediction including BUE density and tool wear volume

Formation of BUE in micro milling was prevalent and therefore equation (6) is not able to accurately predict line roughness. Hence a new model including the effect of BUE is developed. A null hypothesis is assumed that this difference (delta) between actual roughness and predicted roughness due to equation (6) is not due to BUE and tool wear.

$$R_a = 0.277 \tan(\alpha)\, f + \Delta \quad (8)$$

A model is fit in R with BUE and tool wear as variables and this difference as response variable. It is observed from Table 16 that both BUE and tool wear are significant predictors of delta due to their small p-values and thus the null hypothesis is rejected.

Table 16. Final model using R statistical software for difference between predicted roughness and actual roughness

Variable	**Estimate**	**Std. Error**	**p value**
Intercept	-2.263×10^{-01}	5.375×10^{-02}	0.00102
BUE density (#/mm^2)	3.575×10^{-05}	9.790×10^{-06}	0.00293
Tool wear volume (μm^3)	1.890×10^{-05}	6.042×10^{-06}	0.00799

$$\Delta = (3.575 \times 10^{-05} * \text{BUE}) + (1.890 \times 10^{-05} * \text{tool wear volume}) \quad (9)$$

$$R_a = 0.277 \tan(\alpha)\, f + (3.575 \times 10^{-05} * \text{BUE}) + (1.890 \times 10^{-05} * \text{tool wear volume}) \quad (10)$$

Hence a model including the effect of BUE and tool wear is added to equation (6). Equation (10) is able to predict line roughness accurately for micro milling considering the effect of BUE and tool wear.

Also, a model is developed to study the effect of input variables on BUE formation (Equation 11). Cutting speed, chip load, tool wear and interaction among them are fit with BUE density as response variable. After series of iterations, unimportant variables are removed from successive models and it is found that cutting speed has significant influence on BUE (Table 17).

Table 17. Final model using R statistical software for difference between predicted roughness and actual roughness

Variable	**Estimate**	**Std. Error**	**p value**
Intercept	7708.40	971.29	2.44×10^{-06}
Chip load (μm/tooth)	4264.33	3243.31	0.2113
Cutting speed (m/min)	-144.33	63.04	0.0394

BUE density = 7708.40 + (4264.33 chip load) - (144.33 * cutting speed) (11)

5.7.5 Surface roughness prediction including BUE density and tool wear volume using curve fitting

A new model including the effect of BUE is developed by combining equation (6) with data fitting line as in equation (12).

$$R_a \text{ (micro range)} = 0.0061\, f + 0.0872 \quad (12)$$

The above model is a linear fit of the difference between actual line roughness and predicted line roughness (equation (6)). This difference, delta is considered to be due to BUE formation in micro milling. Thus a modified equation, combining equation (6) and (12) can be used to predict line roughness for both meso and micro milling (equation (13)).

$$R_a = [0.277 \tan(\alpha)\, f] + [0.0061\, f + 0.0872] \quad (13)$$

$$= [0.277 \tan(7)\, f] + [0.0061\, f + 0.0872]$$

$$R_a = 0.040\, f + 0.0872 \quad (14)$$

Figure 62 plots equations (10), (13) and (6) for 7^o concavity angle and superimposes micro milling data for tools with the same concavity angle. It can be observed that equation (14) is able to predict line roughness accurately for both micro and meso milling. Since BUE has a lot of effect on line roughness values in micro milling, the difference in predicted line roughness using equation (6) and (14) is high at chip loads below 3 μm/tooth. As we make a transition to meso milling, formation of BUE doesn't impact roughness as much as it would in micro milling and hence the difference is quite small.

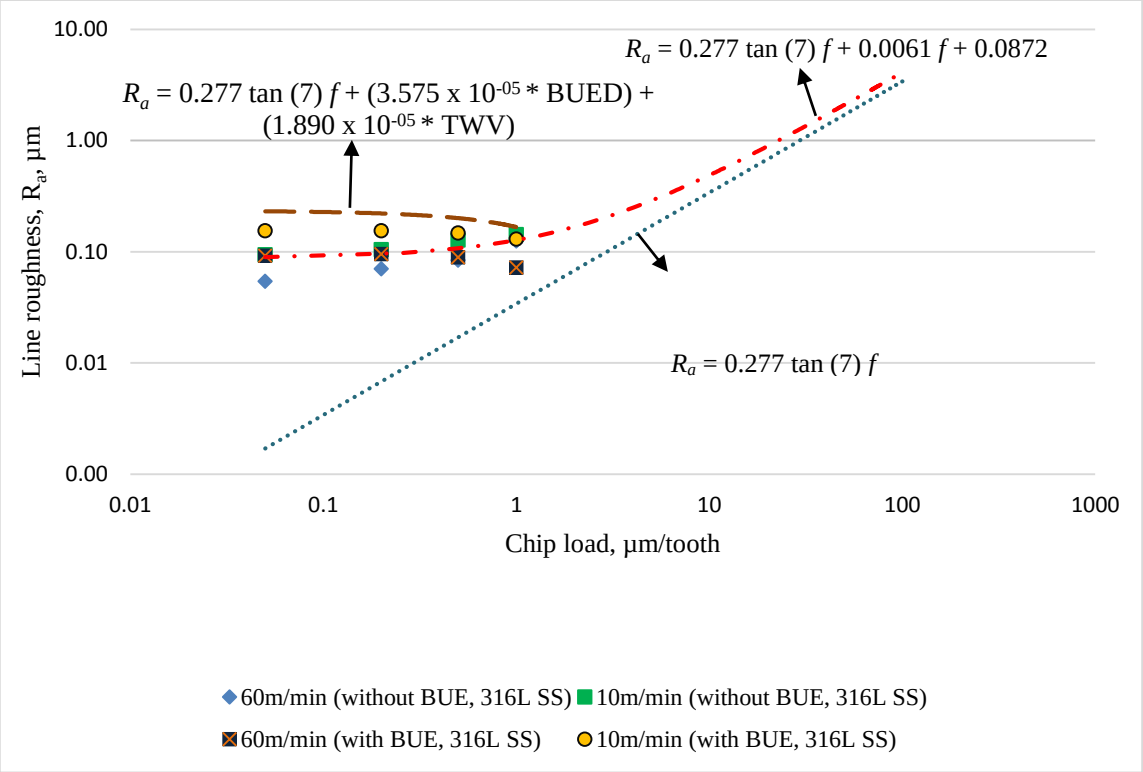

Figure 62. Predicted and actual line roughness, R_a values of slots measured at center. 316L stainless steel, Φ0.406 mm uncoated WC tool, 2 flute, 10-60 m/min speed, 0.05-1 µm/tooth chip load, 30 µm depth, MQL, 7° concavity angle.

6. CONCLUSIONS

Meso milling of Aluminum 6061 T6, A36 carbon steel and micro milling of 316L stainless steel were carried out. The experimental study shows:

1. A surface finish model was derived for both meso and micro milling; the line roughness R_a is a function of chip load and tool concavity angle. At chip loads below 3 μm/tooth, where the effect of BUE on line roughness is significant, the surface finish model predicted a higher line roughness over conditions in absence of BUE. However as we increase the chip loads above 3 μm/tooth, the effect of BUE on roughness is small and the difference between predicted roughness in presence of BUE and absence of BUE is small.
2. A combination of high cutting speed with MQL resulted in best surface finish in meso milling of A36 carbon steel. It was also observed that AlTiN coated WC tools produce less BUE and smooth surface finish compared to uncoated WC tools.
3. Built-up-edge density is high at low cutting speeds (<30 m/min) and low at high cutting speeds (>40 m/min). Also BUE formation is minimal at high chip load conditions. This is because of shear dominated cutting mechanism at high chip loads and ploughing dominated cutting mechanism at low chip loads.
4. Surface roughness is low at high cutting speeds (>40 m/min) and high at low cutting speeds (<30 m/min). However tool wear per machining length is more at high cutting speeds. Hence, to achieve a smooth surface with minimum BUE and longer tool life, higher cutting speeds (>40 m/min) and chip loads (> 0.5 μm/tooth) are to be selected.

7. RECOMMENDATIONS AND FUTURE WORK

1. This research can be extended to different type of tool coatings and other workpiece materials to study effect of BUE on surface roughness on wide range of chip loads. Also this data can be used to test the validity of combined line roughness model proposed which compensates for BUE formation in milling. A BUE adhesion and welding to cutting tool depends on the surface of tool material and cutting condition.
2. Study of BUE density and machining conditions by observing machined chips.
3. Analyze tool vibration data to detect BUE.
4. Tool diameters with 0.050 mm can be machined with CNC milling machines capable of reaching 200,000 RPM and 400,000 RPM for cutting speeds of 30 m/min and 60 m/min respectively.
5. A device for tool offset measurements can be developed to shorten set up time for micro milling experiments.
6. Using atomic force microscope (AFM) to measure surface roughness of micro milled surface while avoiding BUE.

REFERENCES

Aramcharoen, A., Mativenga, P.T., 2009. Size effect and tool geometry in micromilling of tool steel. Precision Engineering 33, 402-407.

Aramcharoen, A., Mativenga, P.T., Yang, S., Cooke, K.E., Teer, D.G., 2008. Evaluation and selection of hard coatings for micro milling of hardened tool steel. International Journal of Machine Tools and Manufacture 48, 1578-1584.

AZoM™. Grade 316L, A36 – properties, fabrication and applications, [Online]. Available: http://www.azom.com/ [Accessed Dec 22, 2014].

Bourne, M.A., 2007. A Consumer's Guide to MEMS & Nanotechnology. Bourne Research [Accessed Nov 19, 2014].

Byrne, G., Dornfeld, D., Denkena, B., 2003. Advancing Cutting Technology. CIRP Annals - Manufacturing Technology 52, 483-507.

Childs, T.H.C., 2011. Towards simulating built-up-edge formation in the machining of steel. CIRP Journal of Manufacturing Science and Technology 4, 57-70.

Clausing Industrial, Surface grinder properities, [Online]. Available: http://www.clausing-industrail.com/ [Accessed Jan 29, 2015].

Cui, X., Zhao, J., Jia, C., Zhou, Y., 2012. Surface roughness and chip formation in high-speed face milling AISI H13 steel. The International Journal of Advanced Manufacturing Technology 61, 1-13.

Dmytro, B., 2013. Surface finish modeling in micro milling of biocompatible materials. Texas A&M University, College Station.

Fang, N., Pai, P.S., Edwards, N., 2010. Prediction of built-up edge formation in machining with round edge and sharp tools using a neural network approach. International Journal of Computer Integrated Manufacturing 23, 1002-1014.

Furukawa, Y., Moronuki, N., 1988. Effect of Material Properties on Ultra Precise Cutting Processes. CIRP Annals - Manufacturing Technology 37, 113-116.

Groover, M.P. (2004). Fundamentals of Modern Manufacturing. New York: John Wiley & Sons.

HAAS CNC, OM2 milling machine, [Online]. Available: http://www.haascnc.com/ [Accessed Oct 18, 2014].

Heginbotham, W., Gogia, S., 1961. Metal cutting and the built-up nose. Proceedings of the Institution of Mechanical Engineers 175, 892-917.

Ikawa, N., Shimada, S., Tanaka, H., 1992. Minimum thickness of cut in micromachining. Nanotechnology 3(1), 6.

Iwata, K., Ueda, K., 1980. Fundamental analysis of the mechanism of built-up edge formation based on direct scanning electron microscope observation. Wear 60, 329-337 52.

Keyence sensors, Keyence LK-G82 laser displacement sensor, [Online]. Available: http://www.keyence.com/ [Accessed March 14, 2015].

Lai, X., Li, H., Li, C., Lin, Z., Ni, J., 2008. Modelling and analysis of micro scale milling considering size effect, micro cutter edge radius and minimum chip thickness. International Journal of Machine Tools and Manufacture 48, 1-14.

Liu, X., DeVor, R.E., Kapoor, S., Ehmann, K., 2004. The mechanics of machining at the microscale: assessment of the current state of the science. Journal of manufacturing science and engineering 126, 666-678.

Masaki, T., Kawata, K., Masuzawa, T., 1990. Micro electro-discharge machining and its applications, Micro Electro Mechanical Systems, 1990. Proceedings, An Investigation of Micro Structures, Sensors, Actuators, Machines and Robots. IEEE. IEEE, pp. 21-26.

Masuzawa, T., 2000. State of the Art of Micromachining. CIRP Annals - Manufacturing Technology 49, 473-488.

McKeown, P., 1986. High precision manufacturing and the British economy. Proceedings of the Institution of Mechanical Engineers, Part B: Journal of Engineering Manufacture 200, 147-165.

MSC Industrial Supply, Meso tool properties, [Online]. Available: http://www.mscdirect.com/ [Accessed Nov 24, 2014].

Oberg, E., Jones, F., Horton H., Ryfeel H., 2009. Machinery's hand book 29th edition, New York: Industrial Press Inc,.

Olympus corporation, Optical microscope, [Online]. Available: http://www.olympusamerican.com/ [Accessed Oct 29, 2014].

Peng, F.Y., Wu, J., Yuan, S., Yan, R., 2012. The Effect of Vibration on the Surface Topography in Micro-Milling. Applied Mechanics and Materials 217, 1791-1801.

Performance Micro Tools, Micro tool properties, [Online]. Available: http://www.pmtnow.com/ [Accessed Dec 21, 2014].

Rahman, M., Senthil A.K., Salam, M.U., 2001. Experimental evaluation on the effect of minimal quantities of lubricant in milling. International Journal of Machine Tools and Manufacture 42, 539-547.

Sasaki, T., Takeuchi, Y., Kawai T., Sakaida Y., 2004. 5-Axis Control Ultraprecision Micromachining of Micro 3-D Body. Proceedings of the Spring Annual Meeting of JSPE, 1075-1076.

Shahabi, H., Ratnam, M., 2010. In-cycle detection of built-up edge (BUE) from 2-D images of cutting tools using machine vision. The International Journal of Advanced Manufacturing Technology 46, 1179-1189.

Shimada, S., Ikawa, N., Tanaka, H., Ohmori, G., Uchikoshi, J., Yoshinaga, H., 1993. Feasibility study on ultimate accuracy in microcutting using molecular dynamics simulation. CIRP Annals-Manufacturing Technology 42, 91-94.

Shimada, S., Tanaka, H., Higuchi, M., Yamaguchi, T., Honda, S., Obata, K., 2004. Thermo-chemical wear mechanism of diamond tool in machining of ferrous metals. CIRP Annals-Manufacturing Technology 53, 57-60.

Song Z., Jian-feng L., 2010. Tool wear criterion, tool life and surface roughness during high speed end milling Ti-6Al-4V alloy. Applied physics and engineering 11, 587-595.

Snoeys, R., Staelens, F., Dekeyser, W., 1986. Current trends in non-conventional material removal processes. CIRP Annals-Manufacturing Technology 35, 467-480.

Steel Grades, A36-properties, fabrication and applications, [Online]. Available: http://www.steel-grades.com/ [Accessed 7 Dec, 2014].

Sujeev, C., 2009. Failure prediction and stress analysis of micro cutting tools. Texas A&M University, College Station.

Sukvittayawong, S., Inasaki, I., 1994. Detection of built-up edge in turning process. International Journal of Machine Tools and Manufacture 34, 829-840.

Sutherland, J., Babin, T., 1988. The geometry of surfaces generated by the bottom of an end mill. Transaction of NAMRC 16, 202-208.

Taniguchi, N., 1983. Current status in, and future trends of, ultraprecision machining and ultrafine materials processing. CIRP Annals-Manufacturing Technology 32, 573-582.

Tescan Vega 3, Scanning electron microscope, [Online]. Available: http://www.tescan.com/ [Accessed April 15, 2015].

UNIST fluid systems, Oil Mist lubrication, [Online]. Available: http://www.unist.com/ [Accessed Dec 11, 2014].

Vogler, M.P., DeVor, R.E., Kapoor, S.G., 2004. On the modeling and analysis of machining performance in micro-endmilling, Part I: Surface generation. Journal of Manufacturing Science and Engineering 126, 685-694.

Wang, M.-Y., Chang, H.-Y., 2004. Experimental study of surface roughness in slot end milling AL2014-T6. International Journal of Machine Tools and Manufacture 44, 51-57.

Weule, H., Hüntrup, V., Tritschler, H., 2001. Micro-cutting of steel to meet new requirements in miniaturization. CIRP Annals-Manufacturing Technology 50, 61-64.

Yuan, Z., Zhou, M., Dong, S., 1996. Effect of diamond tool sharpness on minimum cutting thickness and cutting surface integrity in ultraprecision machining. Journal of Materials Processing Technology 62, 327-330.

Zawawi, M.Z., Shaharudin, M.A.H., Manaf, A.R.A., 2014. Influences of Varying Combination of Feed Rate and Depth of Cut to Tool Wear Rate and Surface Roughness: High Speed Machining Technique in Non-High Speed Milling Machine. Advanced Materials Research 903, 194-199.

Zorev, N.N., 1966. Metal cutting mechanics. Pergamon, Headington hill hall, Oxford, England. 1966, 526P.

Zygo 3D optical surface profiler, Surface roughness measurements, [Online]. Available: http://www.zygo.com/ [Accessed Nov 28, 2014].

APPENDIX A

SPECIFICATIONS OF EQUIPMENT

A.1 HAAS OM2 CNC Milling machine

The HAAS OM2 milling machine is a 5 axis machine (X, Y, Z, A and B).

Specifications:

1. The maximum travel for X, Y and Z axis are 305 mm x 254 mm x 305 mm respectively.
2. The spindle runs on air bearings with a minimum rotational speed of 1000 RPM and maximum speed of 50,000 RPM.
3. The maximum rapid feed rate is 19.2 m/min and maximum cutting feed rate is 12.7 m/min.
4. The positioning accuracy is $\pm$5 µm and repeatability is $\pm$3 µm.

Figure A.1 HAAS OM2 CNC milling machine (HAAS, 2014)

A.2 CLAUSING CSG818H Surface Grinder

Specifications:

1. The table size for the surface grinder is 203 mmX460 mm with a maximum grinding length of 480 mm and maximum grinding width of 238 mm.
2. The grinding spindle drive is powered by a 2 HP motor with a speed of 3450 RPM.
3. The diameter of the standard grinding wheel is 203 mm and width between 12.7 mm-19 mm.

Figure A.2 CLAUSING Surface grinder (Clausing, 2014)

A.3 UNIST lubrication system

1. Unist lubrication system was used to supply micro-mist during machining.
2. A liquid metering pump exists to generate 5-200 pulse/minute.
3. An air metering screw exists to control the flow of air atomizing out the nozzle.

4. The amount of coolant (drops per cycle) and ratio of coolant to pressurized air can be adjusted according to needs.
5. Cool lube 2210 was used as a lubricant for cooling workpiece and tool. It reduces coefficient of friction, μ at tool and workpiece interface.

Figure A.3 UNIST micro mist system with its components (Unist, 2015)

A.4 Olympus optical microscope

1. Olympus STM6 with a motorized 3-axis type microscope was used.
2. The dimensions of the observation table are 465 mmX437 mm. The minimum readout on the counter was 0.1 μm
3. Repeatability of objective lens with 10X and 20X was 2 μm and with 50X was 1 μm

Figure A.4 Olympus STM6 microscope (Olympus, 2015)

A.5 Keyence Laser displacement sensor

1. The main part of laser displacement sensor consists of a laser head (LK-G82) with a reference distance of 80 mm±15 mm.
2. The laser head emits a red semiconductor laser with a wavelength of 655 nm.
3. The repeatability of this device is about 0.2 µm and has a resolution of 0.1 µm.
4. The laser head weighs about 380grams including cables.
5. LK Navigator software is used to tune the reflectivity of laser to the tool material.

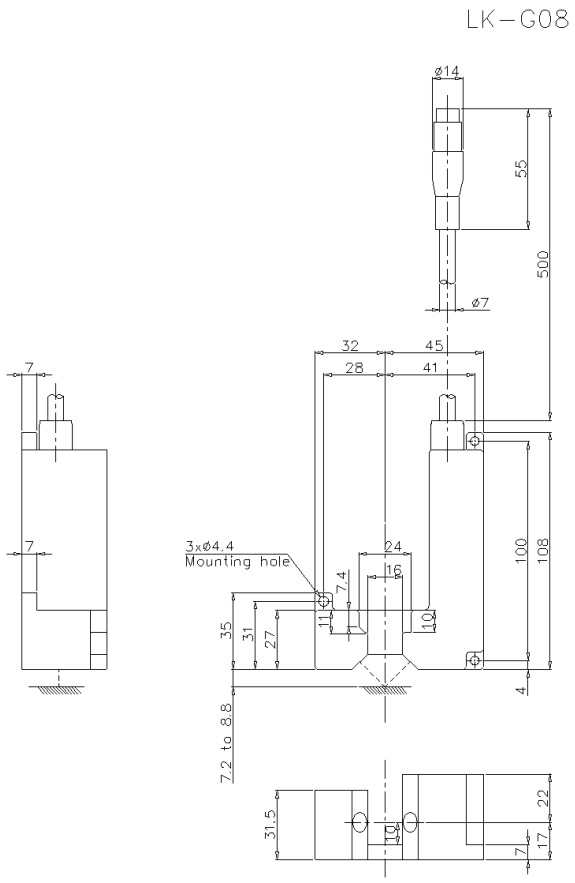

Figure A.5 CAD drawing of Keyence LKG-08 laser head (Keyence, 2015)

A.6 Zygo ZeGage 3D optical surface profiler

1. The physical dimensions of the workstation table are 74 cm X 127 cm X 76 cm and weighs 37 kilograms.
2. The part stage is an integrated T-slot plate with a travel of 50 mm X 100 mm travel in both X and Y directions. It tips/tilts to an angle of 4^0.
3. The Z-stage has a travel of 100 mm and has a 10X objective lens attached.
4. The Zygo ZeGage comes with a ZeMaps software integrated with inbuilt functions for image processing.

5. The surface topography has a repeatability of less than 3.5 nm with a data scan rate of less than 23 μm/sec.

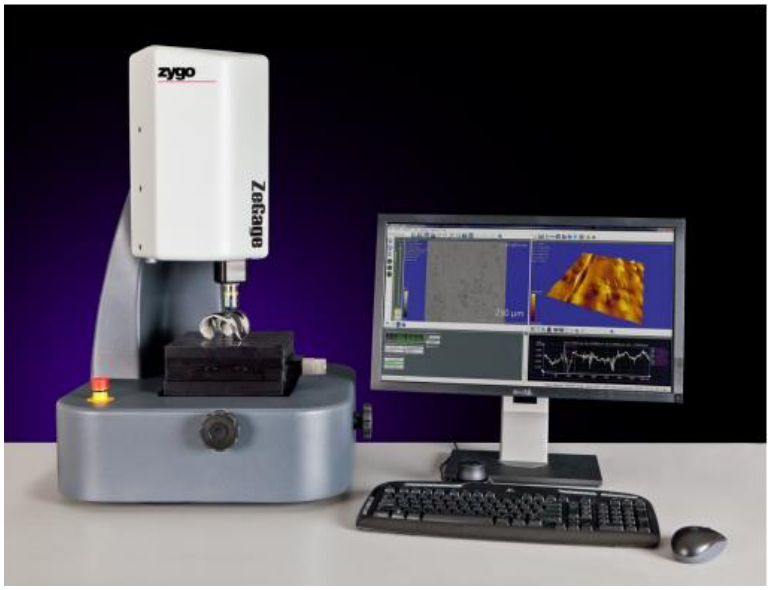

Figure A.6 Zygo ZeGage 3D optical surface profiler (Zygo, 2015)

A.7 TESCAN Vega LM3

1. The Vega LM3 has a tungsten heated cathode electron gun. The resolution is 3 nm at 30kV/2 nm at 30kV. The chamber pressure is less than 9 X 10^{-3} Pa.

2. The magnification can be varied from 2x-100000x.

3. The scanning speed varies from 20 ns to 10 ms per pixel adjustable in steps.

4. The table movement is Comp centric, fully motorized with a movement of 80 mm, 60 mm and 47 mm in X, Y and Z direction respectively. Also the table can be rotated 360^0 and can be tilted from -80^0 to 80^0.

Figure A.7 TESCAN Vega LM3 scanning electron microscope (TESCAN, 2015).

APPENDIX B

MODELLING OF LINE SURFACE ROUGHNESS IN FLAT END MILLING

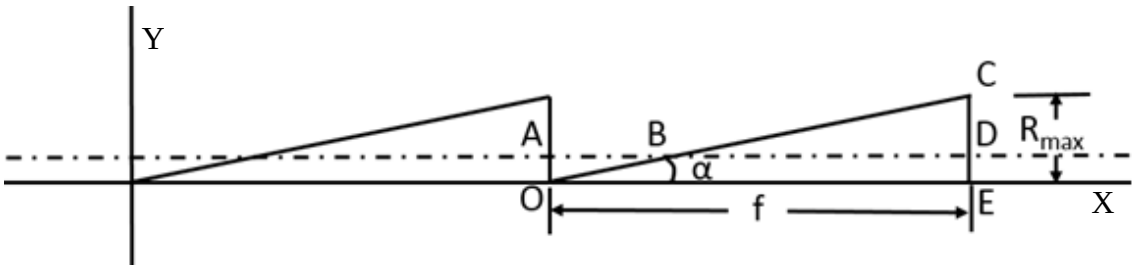

Figure B.1 Geometrical sketch representing simulated surface of a flat end mill

Figure B.1 is assumed to be the surface simulated by a flat end mill cutter. The concavity angle of the tool is a geometric property of the tool and depends on the manufacturer. It is assumed that the concavity angle effects the final geometry of the machined surface.

∠EOC=α be the concavity angle

EC = t = R_{max} be the maximum height of surface profile

OE = f = chip load

1. The center of gravity for a right angle triangle is at a distance of 1/3 from X-axis and 1/3 from the perpendicular side inside the triangle. Hence the dashed line is at a height t/3 from X-axis.

$$DE = \frac{1}{3}EC$$

$$DE = \frac{1}{3}t \quad \text{(B1)}$$

2. Also, Triangles CBD and COE are similar to each other

$$\frac{CD}{CE} = \frac{BD}{OE}$$

$$\frac{2}{3} = \frac{BD}{OE}$$

$$BD = \frac{2}{3}\, OE \tag{B2}$$

3. The value of AB can be found by subtracting BD from OE

$$AB = OE - BD$$

$$AB = OE - \frac{2}{3}OE$$

$$AB = \frac{1}{3}OE$$

$$AB = \frac{1}{3}\, f \tag{B3}$$

4. Tangent of Concavity angle is calculated

$$tan\alpha = \frac{t}{f} \tag{B4}$$

$$t = f * tan\alpha \tag{B5}$$

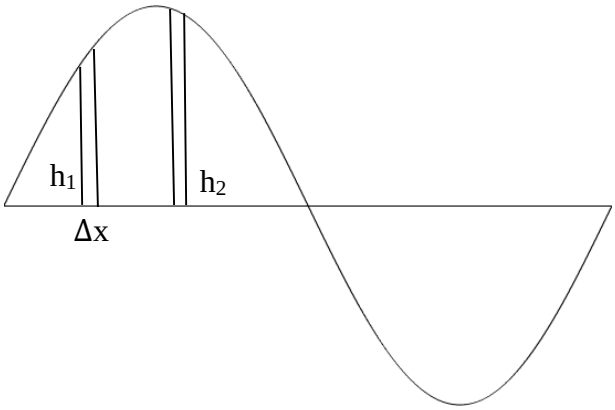

Figure B.2 Line roughness is calculated as the arithmetic average of infinitesimally small areas along a given length.

Let h_1, h_2, $h_3 \ldots h_n$ etc. be infinitesimally height of a surface when moving the same distance along the machined surface. The arithmetic average R_a is defined as

$$R_a = \frac{(h_1 + h_2 + h_3 \ldots . h_n)}{n} \tag{B6}$$

$$R_a = \frac{(h_1 \Delta x + h_2 \Delta x + h_3 \Delta x \ldots . h_n \Delta x)}{n * \Delta x}$$

$$R_a = \frac{(A_1 + A_2 + A_3 \ldots . A_n)}{L}$$

Hence,

5. Area of ΔOAB is calculated as

$$Area\ of\ \Delta OAB\ = \frac{1}{2} * Base * Height$$

$$Area\ of\ \Delta OAB\ = \frac{1}{2} * AB * OA$$

$$Area\ of\ \Delta OAB\ = \frac{1}{2} * \frac{f}{3} * \frac{t}{3}$$

$$Area\ of\ \Delta OAB\ = \frac{ft}{18} \tag{B7}$$

6. Area of ΔBCD is calculated as

$$Area\ of\ \Delta\mathrm{BCD}\ = \frac{1}{2} * \ Base\ * \ Height$$

$$Area\ of\ \Delta\mathrm{BCD} = \frac{1}{2} * \ BD * \ CD$$

$$Area\ of\ \Delta\mathrm{BCD}\ = \frac{1}{2} * \frac{2f}{3} * \frac{2t}{3}$$

$$Area\ of\ \Delta\mathrm{BCD} = \frac{2ft}{9} \qquad \text{(B8)}$$

7. Arithmetic Line roughness is calculated as follows:

$$R_a = \frac{Area\ of\ \Delta\mathrm{OAB} + Area\ of\ \Delta\mathrm{BCD}}{length\ of\ machined\ surface}$$

$$R_a = \frac{\frac{\mathrm{f\,t}}{18} + \frac{2f\ t}{9}}{f}$$

$$R_a = \frac{\frac{5f\ *\ f\ *\ tan\alpha}{18}}{f}$$

$$R_a = \frac{5\tan\alpha\ f}{18}$$

$$R_a = \ 0.277\tan(\alpha)\ f \qquad \text{(B9)}$$

APPENDIX C

CNC CODE

C.1 SPINDLE WARMUP PROGRAM

```
M03 S10000
G04 P120.
M03 S20000
G04 P180.
M03 S25000
G04 P180.
M03 S30000
G04 P180.
M03 S35000
G04 P180.
M03 S40000
G04 P180.
M03 S50000
G04 P180.
M05
M30
```

C.2 MESO AND MICRO SLOT MILLING PROGRAM

```
G00 G17 G40 G90                 (STANDARD START-UP SETTINGS)
G21                             (MILLIMETERS)
T1                              (IDENTIFIES TOOLING)
G43 H01                         (CALLS FOR TOOL LENGTH
COMPENSATION)
G90 G54 G01 X0. Y0. Z5. F50.    (MOVES MACHINE TO X Y ORIGIN AND Z
OFFSET) (COORDINATES SET IN LINE G54 IN OFFSETS)
N70 M97 P11111 L1               (SUB-ROUTINE)
(CONDITION 1)
S7839 M03
G90 G01 Z-0.03 F0.78
Z20. F20.
M30                             (HARD STOP)
```

APPENDIX D

EXPERIMENTAL DATA

Table D.1 Surface roughness values for meso milling of A36 carbon steel with coated and uncoated WC tool.

Tool coating	Depth of cut (µm)	Cutting fluid	Cutting speed (m/min)	Surface roughness, S_a, (µm)
Uncoated	50µm	Dry	15	1.015
Uncoated	50µm	Wet	80	0.584
Uncoated	100µm	Dry	80	1.066
Uncoated	100µm	Wet	15	0.997
Coated	50µm	Dry	80	0.332
Coated	50µm	Wet	15	0.925
Coated	100µm	Dry	15	1.539
Coated	100µm	Wet	80	0.466

Table D.2 Experimental conditions for micro milling 316L stainless steel.

Run order	Condition	Chip Load (µm/tooth)	Cutting speed (m/min)
1	8	0.2	60
2	4	0.05	60
3	13	1	10
4	16	1	60
5	14	1	27
6	11	0.5	44
7	6	0.2	27
8	9	0.5	10
9	2	0.05	27
10	3	0.05	44
11	5	0.2	10
12	10	0.5	27
13	12	0.5	60
14	7	0.2	44
15	1	0.05	10
16	15	1	44

Table D.3 Average of 15 random surface roughness (S_a) values for micro milling 316L stainless steel.

Run order	Condition	Chip Load (µm/tooth)	Cutting speed (m/min)	Surface roughness, S_a, (µm), Average	Surface roughness, S_a, (µm), High	Surface roughness, S_a, (µm), Low
1	8	0.2	60	0.090533	0.10008	0.090533
2	4	0.05	60	0.094269	0.10871	0.094269
3	13	1	10	0.129849	0.14703	0.129849
4	16	1	60	0.075462	0.08263	0.075462
5	14	1	27	0.136354	0.15863	0.136354
6	11	0.5	44	0.091072	0.10869	0.091072
7	6	0.2	27	0.13705	0.14332	0.13705
8	9	0.5	10	0.147578	0.18454	0.147578
9	2	0.05	27	0.13762	0.14432	0.13762
10	3	0.05	44	0.093854	0.10222	0.093854
11	5	0.2	10	0.154764	0.19724	0.154764
12	10	0.5	27	0.139085	0.15134	0.139085
13	12	0.5	60	0.084304	0.09622	0.084304
14	7	0.2	44	0.086662	0.09783	0.086662
15	1	0.05	10	0.15426	0.16587	0.15426
16	15	1	44	0.092542	0.09977	0.092542

Table D.4 Measured BUE Density for micro milling 316L stainless steel, up milling.

Run order number	Measurement 1	Measurement 2	Measurement 3	Measurement 4	Measurement 5	Measurement 6	Measurement 7	Measurement 8	Measurement 9	Measurement 10
1	3500	3200	3500	3200	3800	2500	3900	3500	3100	3500
2	4000	3900	3800	3400	3100	3600	3900	3700	3900	4500
3	6400	5100	4000	4000	5500	3600	4800	5000	3000	4300
4	3500	3100	2500	2800	1900	2200	3900	2700	3100	2200
5	4400	4500	4400	3900	4800	3800	4400	4900	4700	4200
6	2300	2800	2400	3100	3700	3300	3000	4400	2900	4000
7	4900	5100	4900	4900	5700	5100	4700	4200	5000	5400
8	6300	5400	5300	4900	4800	4200	5800	6000	5800	5400
9	4900	5700	4300	4900	5500	6300	5500	5400	5200	4900
10	3200	4100	3900	2800	3400	3200	3500	4400	3700	3600
11	5500	6500	5800	4900	4500	6000	6200	6600	6500	4800
12	5500	5700	4200	4000	5500	3700	4600	4400	3500	4500
13	3700	3800	2800	3400	3400	3400	2900	2500	2900	2900
14	3400	3700	3500	2900	3800	3000	2800	2300	3600	4000
15	8900	7200	6600	7500	9800	7800	9800	10400	9900	9100
16	3400	2000	3100	2500	2200	2300	2400	2900	2100	2800

Table D.5 Measured BUE Density for micro milling 316L stainless steel, down milling.

Run order number	Measurement 1	Measurement 2	Measurement 3	Measurement 4	Measurement 5	Measurement 6	Measurement 7	Measurement 8	Measurement 9	Measurement 10
1	5000	3500	4500	3700	5200	3900	3200	1900	1900	2400
2	4900	4500	3700	2600	3900	3700	3900	4600	4500	4400
3	4700	4500	4700	4800	5200	5500	3100	4500	4300	4900
4	3000	3400	3000	3300	2600	2900	3200	4400	2400	2200
5	5100	4500	4400	3900	4800	3800	4400	4900	4700	4200
6	2600	3000	4300	2600	3100	4400	4800	2900	2100	3100
7	5800	6300	4600	5800	5000	6200	5400	5500	6400	5900
8	6200	6400	5800	5500	5700	6400	5200	5300	6300	5500
9	5400	5200	6000	5600	5600	3300	5500	6100	6000	5800
10	3300	3700	4200	3500	3900	2500	3400	3900	4900	3900
11	5600	6200	6300	5900	5400	6200	6000	5900	5100	6600
12	5400	5700	5100	4900	4900	4600	4800	5100	5500	5500
13	3100	2700	3300	3800	4500	2700	2500	2900	5000	3000
14	4100	3200	3500	3500	3400	4000	3900	3700	2900	3600
15	10400	11500	10300	11200	9900	10300	11400	10500	12500	11100
16	3300	3100	3400	3100	3300	2400	2200	2600	2500	2300

Table D.6 Measured tool wear for micro milling 316L stainless steel.

Run order	Tool wear, side 1 (μm^3)	Tool wear, side 2 (μm^3)	Total average tool wear (μm^3)
1	4497	1365	2931
2	1023	1960	1491
3	6443	6143	6293
4	2803	2371	2587
5	2327	6195	4261
6	2922	961	1941
7	4362	3000	3681
8	14960	9549	12255
9	5735	2960	4348
10	2907	2458	2683
11	5603	3079	4341
12	10586	4678	7632
13	2379	1216	1797
14	2088	2934	2511
15	2194	4876	3535
16	1546	1402	1474

APPENDIX E

R STATISTICAL DATA

```
Call:
lm(formula = Ra ~ Doc + Fluid + Speed + Doc * Fluid, data = Roughness)

Residuals:
     1      2      3      4      5      6      7      8
 0.088  0.083  0.017  0.012 -0.088 -0.083 -0.017 -0.012

Coefficients:
             Estimate Std. Error t value Pr(>|t|)
(Intercept)  0.415000   0.166709   2.489  0.08853 .
Doc          0.012580   0.002004   6.276  0.00817 **
Fluid        0.733000   0.224098   3.271  0.04675 *
Speed       -0.007800   0.001090  -7.154  0.00562 **
Doc:Fluid   -0.013040   0.002835  -4.600  0.01931 *
---
Signif. codes:  0 '***' 0.001 '**' 0.01 '*' 0.05 '.' 0.1 ' ' 1

Residual standard error: 0.1002 on 3 degrees of freedom
Multiple R-squared:  0.9716,    Adjusted R-squared:  0.9337
F-statistic: 25.65 on 4 and 3 DF,  p-value: 0.01177
```

Figure E.1. Final model using R statistical software for meso milling A36 carbon steel.

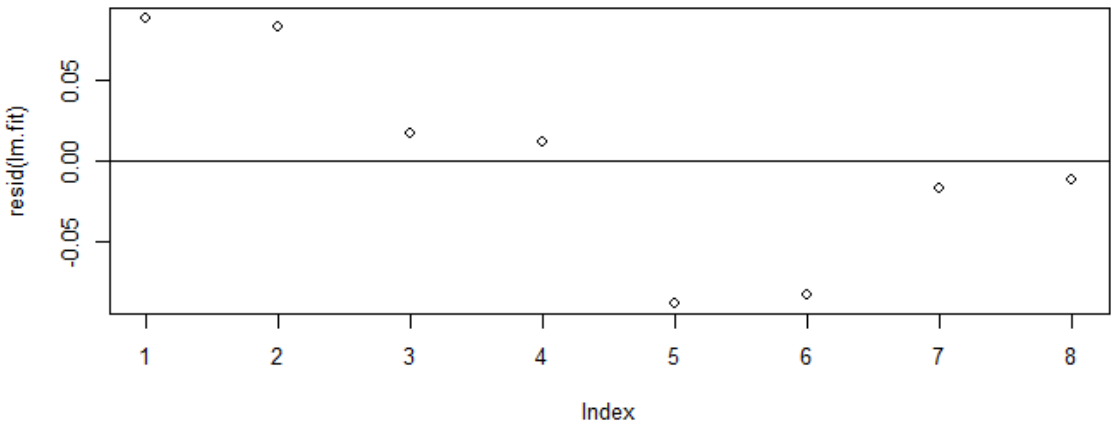

Figure E.2. Residual plot for meso milling A36 carbon steel.

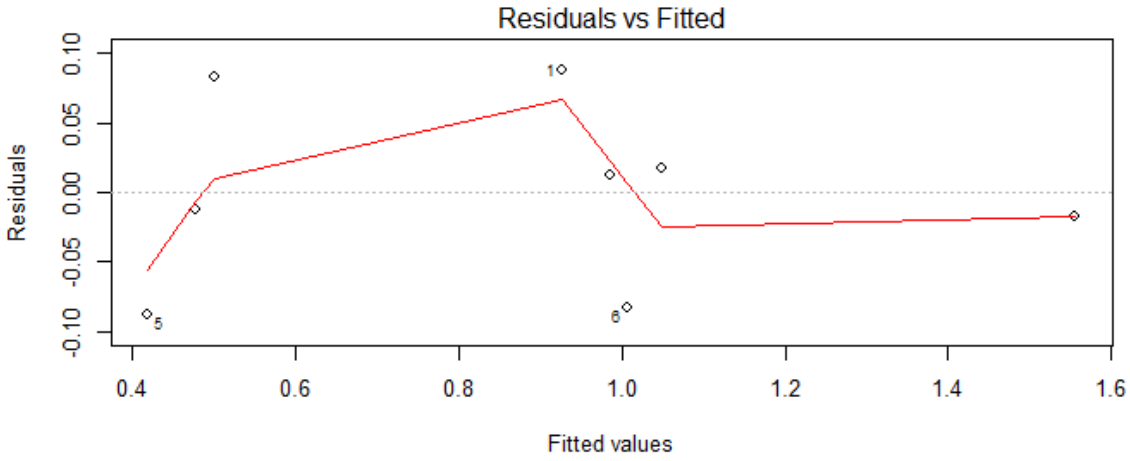

Figure E.3. Residuals vs Fitted for meso milling A36 carbon steel.

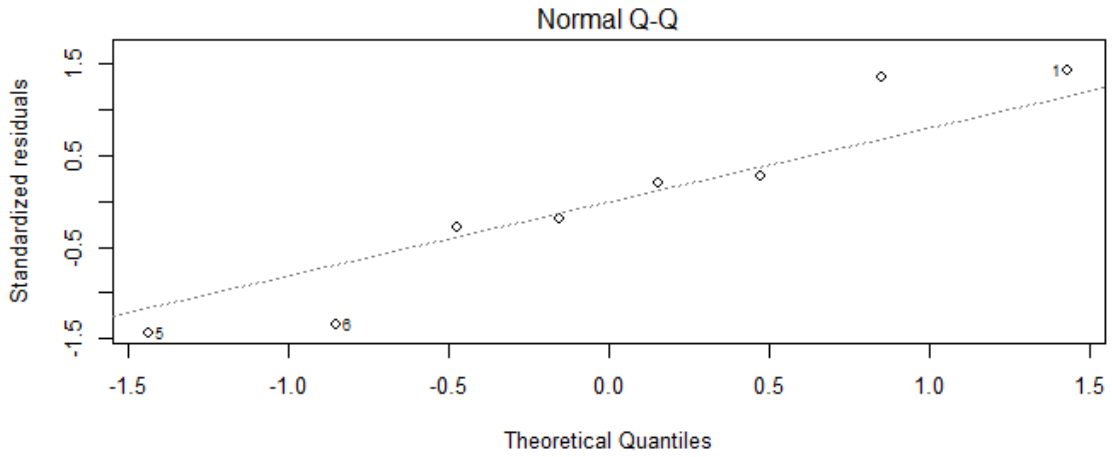

Figure E.4. Normal Q-Q plot for meso milling A36 carbon steel.

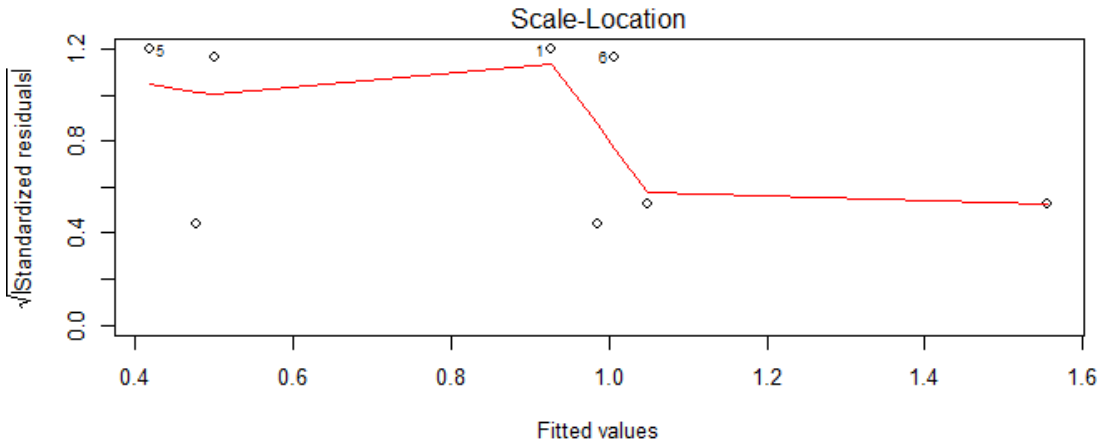

Figure E.5. Scale-Location plot for meso milling A36 carbon steel.

```
Residuals:
     Min       1Q   Median       3Q      Max
-0.09343 -0.05370  0.01891  0.04695  0.07832

Coefficients:
             Estimate Std. Error t value Pr(>|t|)
(Intercept) -2.263e-01  5.375e-02  -4.210  0.00102 **
BUE          3.575e-05  9.790e-06   3.652  0.00293 **
Toolwear     1.890e-05  6.042e-06   3.129  0.00799 **
---
Signif. codes:  0 '***' 0.001 '**' 0.01 '*' 0.05 '.' 0.1 ' ' 1

Residual standard error: 0.06499 on 13 degrees of freedom
Multiple R-squared:  0.6278,    Adjusted R-squared:  0.5706
F-statistic: 10.97 on 2 and 13 DF,  p-value: 0.001621
```

Figure E.6. Final model using R statistical software for difference (delta) between predicted roughness and actual roughness for micro milling 316L stainless steel.

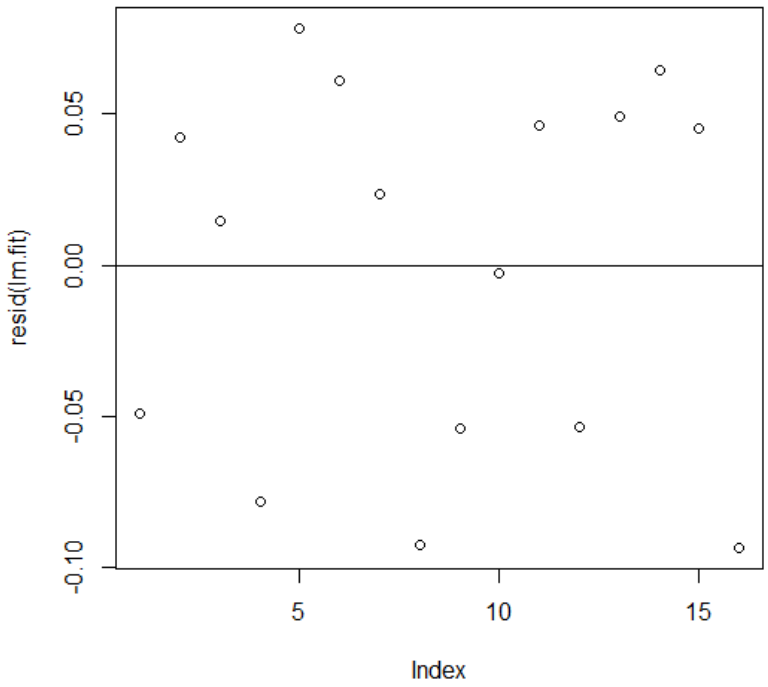

Figure E.7. Residual plot difference (delta) between predicted roughness and actual roughness for micro milling 316L stainless steel.

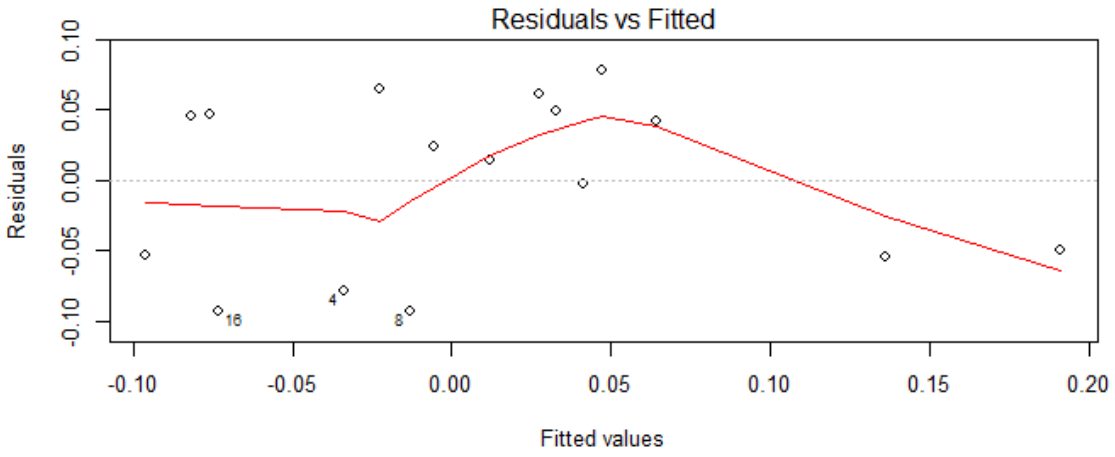

Figure E.8. Residuals vs Fitted plot between predicted roughness and actual roughness for micro milling 316L stainless steel.

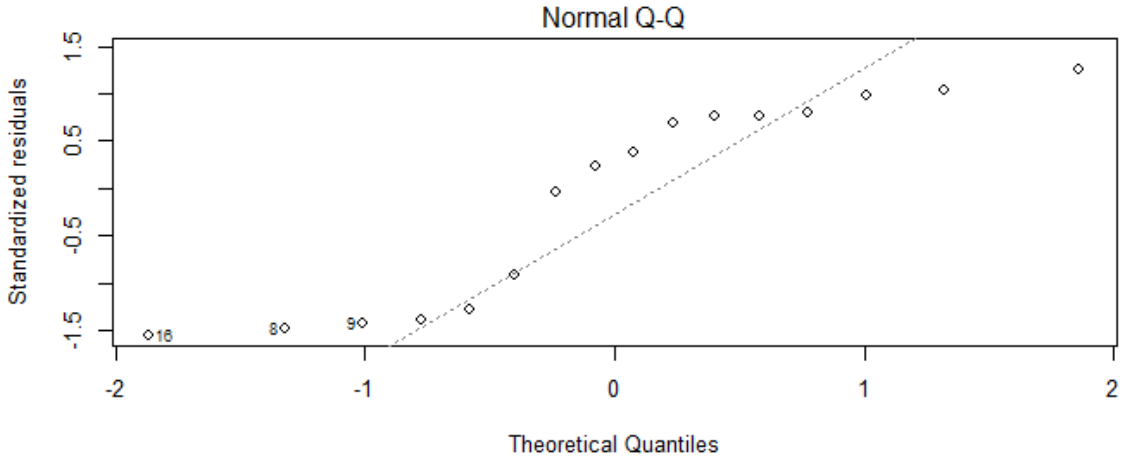

Figure E.9. Normal Q-Q plot difference (delta) between predicted roughness and actual roughness for micro milling 316L stainless steel.

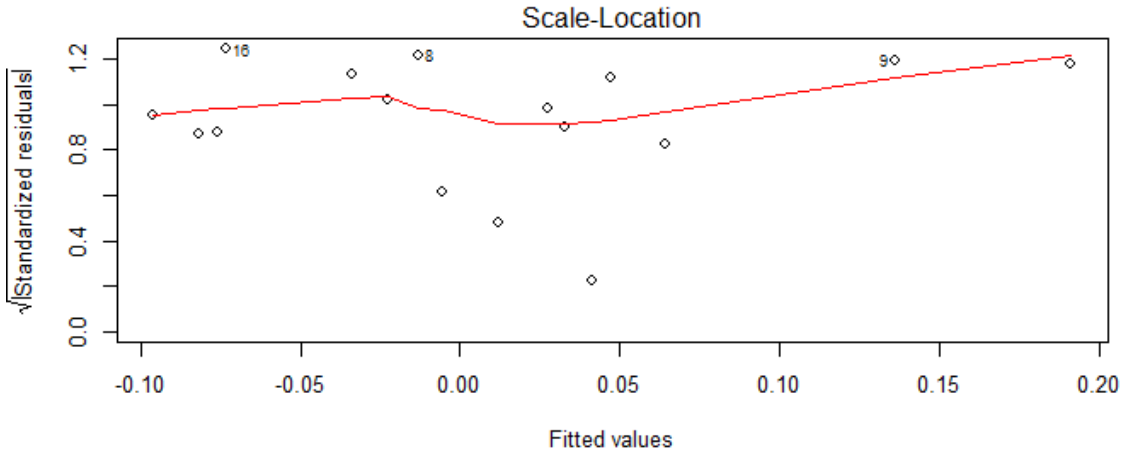

Figure E.10. Scale-Location plot difference (delta) between predicted roughness and actual roughness for micro milling 316L stainless steel.

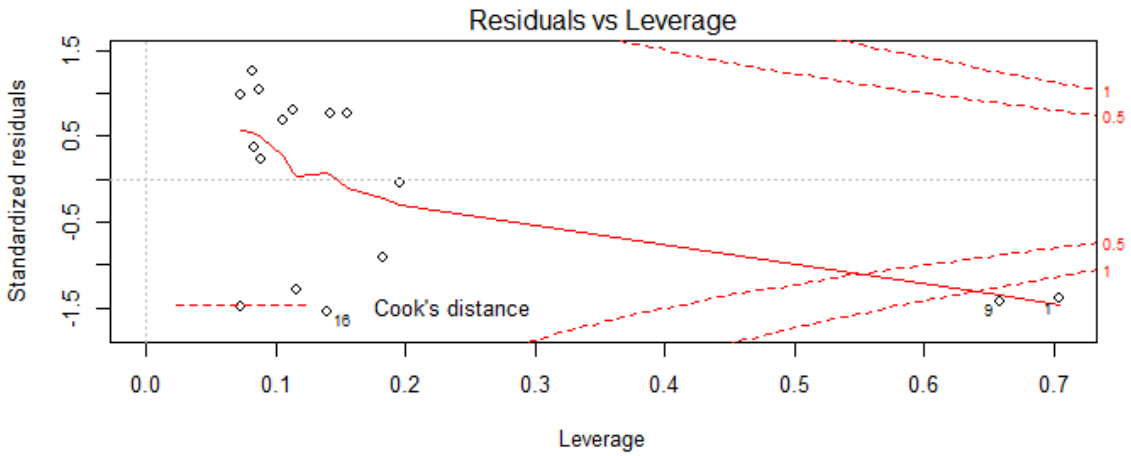

Figure E.11. Residuals vs Leverage plot difference (delta) between predicted roughness and actual roughness for micro milling 316L stainless steel.

```
Call:
lm(formula = BUE ~ Chipload + Speed, data = Roughness)

Residuals:
    Min      1Q  Median      3Q     Max
-1880.3  -461.8   -48.0   264.6  3336.7

Coefficients:
            Estimate Std. Error t value Pr(>|t|)
(Intercept)  7708.40     971.29   7.936 2.44e-06 ***
Chipload     4264.33    3243.31   1.315   0.2113
Speed        -144.33      63.04  -2.290   0.0394 *
---
Signif. codes:  0 '***' 0.001 '**' 0.01 '*' 0.05 '.' 0.1 ' ' 1

Residual standard error: 1200 on 13 degrees of freedom
Multiple R-squared:  0.5763,    Adjusted R-squared:  0.5111
F-statistic:  8.84 on 2 and 13 DF,  p-value: 0.003767
```

Figure E.12. Final model using R statistical software for BUE density for micro milling 316L stainless steel.

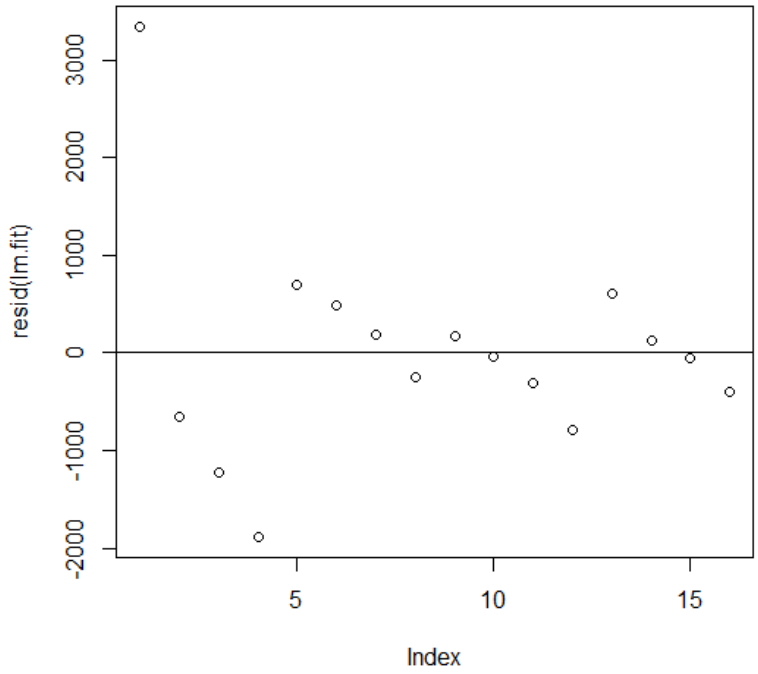

Figure E.13. Residual plot using R statistical software for BUE density for micro milling 316L stainless steel.

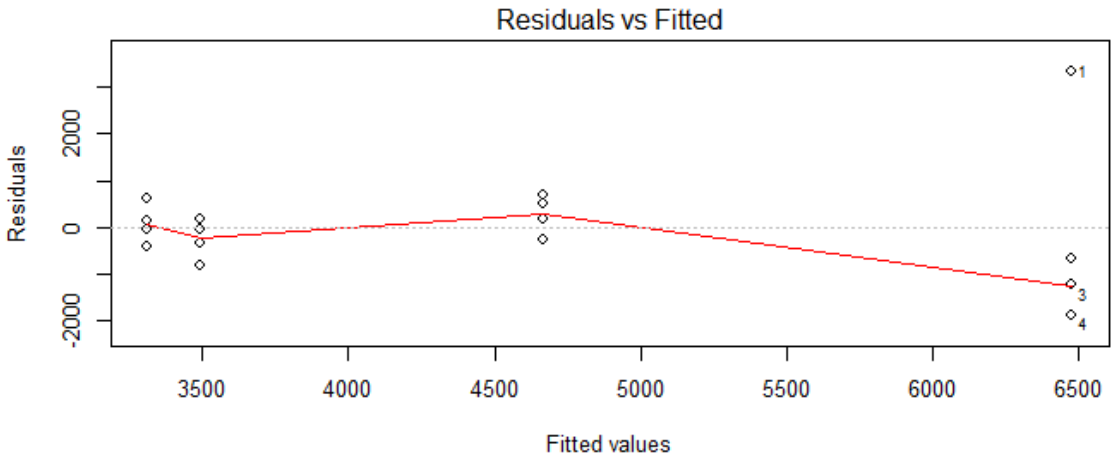

Figure E.14. Residuals vs Fitted plot using R statistical software for BUE density for micro milling 316L stainless steel.

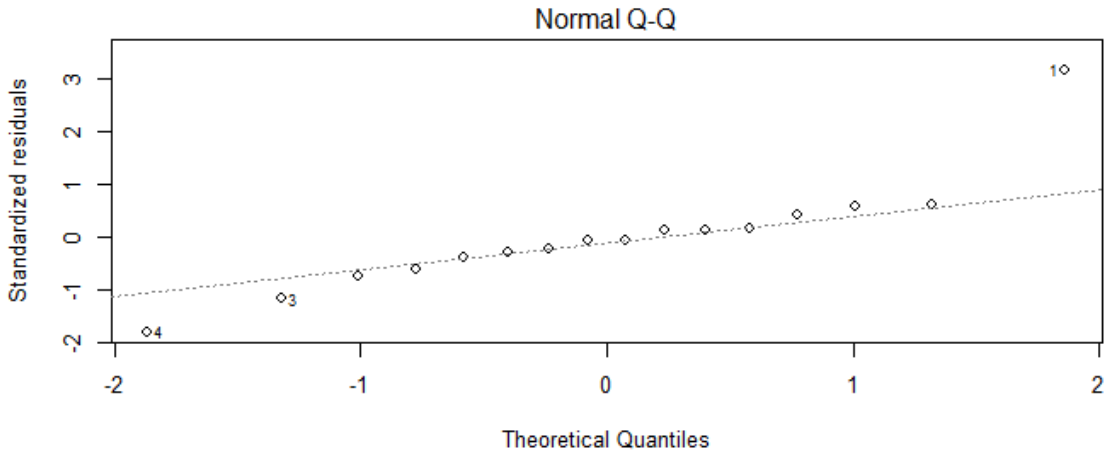

Figure E.15. Normal Q-Q plot using R statistical software for BUE density for micro milling 316L stainless steel.

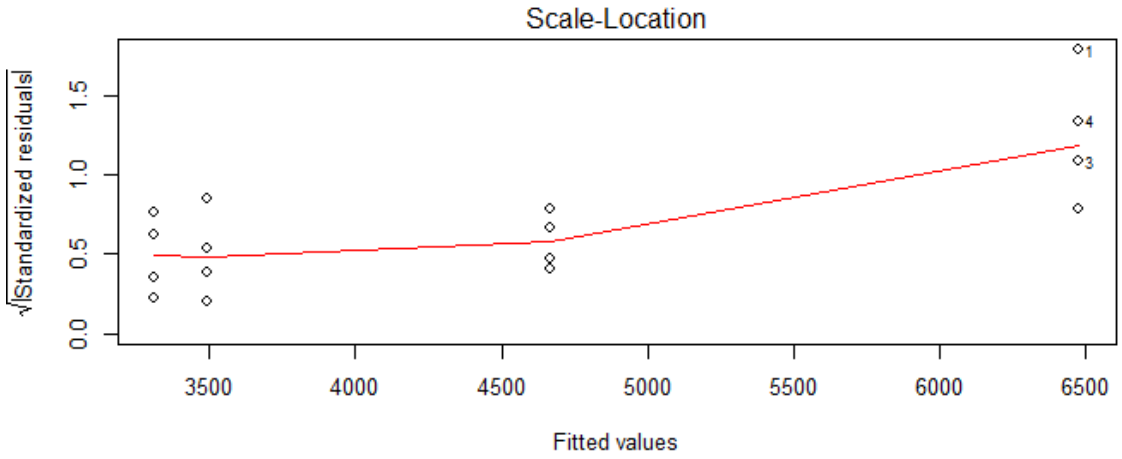

Figure E.16. Scale-Location plot using R statistical software for BUE density for micro milling 316L stainless steel.

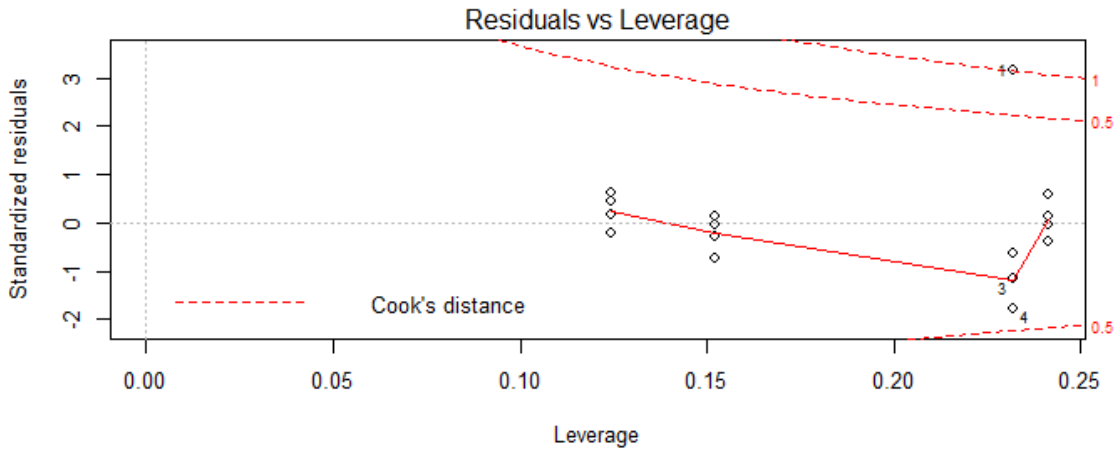

Figure E.17. Residuals vs Leverage plot using R statistical software for BUE density for micro milling 316L stainless steel.